

11-18
84731
0150
D180-30550-2

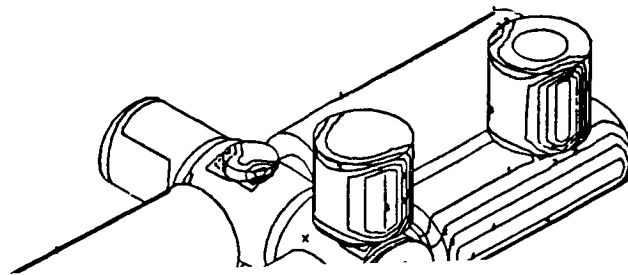
Final Report

Task 3 - Theoretical Analysis of Penetration Mechanics

**SPACE STATION INTEGRATED WALL DESIGN
AND PENETRATION DAMAGE CONTROL**

By

M. D. Bjorkman, J. D. Geiger, and E. E. Wilhelm



(NASA-CR-179166) SPACE STATION INTEGRATED
WALL DESIGN AND PENETRATION DAMAGE CONTROL.
TASK 3: THEORETICAL ANALYSIS OF PENETRATION
MECHANICS Final Report (Boeing Aerospace
Co.) 150 p Avail: NTIS EC A07/BP A01

N87-28582

Unclas
G3/18 0084731

Prepared for

National Aeronautics and Space Administration

July 1987

Contract NAS8-36426

Technical Management
NASA George C. Marshall Space Flight Center
Marshall Space Flight Center, Alabama
Structures and Dynamics Laboratory
Sherman L. Avan

Boeing Aerospace Company
Seattle, Washington

D180-30550-2

Final Report

Task 3 - Theoretical Analysis of Penetration Mechanics

SPACE STATION INTEGRATED WALL DESIGN AND PENETRATION DAMAGE CONTROL

By

M. D. Bjorkman, J. D. Geiger, and E. E. Wilhelm

Prepared for

National Aeronautics and Space Administration

July 1987

Contract NAS8-36426

Technical Management
NASA George C. Marshall Space Flight Center
Marshall Space Flight Center, Alabama
Structures and Dynamics Laboratory
Sherman L. Avan

Boeing Aerospace Company
Seattle, Washington

ABSTRACT

This report documents the effort to provide a penetration code called PEN4 version 10 for calculation of projectile and target states for the impact of 2024-T3 aluminum, R_p 90 1018 steel projectiles and icy meteoroids onto 2024-T3 aluminum plates at impact velocities from 0 to 16 km/s. PEN4 determines whether a plate is perforated by calculating the state of fragmentation of projectile and first plate. Depth of penetration into the second to nth plate by fragments resulting from first plate perforation is determined by multiple cratering. The results from applications are given.

KEY WORDS

Ballistic Limit Velocity
Cratering
Fragmentation
Hole Diameter
Hypervelocity Impact
Meteoroids
Orbital Debris
PEN4
Penetration Code
Residual Velocity
Spall

TABLE OF CONTENTS

	Page
1.0 INTRODUCTION	1
1.1 Purpose	1
1.2 Background	1
1.3 Modeling Approach	2
1.4 Road Map to Results From Those Tasks Performed for the "Space Station Wall Design and Penetration Damage Control" Contract	3
2.0 ANALYTICAL METHODOLOGY	4
2.1 PEN4 Version 10 Overview	4
2.2 Data Input	6
2.2.1 Material Parameters	6
2.2.2 Projectile/target Configuration	7
2.2.2.1 Angles Between the Plates	7
2.2.2.2 Projectile Yaw	7
2.2.3 Impact Velocity	9
2.2.4 Additional Parameters	9
2.3 First Plate Perforation	9
2.3.1 Ballistic Limit Velocity	9
2.3.2 First Plate Hole Diameter	12
2.3.2.1 Normal Impacts	12
2.3.2.2 Oblique Impacts	16
2.3.3 Residual Velocity	18
2.3.3.1 Derivation of Residual Velocity Relations for Normal Impacts	18
2.3.3.2 Comparison With Test Data	24
2.3.3.3 Oblique Impacts	27
2.3.4 Projectile Fragmentation Threshold Velocity	31
2.3.4.1 Normal Impacts	31
2.3.4.2 Oblique Impacts	35
2.3.5 Largest Residual Projectile Fragment Mass	35
2.3.5.1 Projectile Spall	38
2.3.5.2 Power-law Fragmentation	38
2.3.5.3 Power-law Roll Off Fragmentation	44
2.3.5.4 Oblique Impacts	46
2.3.6 Projectile Residual Mass Distribution	48
2.3.6.1 Definitions and Important Empirical Results	48

2.3.6.2	Fragment Mass Distribution Dimensional Analysis	50
2.3.6.3	Fits to Cumulative Fragment Mass Fraction Data	53
2.3.6.4	Oblique Impacts	57
2.3.6.5	Fragment Mass Bins	57
2.3.7	Projectile Fragment Number	62
2.3.8	Plate Plug Fragment Mass Distribution and Number	62
2.4	Second Plate Perforation	64
2.4.1	Spatial Distribution of Fragments on Second Plate	66
2.4.2	Crater Depth and Radius	68
2.4.2.1	Normal Impacts	68
2.4.2.2	Oblique Impacts	73
2.4.3	Multiple Cratering and Probability of Perforation	73
2.4.4	Holed Out Area on the Second Plate	76
2.4.5	Number of Fragments Residual After Second Plate	76
2.4.6	Increased Penetration From Plate Spall	77
2.4.6.1	Spall Threshold Velocity	78
2.4.6.2	Spall Fragment Mass Distribution	81
2.4.7	Second Plate Penetration By Icy Projectiles	81
2.5	Data Output	88
3.0	PENETRATION CODE LIMITATIONS	89
3.1	Limitations on Materials	89
3.2	Limitations on Configurations	89
3.2.1	Projectile Shape	89
3.2.2	Plate Arrangements	89
3.3	Limitations on Intercept Conditions	90
3.3.1	Impact Velocity	90
3.3.2	Impact Angle	90
4.0	COMPARISON WITH TEST DATA	91
4.1	Comparison With Steel Projectile Data	91
4.2	Comparison With Aluminum Projectile Data	95
5.0	RECOMMENDATIONS	102
6.0	REFERENCES	103

APPENDIX A	OBLIQUE IMPACTS DATA SEARCH	107
APPENDIX B	EFFECT OF RATE DEPENDENT YIELD ON BALLISTIC LIMIT VELOCITY SIZE DEPENDENCE.	112
APPENDIX C	EFFECT OF FRACTURE SURFACE ENERGY ON LARGEST RESIDUAL FRAGMENT MASS.	115
	C-1 Grady's Model for Fragment Size From the Radial Expansion of Spherical Fluid Projectiles	115
	C-2 Generalization of Grady's Model to the Impact of Metal Projectiles on Metallic Plates	117
	C-3 The Fit of Equation C-10 to Test Data	117
APPENDIX D	EFFECT OF PROJECTILE FRAGMENT SPATIAL DISTRIBUTION	131
APPENDIX E	DEMONSTRATION OF CONVERGENCE	135
APPENDIX F	CRITICAL DIAMETER CURVE BEHAVIOR AT IMPACT VELOCITIES LARGER THAN 13 km/s	137

LIST OF FIGURES

Figure No.	Title	Page
2-1	PEN4 Version 10 Flow Chart	5
2-2	Impact Geometry Assumed for PEN4	8
2-3	Comparison of Ballistic Limit Velocity Relations	13
2-4	Scaled Hole Diameter	15
2-5	Comparison of Hole Diameter Relation With GM Test Data	17
2-6	The Hole Diameter Relation as a Function of Angle of Obliquity Cross Plotted With Test Data	19
2-7	Comparison of DoD Residual Velocity Relation Large Impact Velocity Data	20
2-8	The Geometry of Plate Plugging	21
2-9	Comparison of Eq. 27 With Large Impact Velocity Test Data	25
2-10	Residual Velocity Mass Ratio Exponent for Four Projectile/Target Combinations	26
2-11	Comparison of Residual Velocity Prediction with Test Data, Aluminum Striking Aluminum	28
2-12	Comparison of Residual Velocity Prediction with Test Data, Steel Striking Aluminum	29
2-13	Change in Angle of Obliquity as a Function of Impact Velocity	30
2-14	Fragmentation Threshold Velocity for 2024-T3 Aluminum Cylinders Striking 2024-T3 Aluminum Plate and R _B 90 1018 Steel Cubes Striking 2024-T3 Aluminum Plate	34
2-15	Schematic Representation of the Experimentally Observed Dependence of Largest Residual Fragment Size on Impact Velocity	37

2-16	Experimentally Measured Dependency of Largest Residual Fragment Size on Impact Velocity For Mild Steel Cubes Striking 2024-T3 Aluminum Plates	39
2-17	Experimentally Measured Dependency of Largest Residual Fragment Size on Impact Velocity For Lexan Projectiles Striking Cubes of Basalt	40
2-18	Dependence of Average Fragment Size from an Exploded Case on the Fracture Toughness of the Case	42
2-19	Boundary Between Power-law fragmentation and and Power-law Roll Off Fragmentation for R_{p90} 1018 Steel Cubes Striking Aluminum Plate	45
2-20	Residual fragment mass distributions for four Fragmentation Processes	49
2-21	Distribution of Residual Fragments from Steel Cubes Striking Aluminum	51
2-22	Comparison of PEN4 Cumulative Mass Distribution with Test Data	56
2-23	Allocation of Mass Within the Mass Bins	58
2-24	Effect of Equal Mass in the Bins on the Critical Diameter Curve	60
2-25	Effect of Unequal Mass in the Bins on the Critical Diameter Curve	61
2-26	Transmitted Mass Fraction as a Function of Angle of Impact Obliquity	63
2-27	Ratio of the first plate mass loss to projectile mass along the critical diameter curve for a 125 mil plate shielded by a 63 mil plate separated by 4 inches	65
2-28	Dependence of Projectile Spray Angle on Impact Velocity	67
2-29	Large Impact Velocity Crater Depth Relation	69
2-30	Small Impact Velocity Crater Depth Relations	71
2-31	Crater Depth to Diameter Relations For Small Impact Velocities	72

2-32	Schematic Representation of the Calculation of Probability of Perforating the Second Plate	74
2-33	Geometry and Definition of Variables Used to Evaluate Two Plate Spall	79
2-34	Comparison of Results From Eq. 89 With SM-1 Test Data	82
2-35	Thor 41 Ballistic Limit Velocity Relations For Aluminum, Steel, and Tungsten Striking Aluminum	84
2-36	The σ/δ Dependence of the Ballistic Limit Velocity Relation for Aluminum, Steel, and Tungsten Striking Aluminum	86
2-37	The Calculated Critical Diameter Curves for Icy Meteoroids Striking Aluminum for 0, 45, and 60 Degrees Angle of Obliquity	87
2-38	Comparison With NSWCV TR-79-66 Number of Plates Perforated Data	93
2-39	Critical Diameter Curves for R _B 90 1018 Steel Cubes Striking 63 mil 2024-T3 shield Plate Spaced 4 inches from 125 mils 2024-T3 Second Plate	94
2-40	Comparison With NSWC Tr-79-66 Second Plate Hole Diameter Data	96
2-41	Comparison With SM-1 0 Degree Obliquity Critical Diameter Data	97
2-42	Comparison With NAS8-36426 45 Degree Obliquity Critical Diameter Data	98
2-43	Comparison With NAS8-36426 60 Degree Obliquity Critical Diameter Data	99
2-44	Comparison With SM-1 6 inch Plate Spacing Critical Diameter Data	101
A-1	Oblique Impact Hole Diameter Data.	108
A-2	Oblique Impact Hole Diameter Data.	109
A-3	Oblique Impact Hole Diameter Data.	111

B-1	Strain-Rate Sensitivity of Aluminum Alloys	113
C-1	Largest Residual Fragment mass as a Function of Impact Velocity for R _B 90 1018 Steel Cubes Striking 2024-T3 Aluminum Plate, $t/d=0.065$	119
C-2	Largest Residual Fragment mass as a Function of Impact Velocity for R _B 90 1018 Steel Cubes Striking 2024-T3 Aluminum Plate, $t/d=0.1$	120
C-3	Largest Residual Fragment mass as a Function of Impact Velocity for R _B 90 1018 Steel Cubes Striking 2024-T3 Aluminum Plate, $t/d=0.2$	121
C-4	Largest Residual Fragment mass as a Function of Impact Velocity for R _B 90 1018 Steel Cubes Striking 2024-T3 Aluminum Plate, $t/d=0.4$	122
C-5	Largest Residual Fragment mass as a Function of Impact Velocity for R _B 90 1018 Steel Cubes Striking 2024-T3 Aluminum Plate, $t/d=0.8$	123
C-6	Measured Functional Dependence of Largest Residual Fragment Mass on t/d for R _B 90 1018 Steel Cubes Striking 2024-T3 Aluminum Plate	124
C-7	Largest Residual Fragment Mass as a Function of Impact Velocity for Steel Cubes and Aluminum Cylinders Striking Aluminum	125
C-8	Correlation Between Fracture Toughness and Yield Strength for Ultra-High Strength Steels	128
C-9	Largest Residual Mass as a Function of Impact Velocity for Aluminum Cylinders Striking Aluminum Plate in the Fragmentation Roll-Off Regime	130
D-1	Critical Diameter Curves Calculated Using FATE Spatial Distribution and an Equal Probability of Impacting any Spot in the Spray Area	132
D-2	Critical Diameter Curve Calculated With FATE 2	133
E-1	Test for Convergence	136
F-1	Critical Diameter Curve Behavior Above 13 km/s Impact Velocity	138

LIST OF TABLES

Table No.	Title	Page
C-1	Fracture Toughness for 8 Materials	126

This page left intentionally blank.

1.0 INTRODUCTION

The analysis and penetration code documented in this report is the result of a continuing study over the past 8 years under a variety of funding sources. The last effort consisted of four tasks performed under the "Space Station Wall Design and Penetration Damage Control" contract NAS8-36426 with the National Aeronautics and Space Administration, Marshall Spaceflight Center, Huntsville, Alabama. The objectives of this last effort were to improve the calculation of oblique impacts and the multiple cratering algorithm and to generalize the code to treat icy projectiles. The entire analysis technique is documented here, even portions not developed under the "Space Station Wall Design and Penetration Damage Control" contract. The 4 tasks specifically performed for the "Space Station Wall Design and Penetration Damage Control" contract are briefly described in section 1.4, where a road map is given for finding in this document the complete descriptions of the results of those 4 tasks.

1.1 PURPOSE

The purpose of this contract was to develop new relations and incorporate those into the existing penetration code, PEN4, and to validate the PEN4 output by comparison with aluminum projectile striking aluminum plates test data.

Specific improvements made to PEN4 were:

1. New relations for hole diameter, crater depth and diameter, and projectile largest residual fragment mass as a function of impact angle.
2. Revision of the PEN4 relations that calculate the probability of multiple impacts at a single place on the second plate to include impacts by projectile fragments with different sizes.
3. Development of relations for plate fragment size distribution from impacts with icy projectiles.

1.2 BACKGROUND

The original PEN4 (version 1) was developed in 1978 with Boeing IR&D funds to analyze the impact of high density (7.8 to 16 g/cm^3) metal projectiles onto aluminum plates at impact velocities between 5 and 10 km/s . At these impact velocities the projectile will be well fragmented, hence the PEN4 analysis treats the perforation of the second plate in a plate array target as a series of multiple cratering events by the projectile fragments. Version 1 was used on an Air Force contract and Boeing IR&D programs to

evaluate the vulnerability of satellite and aircraft targets. Version 1 was documented under Navy contract in Ref. 1.

During 1985 and 1986 further improvements to the fragment size calculation were made under Boeing IR&D to support the Boeing space station proposal effort and are documented in Ref. 2. These improvements made it possible to reproduce by calculation the observed behavior that the minimum aluminum projectile diameter required for perforation of a given two plate array increases with increasing impact velocity for impact velocities in excess of 3 km/s. This phenomenon is the basis for spacecraft protection by the Whipple meteoroid "bumper." To the best of our knowledge PEN4 is the only penetration code that reproduces this important result at large impact velocities.

Two contracts with NSWC/D were running concurrently with the Boeing IR&D program. Both contracts N 60921-84-C-A172 and N 60921-83-C-A246 were tasked with developing fragmentation relations from recent NSWC/D test data (the results are documented in Refs. 3 and 4). These relations for residual fragment mass distribution and largest residual fragment mass presented the basis for a significant improvement in the fidelity of the PEN4 modeling of the impact of steel projectiles onto aluminum plates. This led to a contract with NSWC/D to incorporate the new relations for fragmentation into PEN4, called PEN4 version 9.

The current contract with NASA/MSFC was prompted in part by the encouraging progress made under IR&D and the desire to develop a methodology incorporating material properties into the analysis.

1.3 MODELING APPROACH

PEN4 is a collection of relations describing the projectile and target state to a level of detail consistent with producing a fast-running code. The benefit of such an approach is a modular code, constructed around the various physical phenomena that occur. Thus any improvement in understanding the penetration process requires replacing only one module and not an extensive code rewrite.

Lacking a complete understanding of fragmentation from which ab initio calculations can be performed, the approach presented here has been to produce empirical relations closely tied to the results of impact tests. The important impact parameters are identified through test or theory and used in a dimensional analysis to constrain the functional relationships between the parameters. In some cases, tests were then constructed to validate the parameter selection and the functional forms fitted to the data.

This approach should be superior to strict empiricism because physical models of fragmentation are used to identify the significant parameters and, ideally, tests are performed to validate the parameter selection.

1.4 ROAD MAP TO THE RESULTS FROM THOSE TASKS PERFORMED FOR
THE "SPACE STATION WALL DESIGN AND PENETRATION DAMAGE
CONTROL" CONTRACT.

PEN4 Version 8, documented in Ref. 2, has been modified under the "Space Station Wall Design and Penetration Damage Control" contract to support Space Station vulnerability assessment. Documentation of improvements made to PEN4 to bring it up to version 10 are found in:

Task 1: The data search for oblique impact data is documented in Appendix A.

Task 2: The development of the oblique impact relations is described in sections 2.3.2.2 for the hole diameter, section 2.3.3.2 for residual velocity, section 2.3.4.2 for fragmentation threshold velocity, section 2.3.5.4 for largest residual fragment mass, section 2.3.6.4 for residual fragment mass distribution, and section 2.4.2.2 for the crater depth.

Task 3: The development of relations for probability of multiple impacts by fragments with different sizes is documented in 2.4.3.

Task 4: The development of plate perforation relations for icy projectiles is described in section 2.4.7.

2.0 ANALYTIC METHODOLOGY

The section presents the analytic methodology that constitutes PEN4 Version 10. This version provides the capability to assess the results of aluminum, steel, and icy projectiles striking aluminum spaced plates at impact velocities from 0 to 16 km/s.

An overview of PEN4 version 10's structure is discussed in section 2.1. The input requirements are discussed in section 2.2. The mathematical relationships used in each module shown in figure 2-1 are discussed in section 2.3 for the first plate perforation and section 2.4 for second plate perforation. The last section, section 2.5, discusses the output.

2.1 PEN4 VERSION 10 OVERVIEW

The logic for the PEN4 Version 10 program is shown as a flow chart in figure 2-1. The first plate impact is treated with mathematical relations different from those used for the second plate impact. All second plate interactions are collected in figure 2-1 below the broken line.

At the first module (labeled 2.3.3 in figure 2-1), projectile residual velocity is calculated. (Note that the module label is the document section number where the equations for the module are discussed.) A decision is made in the first module on whether the calculated residual velocity is greater than zero (i.e., the impact velocity exceeds the first plate ballistic limit velocity. The ballistic limit velocity used in PEN4 is discussed in section 2.3.1.). If false, the program ends; if true, the hole diameter in the first plate is calculated at module 2.3.2. The leading edge residual velocity of the projectile or projectile/debris cloud is then calculated at module 2.3.3. Next, the minimum impact velocity required for projectile fragmentation, V_f , is calculated at module 2.3.4. A decision is made whether impact velocity exceeds V_f . If false, the projectile is not fragmented and second plate perforation is decided on the basis of the ballistic limit equation, module 2.3.1. If true, the state of the fragmented projectile is calculated. The mass of the largest piece is calculated at module 2.3.5, the distribution of fragment sizes is calculated at module 2.3.6, and the number of fragments is calculated at module 2.3.7.

Second plate perforation is decided by one of two methods, depending on whether the projectile fragmented. If the projectile is intact, then second plate perforation is determined by the ballistic limit relation, module 2.3.1, as described above. If the projectile fragmented, then the spray area on the second plate is calculated at module 2.4.1. Crater depth and diameter in the second plate for each fragment size is calculated at module 2.4.2. The minimum number of multiple craters required to perforate the second plate is then calculated, the largest likely hole depth is computed, and a decision is made on whether the second plate was perforated.

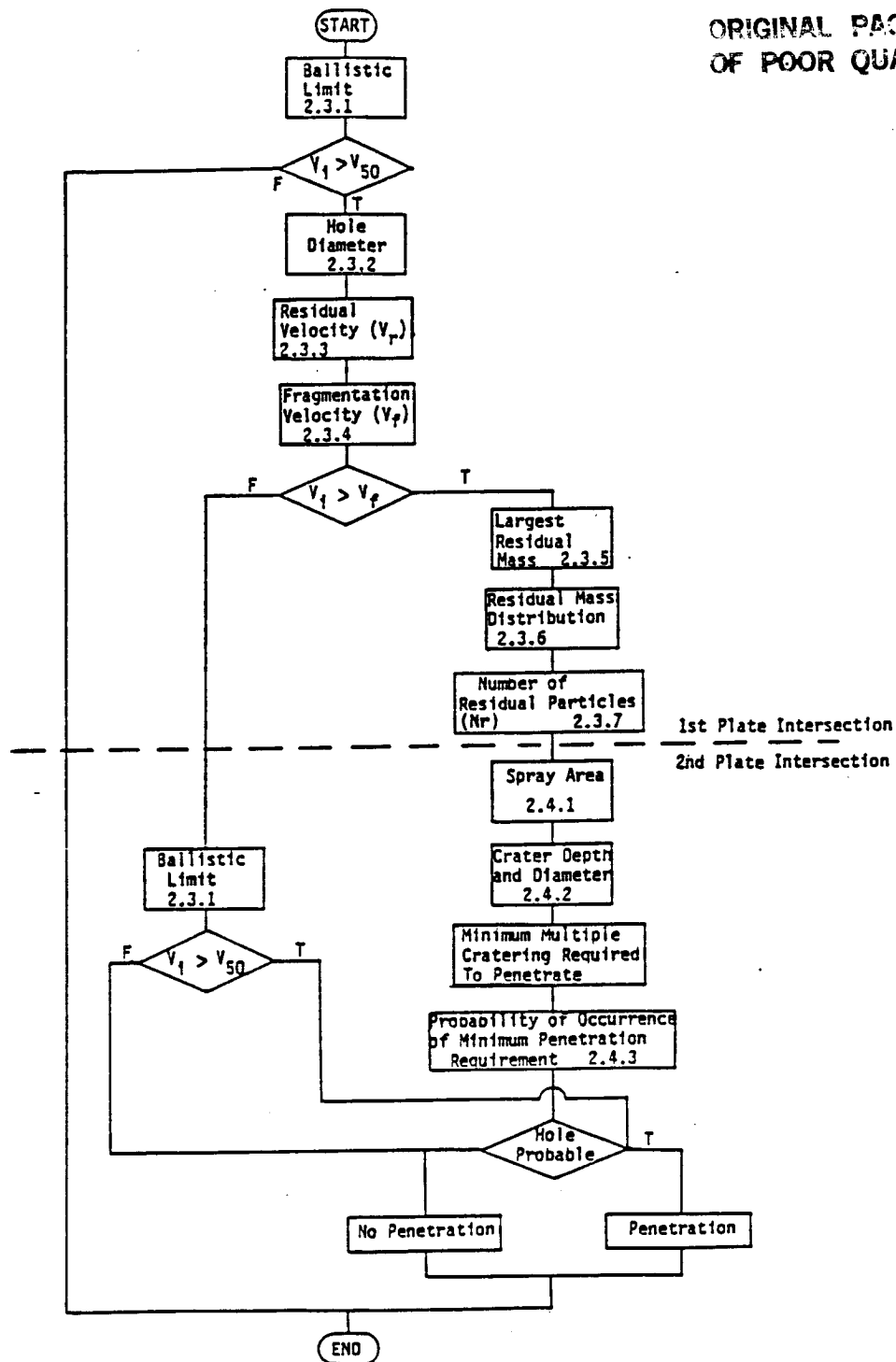
ORIGINAL PAGE IS
OF POOR QUALITY

Figure 2-1 PEN4 version 10 flow chart.

2.2 DATA INPUT

Fourteen parameters are passed to PEN4 through the FORTRAN calling statement,

Call PEN4(Vil, MProj, Thetal, Thickl, Space, Pennon, Shater,
Densel, Ystrnl, SoundV, Tau0l, Pdeep, Area, nr2).

The data input consist of: 1) projectile and target material properties, Densel, Ystrnl, SoundV, Tau0l; 2) projectile and target configuration, Mproj, Thetal, Thickl, Space; and 3) impact velocity, Vil. The above three categories of parameters required for input into PEN4 are described below.

2.2.1 Material Parameters

Currently, PEN4 is capable of calculating the effects of 2024-T3 aluminum and R_B 90 1018 steel projectiles striking 2024-T3 aluminum plates. However, the user does not have access to the R_B 90 1018 mild steel projectile material equations in PEN4 through the FORTRAN Call to PEN4 illustrated above. If the user desires the R_B 90 1018 mild steel projectile option, then the code must be rewritten to pass the parameter PrMat, which equals 1 for R_B 90 1018 steel projectiles and 2 for 2024-T3 aluminum projectiles. The statement fixing PrMat=2 in PEN4 must also be removed and the code recompiled.

The material parameters PEN4 requires passed through the FORTRAN Call are:

Densel a dimension 10 array containing the density of target plates 1 through 10 in pounds per cubic inch. The density of the projectile material is contained in data statements within PEN4.

Ystrnl a dimension 10 array containing the strength of target plates 1 through 10 in pounds per square inch. The strength of the projectile is not needed.

SoundV a dimension 10 array containing the sound velocities of target plates 1 through 10 in feet per second. The sound speed in the projectile material is contained data statements within PEN4.

Tau0l a dimension 10 array not currently used.

The above material parameters can be used to partially correct the PEN4 output when using different alloys of aluminum. However, if the results are significantly different from those for 2024-T3 aluminum, then they are questionable.

It should be noted that a number of empirically determined material parameters are built into the various calculations; i.e., V_{50} , V_f , m_r in the roll-off fragmentation region, cumulative mass fraction distribution, spray angle, and low velocity crater depth. Thus, if it desired to generalize PEN4 to materials other than 2024-T6 aluminum or R_B 90 1018 steel projectiles and 2024-T3 aluminum target plates, then changing the material parameters in the arrays listed above will not completely correct these calculations for the new materials.

2.2.2 Projectile/Target Configuration.

The projectile/target configuration parameters required are:

- Mproj Projectile mass in pounds.
- Thetal The angle of obliquity of the projectile shotline
 with respect to the shield outwards normal.
- Thick1 A dimension 10 array containing the thicknesses of
 target plates 1 through 10 in feet.
- Space A dimension 10 array containing the spacing between
 plates in feet.

2.2.2.1 Angles Between the Plates. The impact geometries that can be modeled with PEN4 are illustrated in figure 2-2. The projectile is allowed to impact the first plate at any angle of obliquity (measured relative to the normal of the first plate). Note, however, that the second through tenth plates are not free to take any orientation with respect to the first plate. The second through tenth plates are parallel, and the normal of the second plate must lie in the same plane as that containing the normal of the first plate and the projectile path. Thus the angular orientation of the second plate is described by one angle, γ , and not the general case of two angles. The angle γ has been set equal to 0 degrees obliquity within PEN4 and can only be changed by resetting that equivalency and recompiling PEN4.

2.2.2.2. Projectile Yaw. Since projectile yaw effects are strongly shape dependent and intrinsically difficult to model, it was desired to develop PEN4 from spherical projectile test data, where there are no complicating yaw effects. This was not entirely possible. The ballistic limit velocity and residual velocity relations were developed from some spherical projectile data, while all fragmentation models were developed from what was available, cubical and cylindrical projectile test data. Yaw was measured for the steel cube cumulative mass fraction distribution test data, hence a relation was developed for yaw effects and coded into PEN4. Currently, PEN4 is written to set the yaw equal to 0 degrees; therefore, any user desiring to use this feature must rewrite the code so that the yaw may be passed into PEN4.

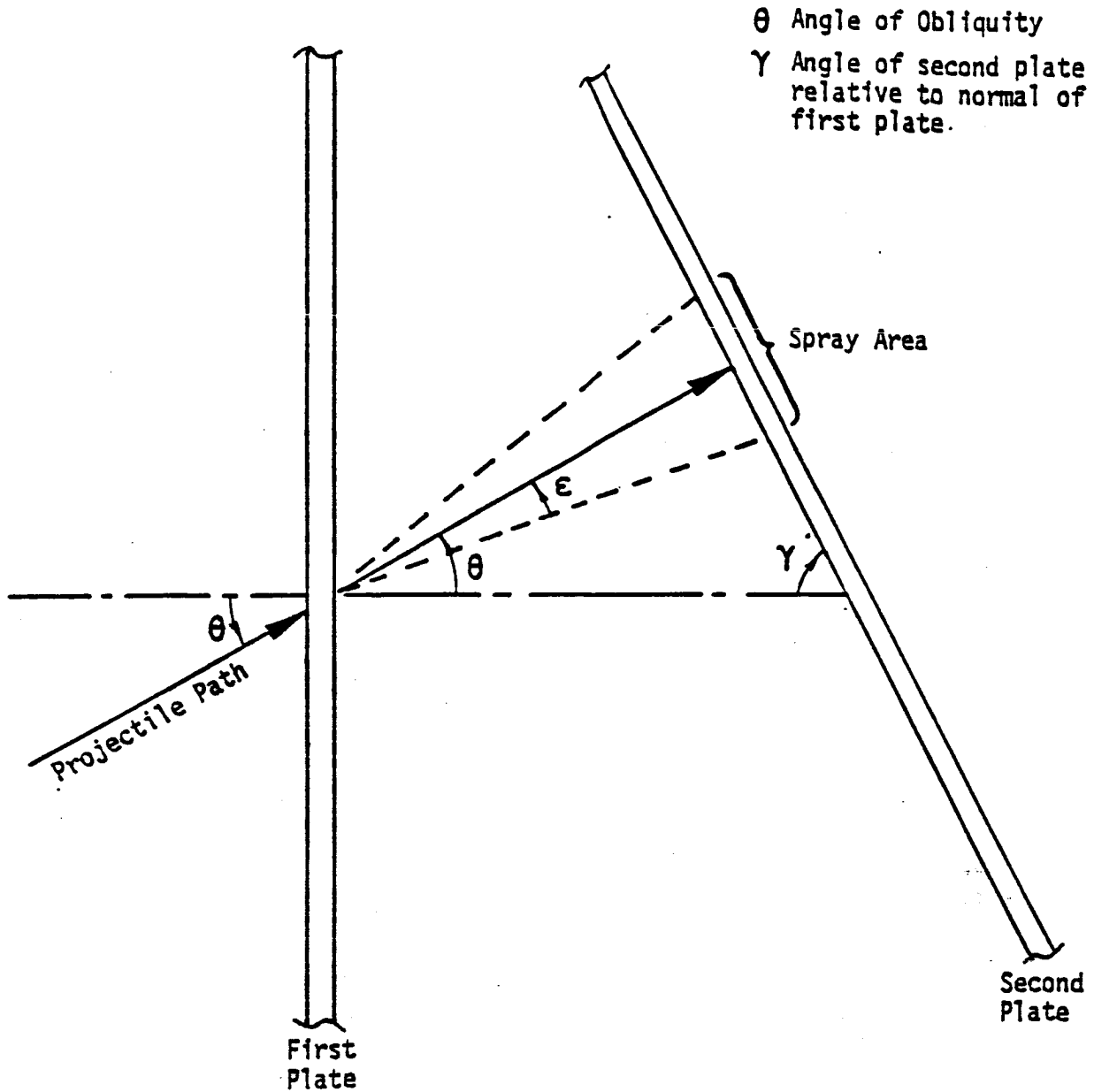


Figure. 2-2. Impact geometry assumed for PEN4.

2.2.3. Impact Velocity.

The impact velocity parameter required is,

Vi1 the impact velocity in feet/s.

2.2.4. Additional Parameters.

In addition to the above input parameters, there are the logical parameters,

Pennon .True. when the array is perforated and .False. when the array is not perforated.

Shater .True. when the user wishes to use the fragmentation portion of PEN4 and .False. when the user desires to only use the ballistic portion of PEN4.

2.3 FIRST PLATE PERFORATION

The various relations used to calculate the state of the first plate and the state of the projectile are collected in this section. When the relations used in a section are drawn from the literature, reference is made to the literature for validation of the relations. When the relations used are original to this report, the relations are validated by analysis and comparison with test data. The relations for predicting second plate perforation are collected in section 2.4.

2.3.1 Ballistic Limit Velocity

A number of ballistic limit relations have been developed and reported in the literature. The relations can be broadly classed into empirical relations, analytical relations, and hydrocode solutions of the balance relations of continuum mechanics. These relations were reviewed up to 1978 by Backman and Goldsmith, Ref. 5, and their number is still growing.

Two analytical relations (Refs. 6 and 7) for ballistic limit velocity based on simple physical models of perforation have been used in previous versions of PEN4, and two others were examined as possible replacements (Refs. 8 and 9). In each case, the simple model either produced incorrect behavior for some regions of t/d and impact velocity, or required parameters not related to available material properties. Thus, at best the analytic models were only providing guidance on the functional form to fit to ballistic limit test data.

Since the analytical models examined were in practice fits to a limited set

of test data, it was decided that the best approach to take with PEN4 was to use the empirical fit,

$$V_{50} = C_b (\delta t A_p / m)^b (\delta t A_p / m_0)^f \sec^h \theta, \quad (1)$$

developed from the large body of ballistic limit velocity data collected for Project THOR (Refs. 10, 11 and 12). Furthermore, the Department of Defense tri-services committee for standardizing penetration equations for aerial target vulnerability has approved Eq. 1 and listed the fit parameters measured for 17 target materials.

The variable δ in Eq. 1 is the projectile density, A_p is the presented area of the projectile, m is the mass of the projectile, θ is the angle of obliquity of projectile impact, and t is the plate thickness.

The material parameters C_b , b , f and h can be determined only by ballistic limit tests and are constant for any given target and projectile material combination. The parameter m_0 is a constant independent of target and projectile material properties and is always equal to 100 grains weight (6.48 grams).

An interesting feature of Eq. 1 is the large size dependence embodied in the exponent f . The size exponent results from some rate dependent material property governing perforation, most likely rate dependent yield or fracture of the target plate. The exponent f can be shown to be larger than expected for rate dependent yield by a dimensional analysis argument. Typical values for the size exponent f measured in the Project THOR ballistic limit velocity tests (Ref. 12) are -0.07 to -0.02 for mild steel striking magnesium, aluminum, mild steel, cast iron, and lead target plates.

For simplicity this dimensional analysis is limited to rigid projectiles. For the ballistic limit of plates struck by rigid projectiles one expects the projectile diameter d , the projectile density δ , the target plate density ρ , the target plate thickness t , the rate independent target strength Y , and θ the angle of obliquity of the impact to govern the ballistic limit velocity V_{50} . Hence, by the pi theorem of dimensional analysis there are 4 independent groups of dimensionless variables, or

$$\sigma V_{50}^2 / Y = f(t/d, \rho/\delta, \theta). \quad (2)$$

Rate dependent material strength can be fitted to the functional form,

$$Y = k (d\epsilon/dt)^n, \quad (3)$$

over ranges of strain rate $d\epsilon/dt$ governed by a single rate dependent yield mechanism. The parameters k and n are material constants which vary from target material to target material. Values for n are determined in Appendix A, where it is shown that the exponent n is typically between 0.0 and 0.01 for ballistic impact of 2024-T3 aluminum plates. Rewriting Eq. 2 as a func-

tion of the rate dependent target material parameters k and n in place of the rate independent target material strength Y gives,

$$\rho V_{50}^2 / [k(V_{50}/t)^n] = f(t/d, \rho/\delta, \theta, n). \quad (4)$$

Rewriting Eq. 4 in a form compatible with Eq. 1 gives,

$$V_{50} = (k/\rho)^{1/(2-n)} t^{-n/(2-n)} f(t/d, \rho/\delta, \theta, n). \quad (5)$$

Plugging the typical values for n into the exponent on t in Eq. 5 gives a range of 0.0 to -0.005 for $-n/(2-n)$, which is a factor of 4 to 12 smaller than the measured values. This is taken to indicate that rate dependent yield does not significantly affect the ballistic limit velocity of blunt fragments. It is thought that the size dependence in Eq. 1 results more from the fragmentation of the projectile and target plate than from the plasticity. In fact the ballistic limit velocity for pointed bullets given in Ref. 12 has no size dependence, and pointed bullets do not fragment the target plate, which is more in keeping with the small size exponents calculated for rate dependent yield in the dimensional analysis performed above.

The constants for 2024-T3 aluminum striking 2024-T3 aluminum and mild steel striking 2024-T3 aluminum listed below were taken from Thor 41, Ref. 10, and Thor 47, Ref. 11, respectively.

mild steel striking 2024-T3 aluminum plate:

$$\begin{aligned} C_b &= 4.13 \times 10^4 \text{ cm/s} \\ b &= 0.941 \\ f &= -0.038 \\ h &= 1.098 \end{aligned}$$

2024-T3 aluminum striking 2024-T3 aluminum plate:

$$\begin{aligned} C_b &= 9.28 \times 10^4 \text{ cm/s} \\ b &= 0.972 \\ f &= -0.105 \\ h &= 1.010 \end{aligned}$$

Note that application of Eq. 1 to other combinations of projectile and target metals as well as other steel and aluminum alloys requires performing more ballistic limit tests to determine the parameters C_b , b , f , and h . Lacking the exponents for other alloys of steel and aluminum has forced the procedure of calculating the ballistic limit of all steel alloy projectiles as if they were mild steel and the ballistic limit of all aluminum alloy projectiles as if they were 2024-T3 aluminum.

Equation 1 is shown plotted along with some test data in figure 2-3 for reference.

2.3.2 First Plate Hole Diameter

There are few relations for hole diameter as a function of impact velocity published in the literature. Most, if not all, are empirical relations specialized for particular combinations of projectile and target materials. Another drawback to the published empirical fits is they were chosen on the basis of convenience and are not based on physical principles. Hence, they can not be confidently extrapolated to large impact velocities.

Lacking a satisfactory alternative, a new fit to available test data has been performed based on the known asymptotic limit the hole diameter relation must take at large impact velocities. This fit is described below in two sections; section 2.3.2.1 for normal impacts and section 2.3.2.2 for oblique impacts.

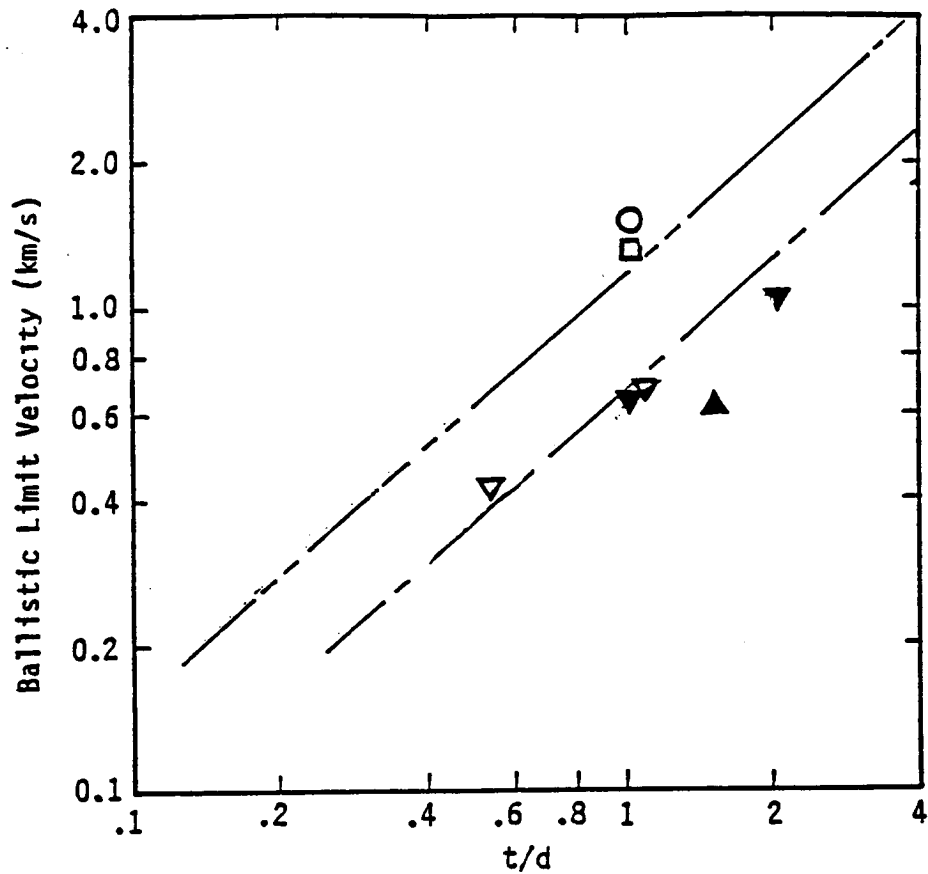
2.3.2.1 Normal Impacts. The approach taken here for fitting hole diameter data is an extension of scaling the particle velocity flow fields produced in thin plates by impact with projectiles hydrocode study described in Ref. 13.

The hole diameter D_H produced in a target plate by a projectile with diameter d , density δ , and closing velocity V , is expected to be a function of projectile parameters d , δ , and V , and target strength parameter Y , thickness t , and density ρ . Because there are 7 parameters to the problem and 3 fundamental units, the pi theorem of dimensional analysis requires there be 4 independent groups of dimensionless parameters governing the problem. The 4 pi groups are related by a function f not restricted in the form it may take by this dimensional analysis:

$$D_H/d = f(\rho V^2/Y, t/d, \rho/\delta). \quad (6)$$

Equation 6, though true, is not particularly helpful, because the functional dependence f is unknown and thus must be determined by experiment. Furthermore, f is a function of three pi groups, thus determining f will require a large test program. The hole diameter, however, can be shown to be a function of fewer pi groups in the limit of large impact velocities, greatly simplifying the amount of testing required.

As the impactor velocity increases, the final position of the hole lip will get further from the impact point. It seems intuitive to expect that the further the final hole lip is from the nonzero diameter impactor the less the motions produced in the target plate will depend on details of the source region and details of the energy transfer from the impactor to the target. It also seems intuitive to expect the motions from a nonzero diameter projectile in the far field to approach the motions from a point source.



CALCULATIONS

—— ——— Eq. 1 Mild Steel Striking Aluminum
 ——— ——— Eq. 1 Aluminum Striking Aluminum

TEST DATA ○ Al→Al Reference 18 Spheres
 □ Al→Al Reference 25 1/8" Cylinders
 ▼ St→Al Reference 19 1/4" Spheres
 ▽ St→Al Reference 19 15/32" Spheres
 ▲ St→Al Reference 14 Cylinders

Figure 2-3. Comparison of ballistic limit velocity relations.

If this intuition is correct and there is a connection between the motions produced by a point source and the far-field motions produced by a nonzero diameter projectile impacting at finite impact velocity, then the question becomes, "What is the sequence of motions from nonzero diameter impactors that approaches the point source in the limit of d approaching zero?"

This problem was examined in detail in Ref. 13, where it was shown through a hydrocode parameter study that the motions in the target plate produced by finite diameter projectiles approach the same point source motions in the far field when the parameters,

$$C_1 = dV^{0.83}\delta^{0.265} \quad \text{for } d/t(V/c)^{0.83}(\delta/\rho)^{0.265} < 200, \quad (7)$$

and,

$$C_2 = dV^{0.83}\delta^{0.265}f(t/d) \quad \text{for } d/t(V/c)^{0.83}(\delta/\rho)^{0.265} > 200, \quad (8)$$

are constant, and c is the zero pressure sound speed in the target plate.

Equation 7 applies to most combinations of t/d and V that are of interest, therefore, the rest of this analysis is limited to scaling with Eq. 7.

A dimensional analysis of the hole diameter relation for point source impactors proceeds along the same lines as that leading to Eq. 6; however, now d , V , and δ do not enter the problem individually. They enter the problem as the one parameter C_1 . Thus there are 5 parameters to the hole diameter relation for point sources and therefore 2 pi groups,

$$D_H/t = f[C_1/(t(Y/\rho)^{0.415}\rho^{0.265})]. \quad (9)$$

Substituting Eq. 7 into Eq. 9 gives,

$$D_H/t = f[d/t(\delta V^2/Y)^{0.415}(\delta/\rho)^{-0.15}]. \quad (10)$$

Equation 10 has been used to fit hole diameter data from the impact of 2024-T3 aluminum alloy plates by glass (Ref. 14), 6061-T6 aluminum plates struck by 1100-O aluminum (Ref. 15), and 2024-T3 plates struck by steel and TalOW projectiles (Ref. 16). The resulting collapse of the data onto a single curve is shown in figure 2-4 and is seen to be quite reasonable.

The functional dependence f in Eq. 10 that the dimensional analysis is unable to determine a priori must be determined from the experimental data plotted in figure 2-4. Over the limited range of $d/t(\delta V^2/Y)^{0.415}$ shown plotted in figure 2-4 with the available data f is adequately represented by the equation,

$$D_H/t = 11.02 [1 - \exp(-d/t(\delta V^2/Y)^{0.415} (\delta/\rho)^{-0.15}/29.9)] \quad (11)$$

Hole Diameter Data

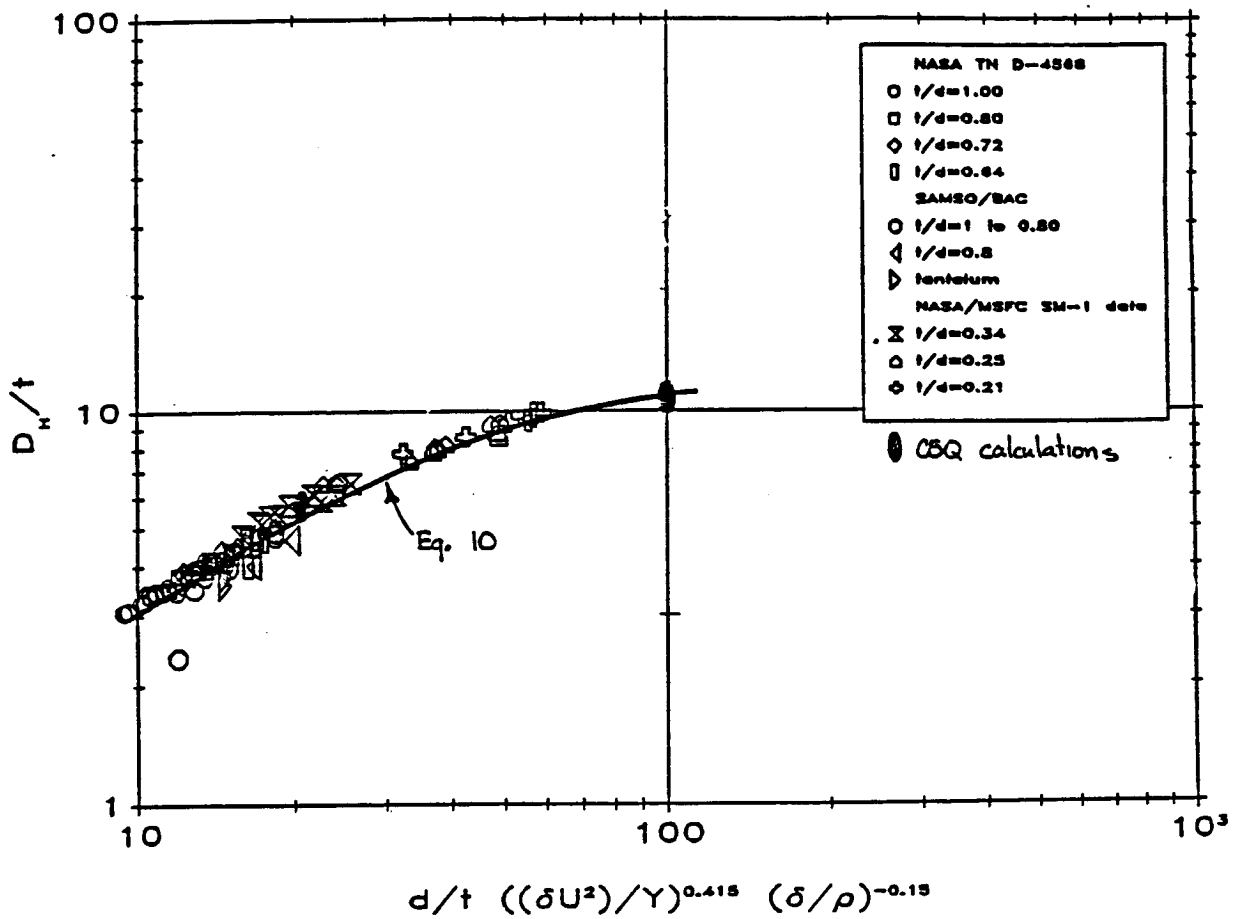


Figure 2-4. Scaled hole diameter data.

It should be reiterated that Eq. 11 strictly applies only to the far field motions from impact with nonzero diameter finite impact velocity sources. Also, even though Eq. 11 can be confidently used to extrapolate to impact velocities larger than can be tested, Eq. 11 can not be used to confidently extrapolate to all combinations of t/d and large impact velocities. This conclusion stems from having to determine the function f empirically. To be precise, Eq. 11 should only be used for $d/t(\delta V^2/Y)^{0.415}(\delta/\rho)^{-0.15} < 100$ (the end of hydrocode data in figure 2-4). Thus, for $t/d=1.0$, Eq. 10 can be used confidently to extrapolate to 100 km/s; while, for $t/d=0.5$, it can only be used with confidence up to 45 km/s.

It has been found empirically that Eq. 11 is acceptable close to the source also, so long as the hole diameter is precluded from becoming smaller than the projectile diameter. This is achieved in the PEN4 coding by testing whether the value of D_H calculated with Eq. 11 is smaller than d , and when so setting D_H to d .

This unexpected result is illustrated in figure 2-5, where a set of data from Ref. 17 is adequately fitted by the procedure described above, even though these data were not included in the original fit to derive Eq. 11.

2.3.2.2 Oblique Impacts. Allowing for the possibility of oblique impacts introduces a new parameter into the dimensional analysis, the impact angle θ . One extra variable introduces one extra pi group, because there is no increase in the number of fundamental dimensions to the problem. Impact angle is dimensionless, hence it forms its own pi group. Thus, for oblique impacts Eq. 9 may be rewritten as,

$$D_H/t = f[d/t(\delta V^2/Y)^{0.415}(\delta/\rho)^{-0.15}, \theta]. \quad (12)$$

The function f is not determined by the dimensional analysis, hence it must be determined by fits to test data.

A data search for oblique impact hole diameter data has been performed for task 1 of this contract. A description of the data search is given in Appendix A. The test data were fitted with the relation,

$$D_H = D_H(\theta=0) [1 - \exp\{(85^\circ - \theta)/9.5^\circ\}]. \quad (13)$$

The parameter $D_H(\theta=0)$ is the hole diameter for normal impact and is calculated with Eq. 11, the angle of obliquity θ is in degrees, d is the projectile diameter, and U is the impact velocity. The parameter D_H in Eq. 13 is an equivalent hole diameter calculated from the experimentally measured hole areas,

$$D_H = 2 [A_H (\cos\theta)/\pi]^{0.5} \quad (14)$$

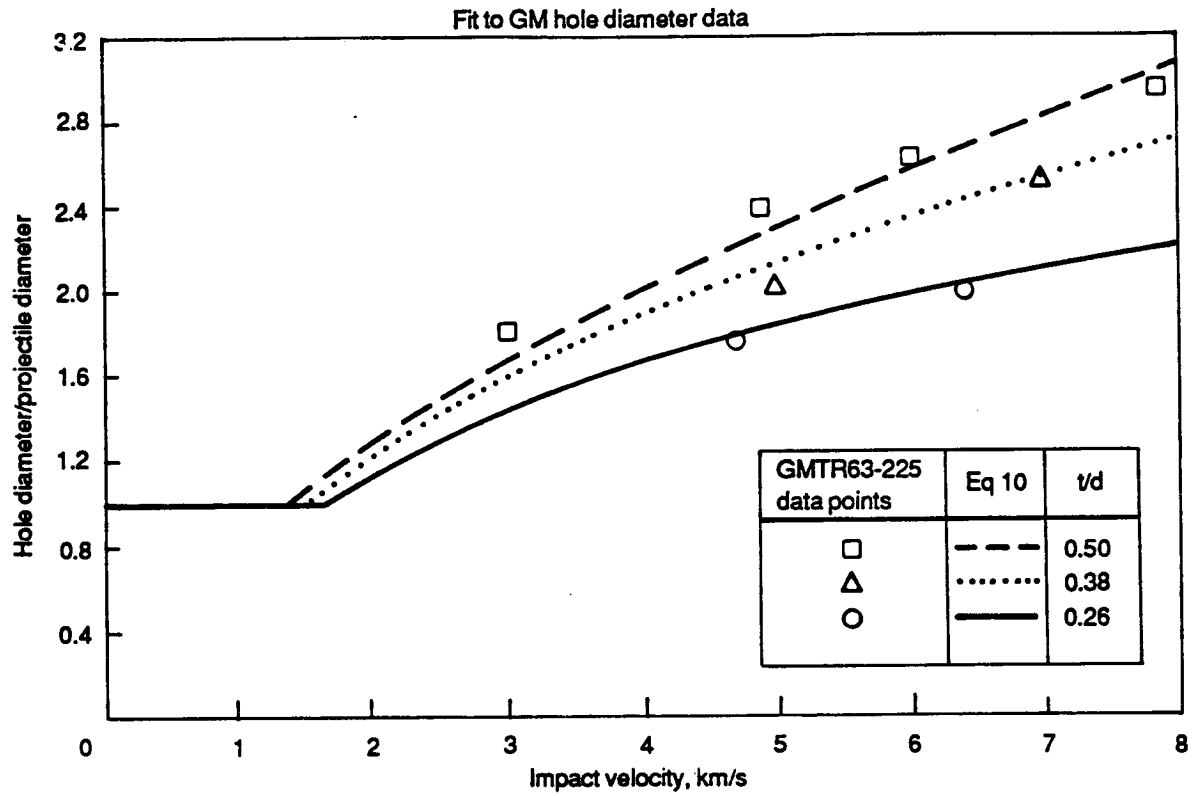


Figure 2-5. Comparison of hole diameter relation with small impact velocity test data.

For reference, Eq. 13 is cross plotted in figure 2-6 with some test data collected at NASA/MSFC under this contract. It should be noted that Eq. 13 underpredicts the hole diameter from the oblique impact of steel projectiles. This is discussed more fully in Appendix A.

2.3.3 Residual Velocity

As was the case for ballistic limit velocity relations, a variety of residual velocity relations have been published in the literature. Thus, the residual velocity relation from the authoritative source for DoD methodologies, Ref. 12, was examined in an effort to resolve the issue for construction of PEN4. However, it was found that the residual velocity relation from Ref. 12 can not be used for all combinations of projectile and target materials contemplated for use in PEN4 without modification. The residual velocity relation from Ref. 12 (which was developed for impact velocities smaller than 3 km/s) is plotted in figure 2-7 for three t/d's. The ballistic limit velocity needed to calculate the residual velocity was calculated with Eq. 1. Note, however, that the residual velocity relation from Ref. 12 underpredicts by as much as 85% the large impact velocity residual velocity test data and hydrocode calculations for hard steel spheres striking aluminum plates also plotted in figure 2-7. This result was perplexing, because the residual velocity relation taken from Ref. 12 is well founded in theory and experiment. This prompted an examination of assumptions made in the derivation. It was found that this residual velocity relation was derived assuming that the projectile was deformed and thus was not a good approximation to the impact of hard steel ball bearings with aluminum plates. This prompted developing the following generalized derivation of the residual velocity relation as given in section 2.3.3.1 below. Experimental confirmation of the residual velocity relations is discussed in section 2.3.3.2. Oblique impact angles effects are discussed in section 2.3.3.3.

2.3.3.1 Derivation of the Residual Velocity Relations for Normal Impacts.

The following derivation is a generalization of the original derivation of residual velocity from plugging given by Recht and Ipson in Ref. 18. Their derivation, as well as this one, is constrained to apply to blunt projectiles plugging the target plate as illustrated in figure 2-8. Their key insight was to resolve the energetics of plugging into two parts. The first part involves the work done separating the plug from the plate, and the second part is a free collision between the plug and projectile where work is done deforming the plug and projectile and accelerating the plug to its final residual velocity. This can be written mathematically as Eq. 16,

$$E_t = E_f + W_p + T_r, \quad (16)$$

where E_t is the total energy of impact, E_f is plastic work done deforming the projectile and plate plug, W_p is the plastic work done separating the plug from the plate, and T_r is the residual kinetic energy of the projectile and plate plug.

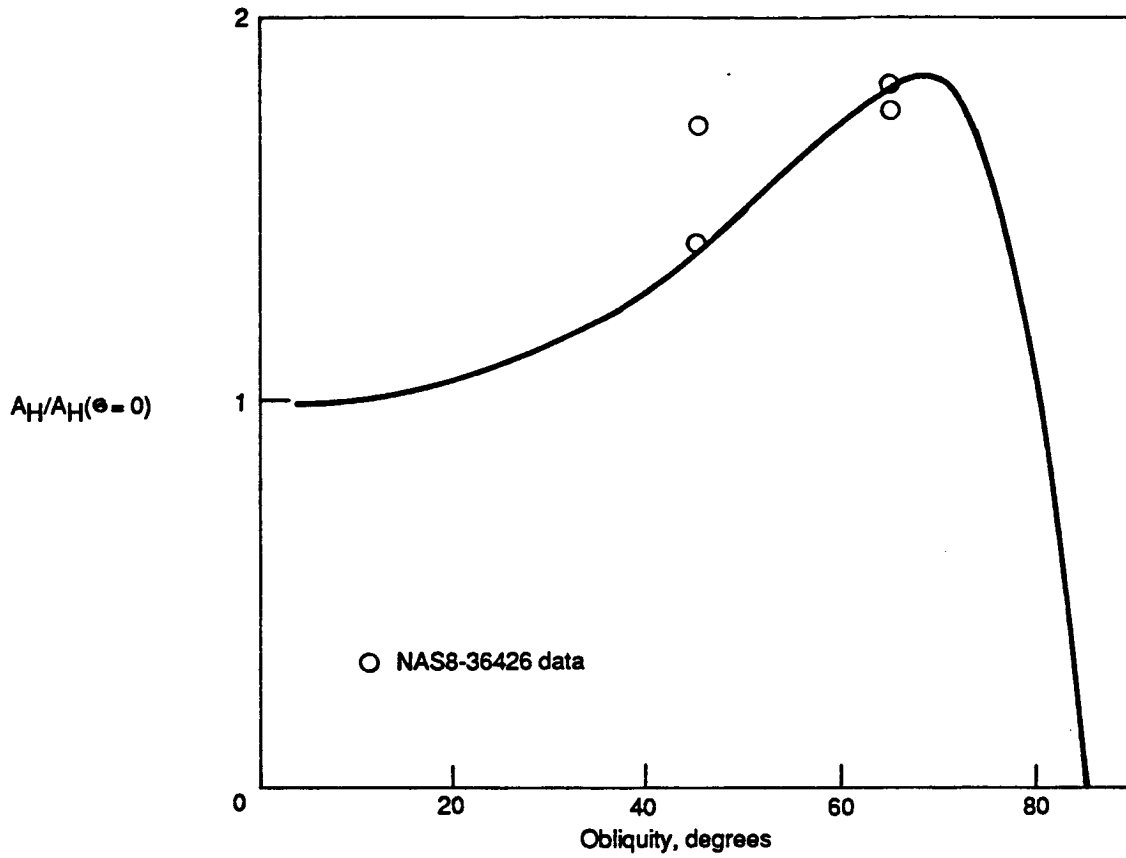


Figure 2-6. The hole diameter relation as a function of angle of obliquity cross plotted with test data.

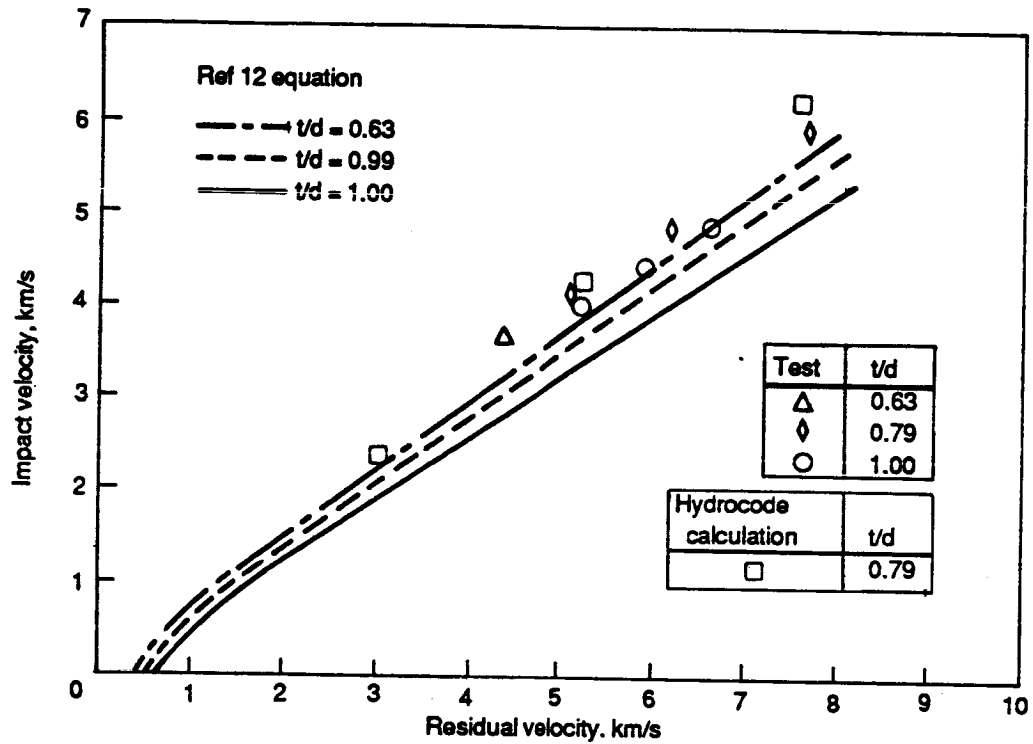


Figure 2-7. Comparison of DoD residual velocity relation with large impact velocity data.

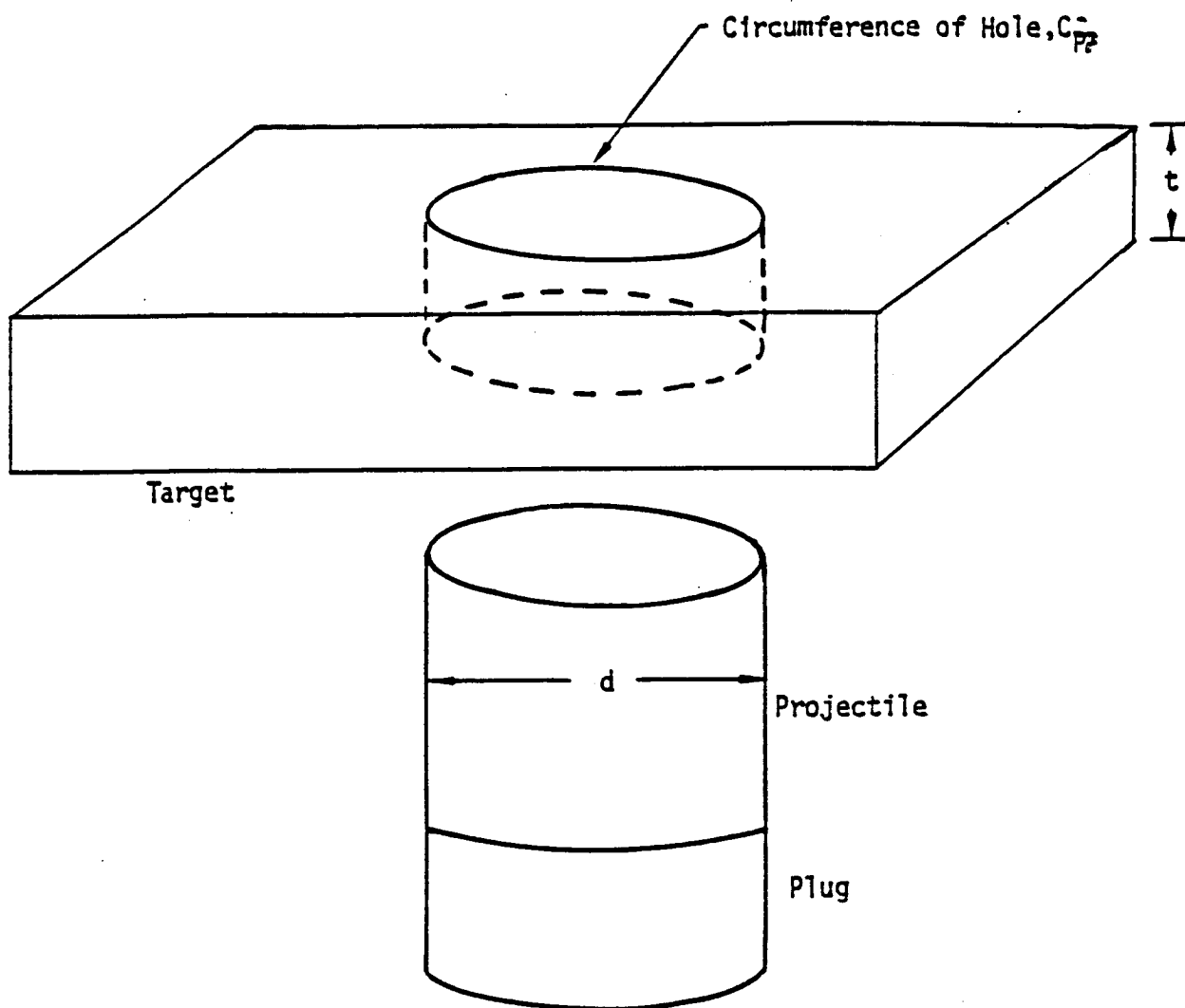


Figure 2-8. The geometry of plate plugging.

All three terms do not necessarily occur for every combination of t/d and V . For example, if the projectile is rigid, then $E_f = 0$. Three cases have been identified,

1. The projectile is rigid and sharp;
2. The projectile is rigid and blunt;
3. The projectile and plate plug deform.

The energy lost to projectile and plug deformation is calculated by treating the collision of the projectile with a plate plug free to slip within the plate. (The plastic work required to separate the plug from the plate, W_p is calculated below). It can be shown that (see Ref. 19),

$$E_f = m_s / (m + m_s) 1/2 m V^2 (1 - \epsilon^2), \quad (17)$$

where m is the projectile mass, m_s is the plate plug mass, V is the impact velocity and ϵ is the coefficient of restitution for the projectile plate plug material combination. For an elastic impact (rigid projectile and plug) $\epsilon = 1$ and for an inelastic impact (projectile and plug deform) $\epsilon = 0$.

The plastic work required for separating the plate plug from the plate is calculated by substituting Eq. 17 into Eq. 16, solving for W_p ,

$$W_p = 1/2 m V^2 - m_s / (m + m_s) 1/2 m V^2 (1 - \epsilon^2) - 1/2 m_s V_r^2 - 1/2 m V_{r2}^2 \quad (18)$$

where V_r is the residual velocity of the plate plug and V_{r2} is the residual velocity of the projectile.

Next assume that the plastic work required for perforation does not increase with impact velocity. Thus at the ballistic limit velocity, where $V = V_{50}$ and $V_{r2} = 0$,

$$W_p = 1/2 m V_{50}^2 - [m_s / (m + m_s)] 1/2 m V_{50}^2 (1 - \epsilon^2) - 1/2 m_s V_r^2 \quad (19)$$

Finally, we observe that the kinetic energy in the plate plug at the ballistic limit is usually small for thin plate targets, thus,

$$W_p = 1/2 m V_{50}^2 - [m_s / (m + m_s)] 1/2 m V_{50}^2 (1 - \epsilon^2) \quad (20)$$

Substituting Eqs. 17 and 20 into Eq. 16 and solving for the square of the residual center-of-mass velocity of projectile and plug gives (see Ref. 19 for the equations for T_r for free impact of two bodies in terms of V_r , V_{r2} and V_{cm})

$$V_{cm}^2 = \{m / (m + m_s) [(m + \epsilon^2 m_s) / (m + m_s)] (V^2 - V_{50}^2) + m m_s / (m + m_s)^2 [V_r - V_{r2}]^2\} \quad (21)$$

With Eq. 21 we can now address the 3 cases identified previously,

Case 1. Projectile is rigid and sharp.

If the projectile is rigid and sharp, then no plate plug forms so

$$m_s = 0 \quad (22)$$

Substituting Eq. 22 into Eq. 21 gives,

$$V_{cm} = (V^2 - V_{50}^2)^{1/2}. \quad (23)$$

Case 2. Projectile is rigid and blunt, and plug is rigid.

If the projectile and plug are rigid, then free collision of the plug and projectile is elastic, so $\epsilon = 1$. Substituting $\epsilon = 1$ into Eq. 21 gives,

$$V_{cm} = \left\{ \frac{m}{(m+m_s)} (V^2 - V_{50}^2) + \frac{mm_s}{(m+m_s)^2} [V_r - V_{r2}]^2 \right\}^{1/2} \quad (24)$$

Case 3. Projectile deforms and is blunt and plug deforms also.

For this case $\epsilon = 0$. Substituting $\epsilon = 0$ into Eq. 21 gives,

$$V_{cm} = \left\{ \left[\frac{m}{(m+m_s)} \right]^{1/2} (V^2 - V_{50}^2) + \frac{mm_s}{(m+m_s)^2} [V_r - V_{r2}]^2 \right\}^{1/2}. \quad (25)$$

Equation 25 reduces to the familiar residual velocity formula first derived by Recht and Ipson, Ref. 18, when the plate plug and projectile have the same residual velocities $V_r = V_{r2}$,

$$V_{cm} = m/(m+m_s) (V^2 - V_{50}^2)^{1/2}. \quad (26)$$

Contrary to the assertion made by Ipson and Recht in Ref. 20, Eq. 26 for residual velocity does not apply to the center of mass velocity of a two particle system (projectile and plate plug) without the additional assumption that the projectile and plate plug have the same velocity.

Equation 24 is new and was first derived by A. B. Zimmerschied of The Boeing Company in the form of Eq. 27 below for the special case when the projectile and plate plug have the same residual velocities,

$$V_{cm} = m/(m+m_s)^{1/2} (V^2 - V_{50}^2)^{1/2}. \quad (27)$$

The observation that there is a range of formulae for the residual velocity may dependent on the coefficient of restitution for the impact, Eq. 21, is new. For the special case of projectile and plate plug traveling together Eqs. 26 and 27 may be summarized as,

$$V_{cm} = R (V^2 - V_{50}^2)^{1/2}, \quad (28)$$

where,

$$m/(m+m_s) < R < m/(m+m_s)^{1/2}. \quad (29)$$

2.3.3.2 Comparison With Test Data. The first comparison with test data shows the fit to the data plotted in figure 2-9 has been improved. The test data were collected with hard steel ball bearings striking 2024-T6 aluminum plate. The three points plotted as open squares are results from 2-d hydrocode calculations. The curves plotted in figure 2-9 were calculated with Eq. 27 using Eq. 1 for the ballistic limit velocity. Note that Eq. 27 agrees well with the hydrocode calculations and with the test data collected with impact velocities smaller than 5 km/s. However, the test data diverge from Eq. 27 at larger impact velocities. It is not clear why the test data diverge from Eq. 27 while the hydrocode calculations do not. Most likely some aspect of the impact has not been modeled correctly by the hydrocode; i.e., temperature effects on the work done to plastically deform the projectile and plug, the work done to melt the projectile or target, or the work done on the alpha to epsilon phase transition in iron (note, however, effects from miscalculating the alpha to epsilon phase transition should occur at impact velocities closer to 2 km/s).

Another check on Eqs. 26 and 27 was performed with four sets of residual velocity test data. The experimentally measured power on the mass ratio $m/(m+m_s)$ was determined by plotting $V_r/(V^2 - V_{50}^2)^{1/2}$ versus $m/(m+m_s)$ on log-log paper. The exponent on the mass ratio is 1/2 for rigid steel spheres plugging aluminum plates in figures 2-10a) and b) as predicted by Eq. 27. The data plotted in figure 2-10a) were taken from Ref. 21, and the data plotted in figure 2-10b) were taken from Ref. 16. The mass ratio exponent is 1 in figures 2-10c) and d) for deformable steel spheres and cylinders that plug steel plate as predicted by Eq. 26. The data plotted in figure 2-10c) were taken from Ref. 21, and the data plotted in figure 2-10d) were taken from Ref. 18.

As a further check on the validity of variable mass ratio exponents, fits to deforming projectile and nondeforming projectile residual velocity as a function of impact velocity, data are shown in figures 2-11 and 2-12. Fits to the Ref. 22 data on aluminum spheres perforating aluminum plates are shown in figures 2-11a) and 2-11b). Aluminum spheres will deform so Eq. 26,

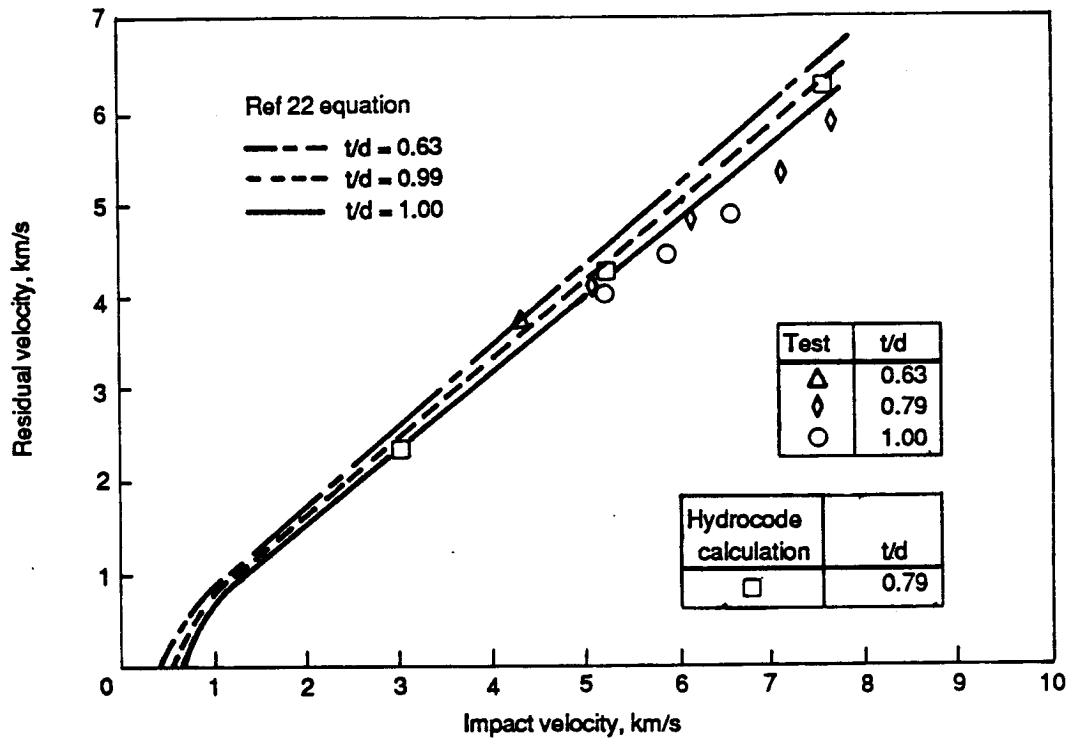
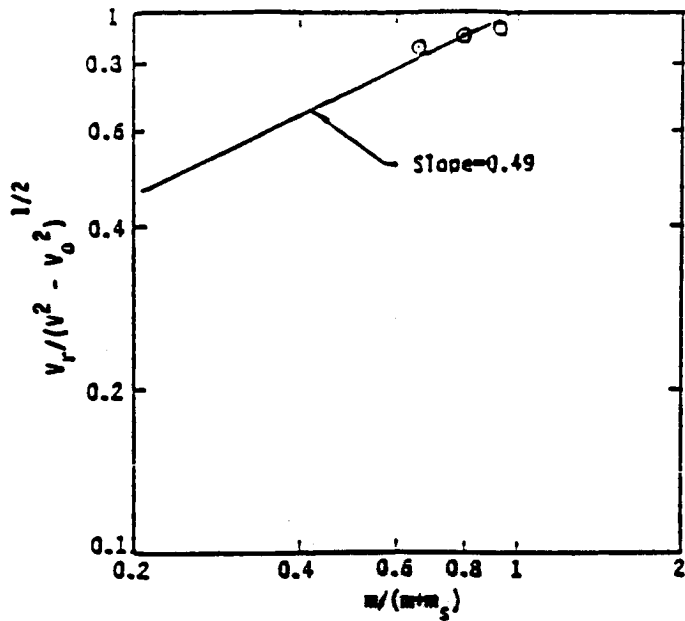


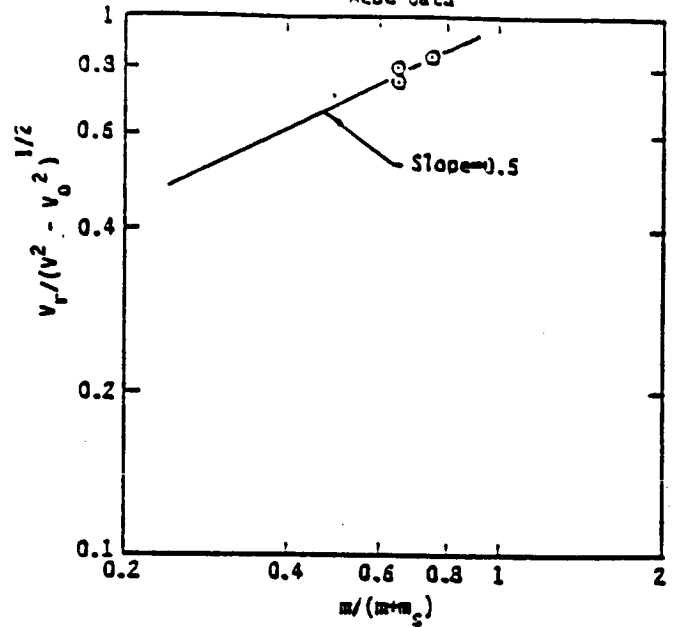
Figure 2-9. Comparison of Eq. 27 with Large Impact Velocity Test Data.

NWC-TP-5844 Data



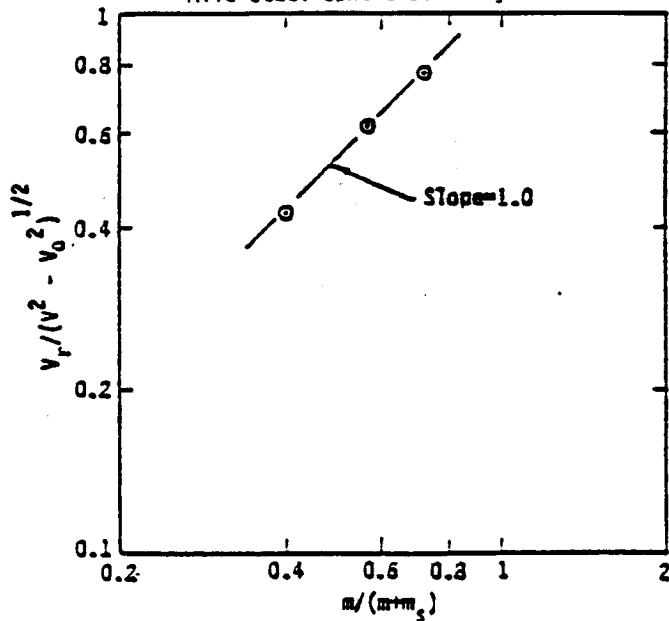
a) Steel Sphere - Aluminum Plate

AEDC Data

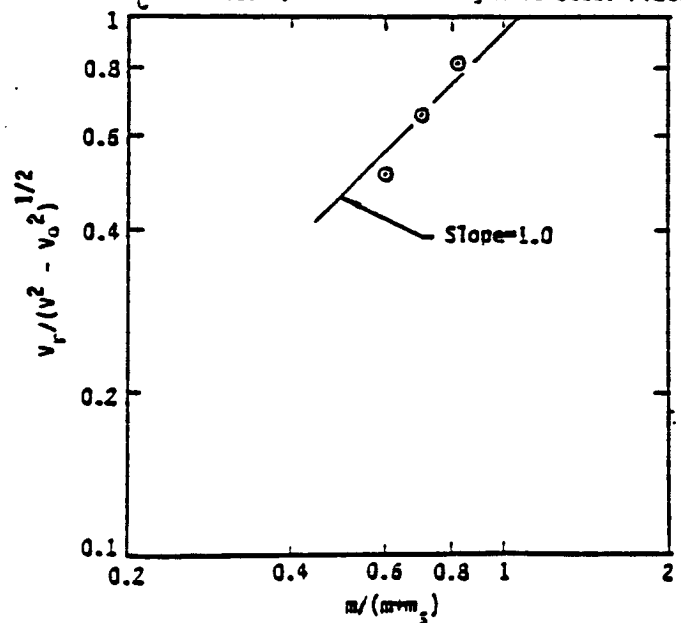


b) Steel Sphere - Aluminum Plate

Mild Steel Sphere Striking US Armor



c) Steel Sphere - Armor Steel

R_c 30 Steel Cylinders Striking Mild Steel Plates

d) Steel Cylinder - Mild Steel

Figure 2-10. Residual velocity mass ratio exponent for four projectile/target combinations.

should apply and the mass ratio exponent is 1. (The mass ratio exponent of 1 fit is shown in figure 2-11b). The fits to the Ref. 23 data for hard steel spheres perforating aluminum plates are shown in figures 2-12a) and 2-12b). Hard steel spheres will not deform, so Eq. 27 should apply and the mass ratio exponent is 1/2 as is shown in figure 2-12b) while the exponent of 1 for deformable projectiles clearly does not fit the data as shown in figure 2-12a).

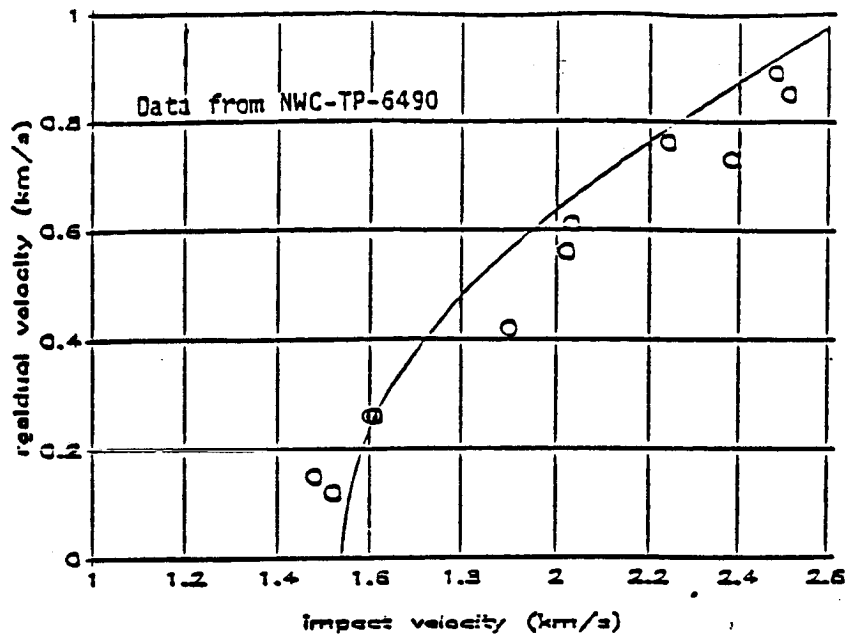
Application of Eq. 27 to large impact velocities has centered on how much of the mass holed out of the plate should be applied towards the m_s term in Eq. 25. The conclusion in Ref. 18 was that only the largest plate plug fragment should be used. Thus, for impact velocities sufficient to fragment the plate plug, m_s should decrease rapidly with impact velocity. Therefore the residual velocity should increase.

The above line of reasoning is not thought correct by the present authors because the projectile is decelerated to nearly its final residual velocity by the rarefaction arriving from the rear of the target. Thus, for thin target plates, the volume of target material initially accelerated by the projectile during the first transit of the target by the shock, and further accelerated by the rarefaction returning to the projectile from the rear of the target plate, is nearly equal to the plug volume described in figure 2-8. Therefore the derivation given for Eq. 21 is considered by the present authors approximately correct at large impact velocities. This has been shown substantially true by figure 2-9.

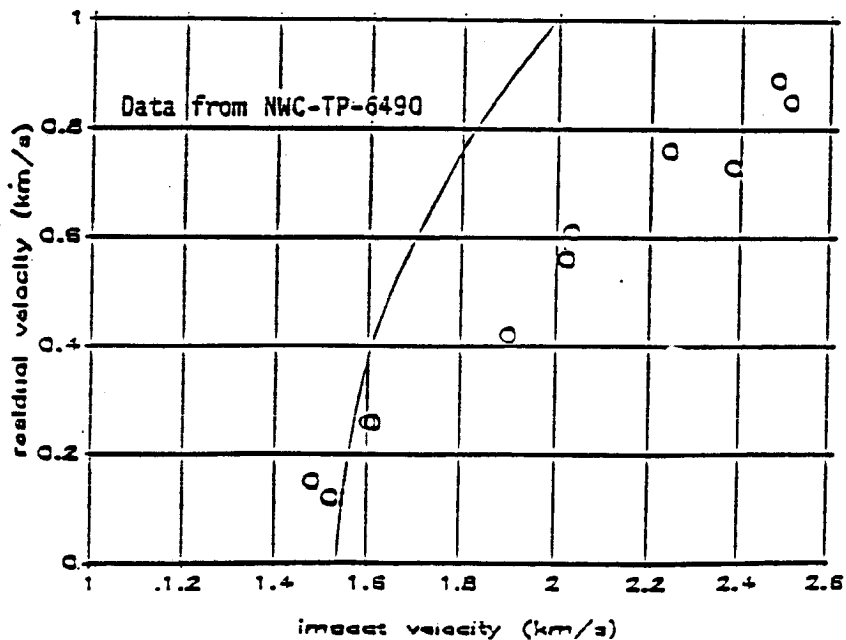
2.3.3.3 Oblique Impacts. The decrease in velocity experienced by a projectile during oblique impacts results in the projectile turning towards the normal of the backside of the target plate. However, as the impact velocity becomes much larger than the ballistic limit velocity, this effect is expected to become smaller. The theory for oblique impacts of blunt deformable projectiles onto flat plates developed by Recht in Ref. 18, and repeated in the Penetration Equations Handbook Ref. 12, can be used to illustrate this. Recht has shown that the residual velocity equation for the oblique impact of deformable projectiles onto flat plates is,

$$V_{cm} = \cos\beta \, m / (m + m_s) (V^2 - V_{50}^2)^{1/2}, \quad (30)$$

where the plate plug mass m_s is now $m_{sn}/\cos\theta$, where m_{sn} is the normal impact plate plug mass. The angle β is the change in angle of obliquity. The relationship of β to θ is illustrated in the vector diagram in figure 2-13. Using Recht's equation for β as a function of impact velocity gives the curves plotted in figure 2-13 for impacts at 45, 60 and 80 degrees. Note that for impact velocities larger than 1.4 times the ballistic limit velocity (which for t/d 's less than 0.4 is less than 1 km/s) the change in angle of obliquity from the impact is less than 10 degrees. Thus the $\cos\beta$ term in Eq. 30 is greater than 0.98 for most impact velocities of interest. Thus the

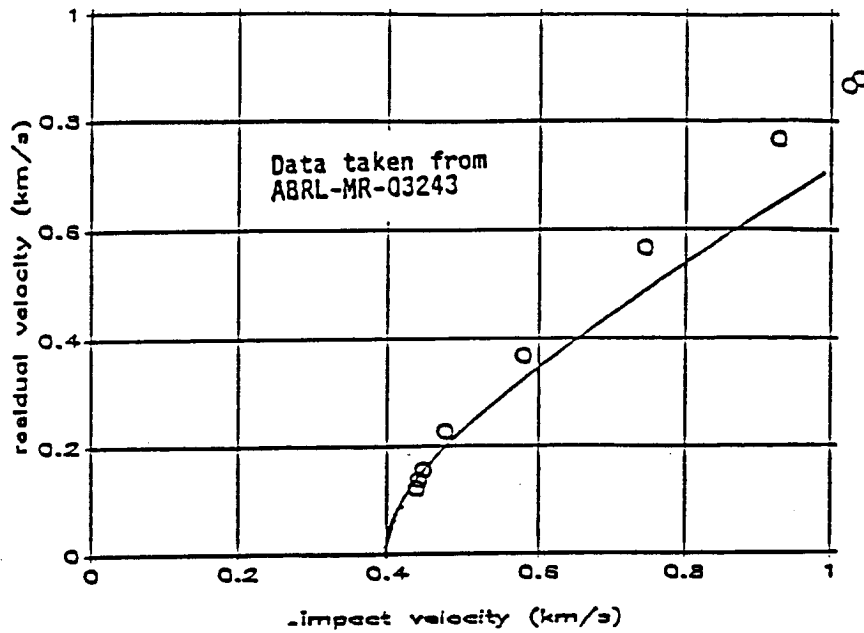
aluminum spheres striking aluminum plates $t/d=1.0$ 

a) Data Comparison with Deformable Projectile Calculation

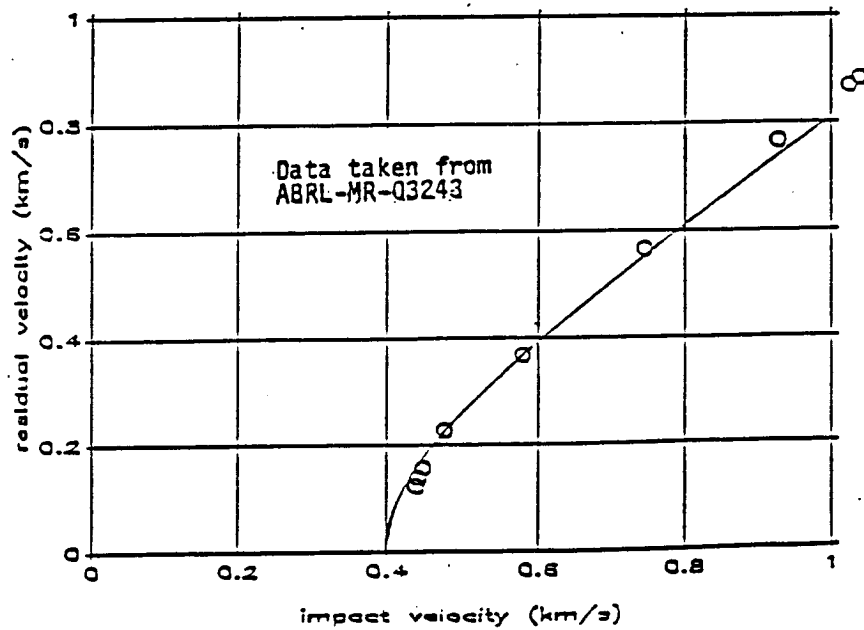
aluminum spheres striking aluminum plates $t/d=1.0$ 

b) Data Comparison with Rigid Projectile Calculation

Figure 2-11. Comparison of residual velocity prediction with test data for aluminum spheres striking aluminum plates.

steel spheres striking aluminum plates $t/d=0.5$ 

a) Deformable Projectile

steel spheres striking aluminum plates $t/d=0.5$ 

b) Rigid Projectile

Figure 2-12. Comparison of residual velocity prediction with test data for hard steel spheres striking aluminum plates.

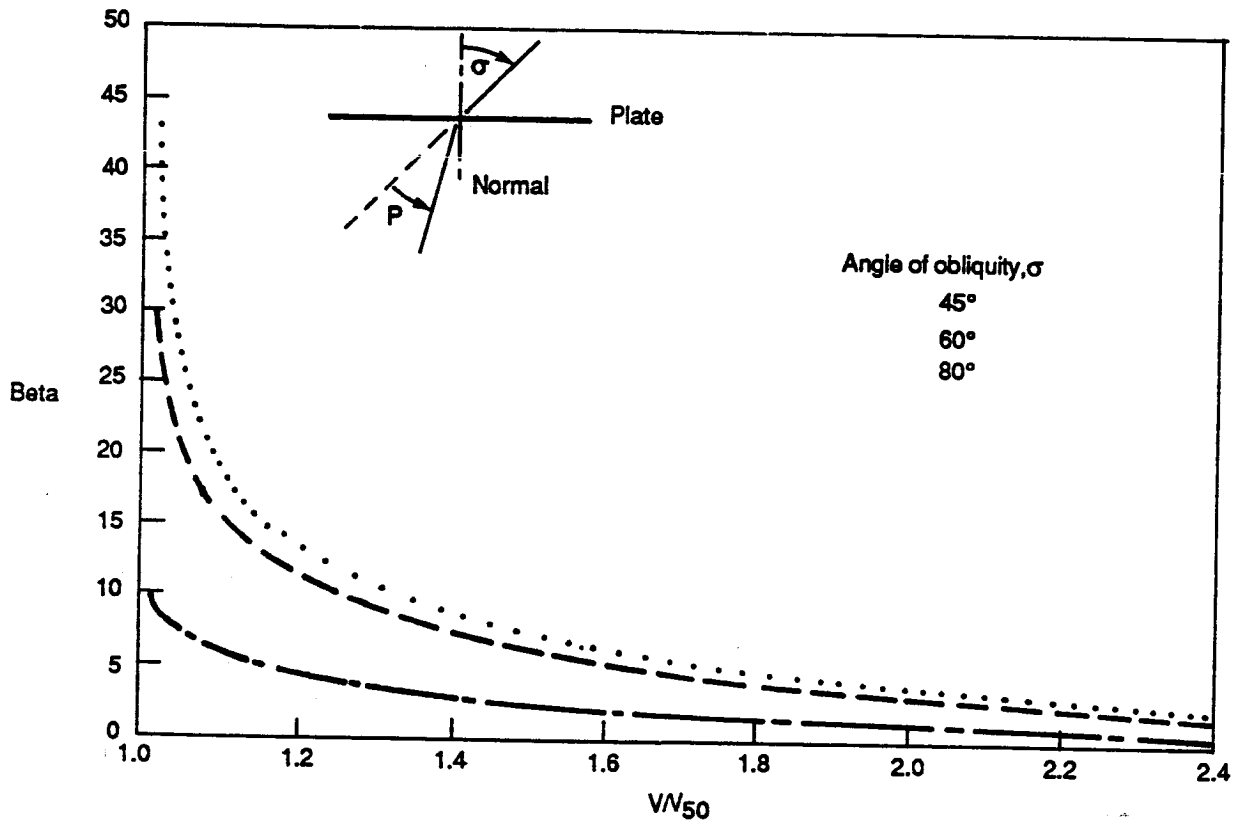


Figure 2-13. Change in angle of obliquity as a function of impact velocity.

most significant obliquity effect in Eq. 30 is the increase in mass of the plate plug at oblique angles. Thus, the increase in plate plug mass is the only oblique angle effect included in the calculation of residual velocity in PEN4.

2.3.4 Projectile Fragmentation Threshold Velocity

Projectile fragmentation has not been treated explicitly in previous DoD penetration codes, hence previous work gives little guidance. For the most part, impact velocities of interest to the DoD have been too small to fragment projectiles. Thus the DoD methodology outlined in Ref. 12 uses a constant threshold velocity for projectile fragmentation, V_f , more as a delimitation of the applicability of the methodology than as an estimate of V_f . The estimate for V_f given in Ref. 12 was based on a very small data base and was shown to be off up to a factor of 2 for certain t/d 's and projectile diameters (Refs. 3 and 24) requiring a review of the data and possible functional forms V_f may take. The functional form of V_f is developed in section 2.3.4.1 along with the relations used in PEN4, and the oblique impact relations are given in section 2.3.4.2.

2.3.4.1 Normal Impacts. The form of the fragmentation threshold velocity formula was chosen on the basis of a dimensional analysis of V_f . This analysis was first performed in Ref. 3 and is reproduced below.

The velocity V_f is expected to depend on target plate thickness t , projectile diameter d , and some target projectile material properties. For simplicity we will only consider one combination of target and projectile materials. Thus the only important material parameters are those describing the projectile fragmentation kinetics. These are not conclusively identified in the dimensional analysis that follows, so some general possibilities are considered. First consider one fragmentation kinetics parameter, then two or more.

If there is only one fragmentation kinetics parameter, identified as J , then V_f is expected to be a function of the following variables,

$$V_f = f(t, d, J). \quad (31)$$

Since V_f , t , and d only have units of length and time, J may only have units of length and time. Without loss of generality, we may assign J to have the units $L^a T$ (where L denotes units of length, T denotes units of time, and the exponent a is, not necessarily an integer). Performing a dimensional analysis on Eq. 31 gives

$$V_f J / d^{(1+a)} = f(t/d). \quad (32)$$

Thus at fixed t/d , V_f is proportional to $d^{(1+a)}$ (i.e., V_f has a power-law dependence on d) and for a fixed fragment size, V_f is some function of t/d ,

not identifiable by this dimensional analysis; tests at the fixed size must be performed to determine the function f .

As an aside, note that if $a = -1$, then Eq. 32 becomes

$$V_f J = f(t/d) \quad (33)$$

and V_f scales geometrically; and, if a is not equal to -1 , then V_f does not scale geometrically but scales with the projectile size. Therefore, if subsize experiments are desired, then the material parameter J must be varied. For example, if a similar experiment is to be performed in half size, then the half size J must equal $(1/2)^{(1+a)}$ of the full-scale J . This result is significant and must be borne in mind when performing scaling or subsize tests.

Returning to the original discussion on the functional form of V_f , if there are two fragmentation kinetics parameters, J and K , it is possible for J and K to also have units of mass, however; if one has units of mass then they both must have units of mass. Without loss of generality, we may assume J has units of $ML^a T^b$ and K has units of $ML^c T^d$, where M denotes units of mass. Note that J and K must always occur in the dimensional analysis as J/K to divide out the units of mass. This effectively results in only one material parameter $J' = J/K$, thus Eq. 32 also results from this dimensional analysis.

If neither of the two fragmentation kinetics parameters contain the unit mass, then J has the units $L^a T^b$ and K has the units $L^c T^d$. The parameters may be redefined as $J' = J/K^{1/(a-b)}$, which has the units L , and $K' = (J/K^{a/b})^{1/(1-a/b)}$, which has the units T . Thus a dimensional analysis gives,

$$V_f K' / J' = f(t/d, J'/d) \quad (34)$$

Equation 34 results in size scaling, analogous to the size scaling result from Eq. 32; however, at fixed t/d , V_f varies as a function of d , which has not been determined by this dimensional analysis and therefore not necessarily a power-law as the functional form was in Eq. 32.

Dimensional analysis on problems with 3 or more fragmentation kinetics parameters will result in equations analogous to Eq. 34, only with additional pi-groups of material parameters in the functional dependence.

In summary, the five conclusions may be drawn from the above discussion.

1. Rate dependent fragmentation necessarily results in size dependent scaling of the threshold velocity for fragmentation. Geometric scaling will not result in similar experiments.
2. If there is only one material parameter describing the fragmentation rate dependence, then at fixed t/d , V_f varies as a power of d .

3. If there are two material parameters describing the fragmentation rate dependence, then at fixed t/d , V_f will vary as a power of d when the material parameters depend on mass, or V_f will depend on some general function of d when the material parameters do not depend on mass.
4. If there are three or more material parameters describing the rate dependent fragmentation, then at fixed t/d , V_f will vary as a general function of d .
5. At fixed diameter d , V_f will vary as some function of t/d , which is not required to be a power law.

The fragmentation threshold velocity relations reported here are the result of fitting test data with a relationship constrained to have a form dictated by the above dimensional analysis. Relationships are given for mild and hard 4340 steel projectiles and 2024-T3 projectiles.

The fragmentation kinetics parameters governing the threshold velocity for steel projectile fragmentation have not been identified. Hence, two relations are given, one for R_B 90 mild steel projectiles and the other for R_C 60 4340 steel projectiles. Both relations were taken from curve fits given in Ref. 24.

For R_B 90 mild steel projectiles striking aluminum plates use the larger of the following two relations:

$$V_f = 4.42 \times 10^4 \text{ cm/s } (t/d)^{-0.39}, \quad (35)$$

$$V_f = 1.39 \times 10^5 \text{ cm/s } d^{0.33} (t/d)^{0.42}. \quad (36)$$

Equation 35 applies to small t/d 's (mostly less than 0.5), and Eq. 36 applies to larger t/d 's (mostly larger than 0.5). Equations 35 and 36 are shown plotted in figure 2-14 for reference.

The relations for threshold velocity for fragmentation of 2024-T3 aluminum cylinders striking aluminum plate was developed from Boeing Independent Research and Development test data. The tests are documented in Ref. 25. No evidence was found for V_f depending on the diameter of projectile for fixed t/d for excursions in d of a factor of 4. Thus the relations used in PEN4 for V_f for 2024-T6 aluminum striking aluminum contain no dependence on d :

$$V_f = 1.45 \times 10^5 \text{ cm/s } (t/d)^{0.08} \quad \text{for } t/d > 0.1 \quad (37)$$

$$V_f = 3.40 \times 10^4 \text{ cm/s } (t/d)^{-0.55} \quad \text{for } t/d < 0.1 \quad (38)$$

Equations 37 and 38 only apply to 2024-T3 aluminum projectiles. No attempt has been made to incorporate material properties.

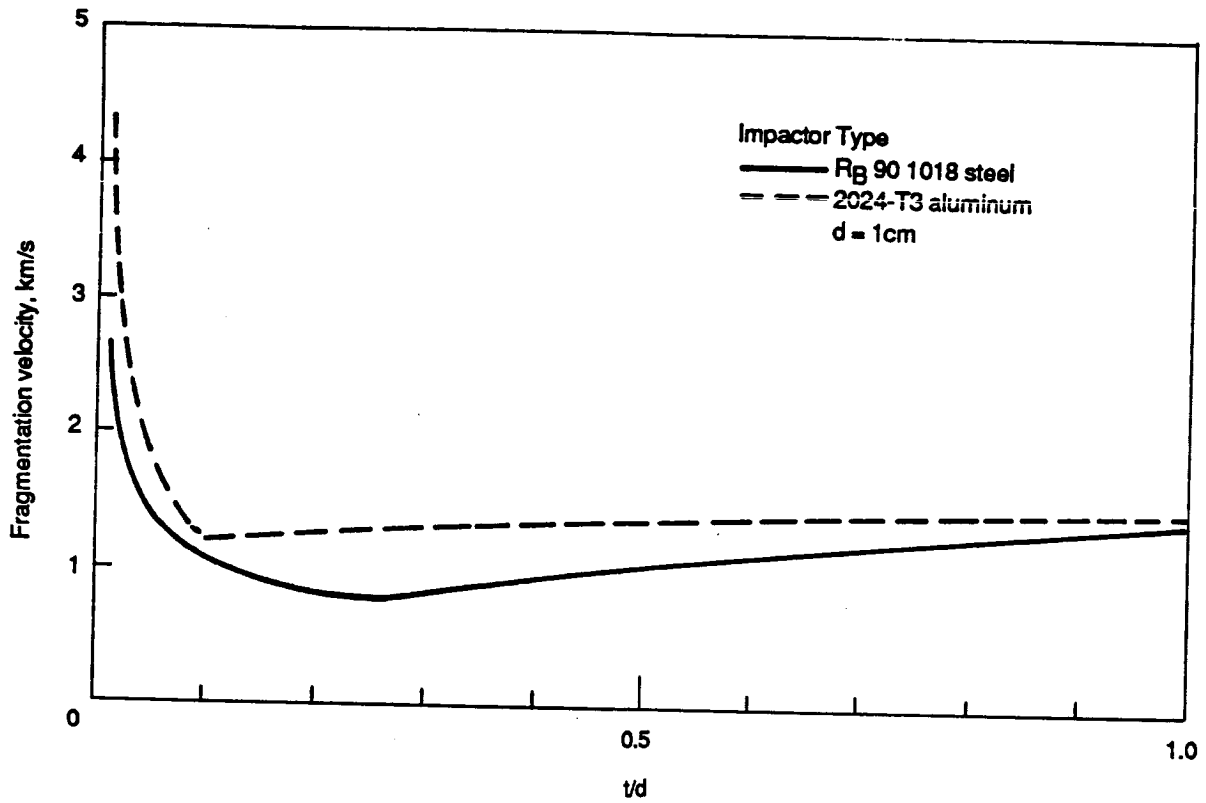


Figure 2-14. Fragmentation threshold relations for steel and aluminum projectiles striking aluminum plates.

2.3.4.2 Oblique Impacts. The dimensional analysis leading to Eqs. 32 and 34 can be modified to encompass oblique impact effects by including the angle of obliquity θ in the parameter list from which the dimensional analysis is performed. Since θ is dimensionless, and introduces no new fundamental dimensions into the problem, the only change to Eqs. 32 and 34 necessary is the addition of a new pi group, θ , in the functional dependencies f .

It has been argued in the Penetration Equations Handbook (Ref. 12), however, that concepts from the mechanics of fragmentation can be used to reduce the parameter list the threshold velocity for fragmentation is dependent on. Specifically, it was argued that the angle of obliquity does not enter the parameter list separately, but only in combination with the impact velocity. This argument is as follows: fragmentation from oblique impact between two flat surfaces is asserted to be governed solely by the longitudinal impact stress. For the P-wave shock amplitude in the projectile from oblique impact to equal the shock amplitude from normal impact at the fragmentation threshold velocity V_f , the impact velocity at oblique impacts V_p must equal,

$$V_p = V_f / \cos \theta. \quad (39)$$

This assertion ignores the effects from the shear wave generated at the interface between the projectile and the target, and it also ignores the effect of obliquity on the duration of the stress loading. However, it was decided that PEN4 should use a simple relation such as Eq. 39, since there were no relevant data to guide the selection of a functional dependence on angle of obliquity. Thus Eq. 39 has been used in PEN4 to describe the effects of angle of obliquity on the fragmentation threshold velocity.

Note that effects from projectile yaw have been ignored. It is assumed here that all impacts are between parallel plane surfaces, at all angles of obliquity.

2.3.5 Largest Residual Projectile Fragment Mass

As mentioned in the introduction to section 2.3.4, fragmentation has not been treated explicitly in previous DoD penetration codes. Up to this time, closing velocities between aerial targets and warhead fragments have been small enough to preclude warhead fragment fragmentation upon impact of the aerial target. Since fragmentation does not generally occur in an encounter, there has been no requirement to model fragmentation.

However, this is not to say that no data have been collected by the aerial target vulnerability community relevant to determining fragment size from impact. Some projectile fragmentation data were collected under Project THOR in the early 60's, and more recently the Navy has sponsored R&D efforts to quantify warhead fragment fragmentation for future weapons that will close at sufficient velocities to fragment the warhead fragment. These data

were reviewed at Boeing under contract with the Naval Surface Weapons Center, Dahlgren, Virginia. The results from these contracts, documented in Refs. 3 and 4, are the basis for the projectile fragmentation relations used in PEN4. Since these reports are not readily available, the major results are reproduced below.

Examination of several sets of largest residual fragment mass, m_r , data revealed that all have at least one of the three functional dependencies on impact velocity shown schematically in figure 2-15. These three functional dependencies on impact velocity are thought to stem from three distinct projectile fragmentation mechanisms described below.

At impact velocities just greater than V_f the projectile breaks up into a fixed number of fragments independent of velocity until another threshold is exceeded and the projectile breaks up into more pieces. If the projectile is brittle, then the number of pieces is fixed and independent of impact velocity above the second threshold. This produces the "stair-step" dependence of m_r on V labeled "spall" in figure 2-15. Spallation is described briefly in section 2.3.5.1.

The second mechanism labeled "power-law fragmentation" in figure 2-15 occurs when m_r is approximately proportional to the inverse square of impact velocity (i.e., kinetic energy). This behavior places constraints on a dimensional analysis of m_r , which allows specific predictions to be made concerning the dependence of m_r on impact velocity and material properties. This is discussed in greater detail in section 2.3.5.2.

The third and last fragmentation mechanism labeled "fragment size roll-off" in figure 2-15 occurs at the extreme limit of testing used for this update of PEN4 (3 to 4 km/s), thus too few data are available for drawing definitive conclusions on the nature of fragment size roll-off. The roll-off fragmentation mechanism, however, through its effect on m_r and the fragment size distribution (see section 2.3.6) is thought responsible for the decreasing ability of projectiles to perforate dual aluminum plate arrays with increasing impact velocity above 3 to 4 km/s. This is the most important feature of the "Whipple Meteoroid Bumper," and modeling this behavior with PEN4 is crucial to all future applications of PEN4 to hypervelocity impact. Thus an empirical relation for the functional dependence of m_r on V has been constructed for the roll-off fragmentation mechanism. The largest residual fragment mass roll-off fragmentation model is discussed at the section 2.3.5.3.

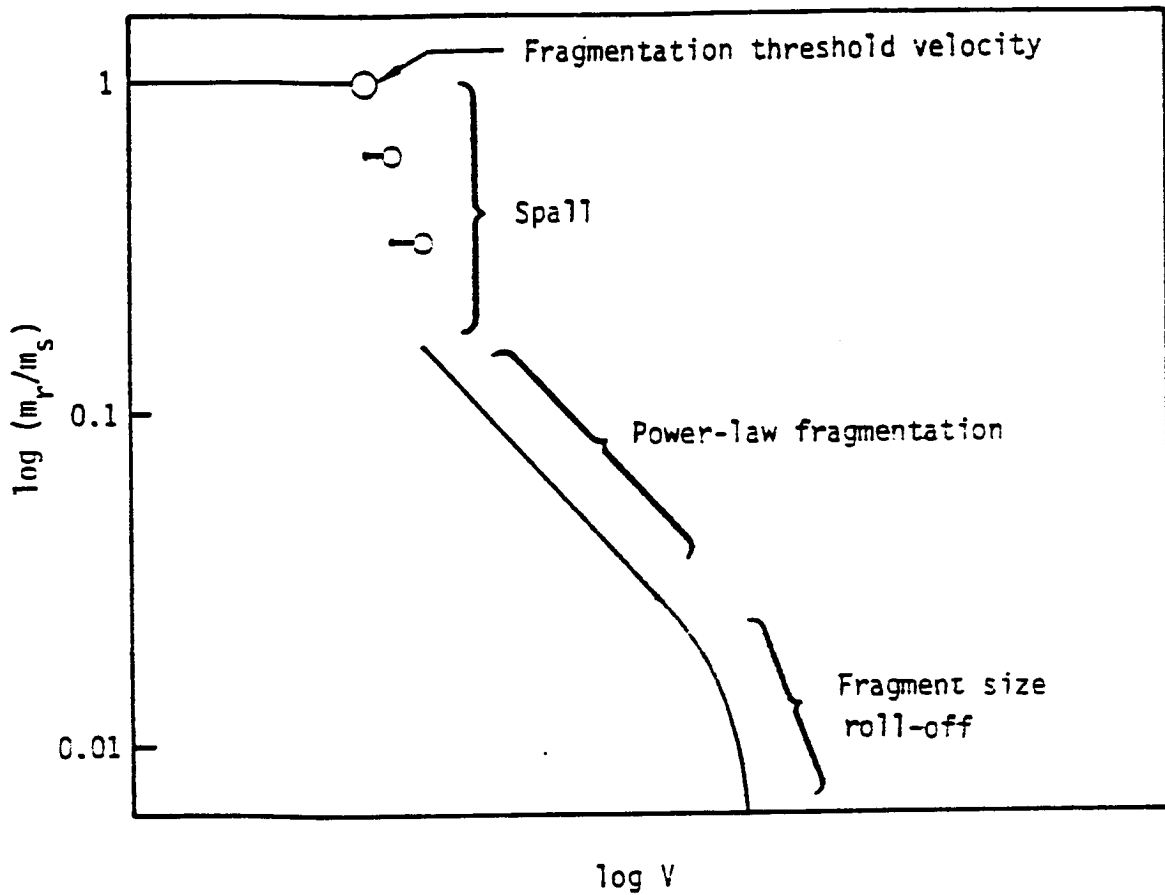


Figure 2-15 Schematic representation of the experimentally observed dependence of largest residual fragment mass on impact velocity.

2.3.5.1 Projectile Spall. Examination of test data has shown the spall mechanism for fragmentation is not important for the 2024-T3 aluminum cylinder and 1018 mild steel cube projectiles considered in this report, because the second mechanism shown in figure 2-15 rises to almost the fragmentation threshold for those two materials. Thus no spall fragmentation model for the projectile has been incorporated into PEN4.

2.3.5.2 Power-law Fragmentation. At impact velocities a few hundreds of meters per second above the threshold velocity for projectile fragmentation the largest residual fragment mass was observed to be proportional to the inverse square of impact velocity, as shown in figure 2-16. This strongly implies that projectile kinetic energy determines the largest residual fragment mass.

The observation that energy governs fragmentation is not new to this report and has been made several times before. Two examples are given here. The first example is the large body of test data collected by planetologists for the purpose of extrapolating experiments which can be performed in the laboratory to sizes typical of collisions between asteroids in the asteroid belt. (For a review of possible scaling laws see Holsapple and Housen, Ref. 27). Usually, the largest residual fragment data from these experiments have been scaled using the impact kinetic energy (Ref. 28). For example, the largest residual fragment mass data taken from Refs. 28 and 29 shown plotted in figure 2-17 scale with a power of the projectile initial kinetic energy. The mass of the largest piece of basalt target was found nearly proportional to the kinetic energy over three orders of magnitude of m_r . The exponent on kinetic energy in excess of one is indicative of rate-dependent fracture strength, as discussed in Ref. 27.

Even though the planetology data is for the impact of brittle rocks and not ductile metals, it is thought relevant to the present discussion for two reasons. First, dependence on the impact energy has been demonstrated for some three orders of magnitude in largest residual fragment size. This is taken as evidence for the effect being pronounced and persisting for a variety of sizes and impact velocities. Second, the planetology data was collected for impact velocities in the range 1 to 5 km/s, which is the same range of impact velocities the steel projectile striking aluminum plate data used below to develop the PEN4 relations were collected at.

D.E. Grady's work is the second example given here of a previous observation that energy governs the largest residual fragment mass. In Ref. 30 Grady made a convincing argument that energy governs fragmentation of rocks and metals for a variety of large strain rate loading conditions: flat plate impact, exploding cased munitions, and well shooting.

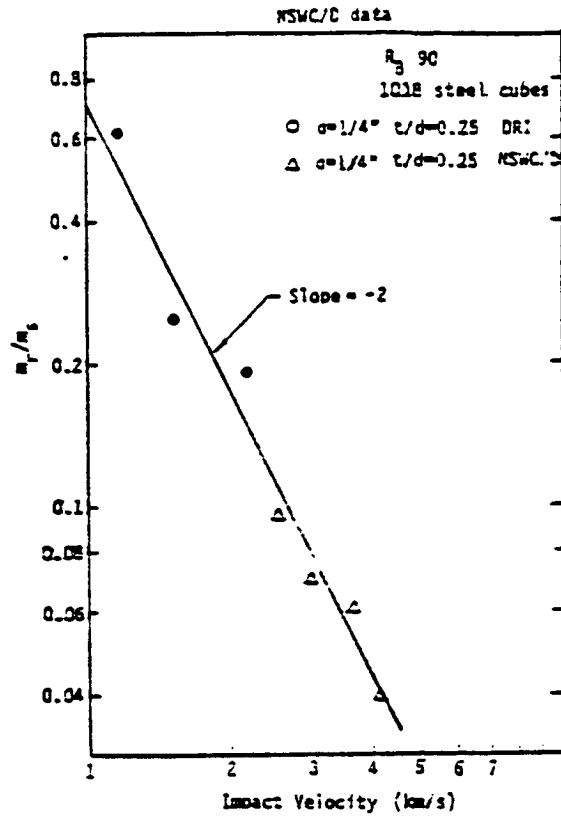


Figure 2-16 Experimentally measured dependence of largest residual fragment mass on impact velocity for mild steel cubes striking 2024-T3 aluminum plates.

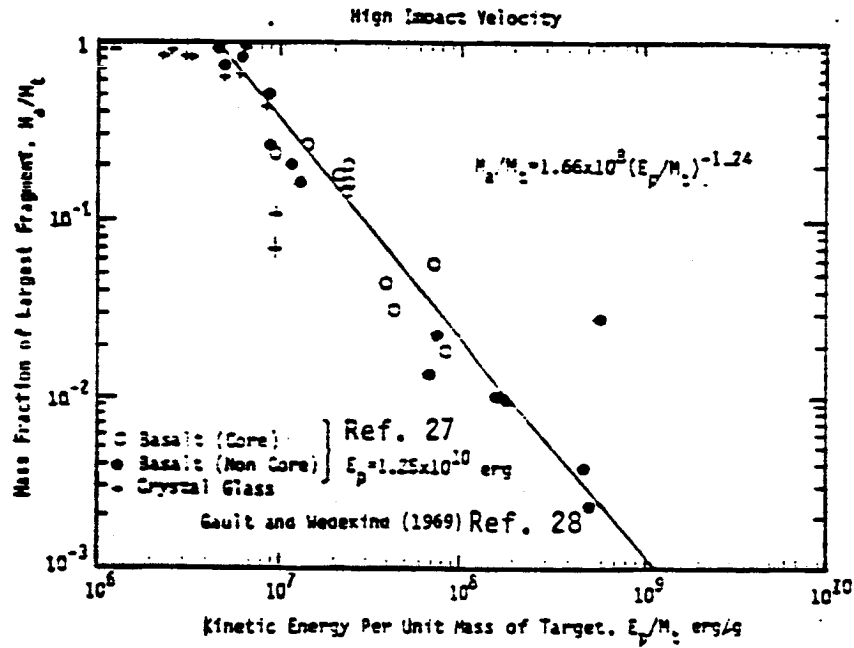


Figure 2-17 Measured dependency of largest residual fragment mass on impact velocity for lexan projectiles striking cubes of basalt.

Even more significant than Grady's observation of power-law dependence of largest residual fragment mass on energy was the demonstration of a power-law dependence on fragmentation material parameters at fixed energy. Figure 2-18 is a reproduction of a figure from Ref. 31 that shows that the average fragment size from an exploded cylindrical steel cased munition is a power-law of the fracture toughness of the steel case.

These two observations: dependence of fragment size on 1) a power of impact velocity and 2) a power of fracture toughness, indicate that only four significant parameters governing fragmentation exist at fixed t/d and at the range of impact velocities (approximately 1 to 5 km/s) the two observations were made. The above conclusion follows from the pi theorem because power-laws imply only one pi group, and, since there are three fundamental dimensions to fragmentation (mass, length, and time), there must be only four parameters so that only one pi group is obtained.

How this occurs can be illustrated by considering the simplest imaginable projectile fragmentation mechanism, one governed by a rate-independent fracture strength Y . The only other projectile and target material parameters of significance should be those that govern the impact stress amplitude and duration. For the most part, the impact stress should be governed by the ratio of projectile shock impedance, Z_p , to target shock impedance, Z_t . Therefore, for a projectile striking a thin plate the following variables are thought significant,

$$m_r = f(d, V, t, Y, Z_p/Z_t), \quad (40)$$

where t is the target plate thickness and is a measure of loading duration. Of the 6 variables in Eq. 40, 3 are fundamental dimensions, thus there are 3 independent dimensionless groups of variables, so Eq. 40 may be rewritten as,

$$m_r V^2 / (Y d^3) = f(t/d, Z_p/Z_t). \quad (41)$$

By multiplying the numerator and denominator of the left hand side of Eq. 41 with the projectile density δ and rearranging the pi group on the left hand side of Eq. 41 so that parameters are on both sides of the equals sign gives,

$$m_r/m = Y/(\delta V^2) f(t/d, Z_p/Z_t), \quad (42)$$

where m is the projectile striking mass and is proportional to δd^3 .

Equation 42 contains 2 results that can be tested by experiment:

1. m_r/m is proportional to V^{-2} at fixed d , t/d and material properties.

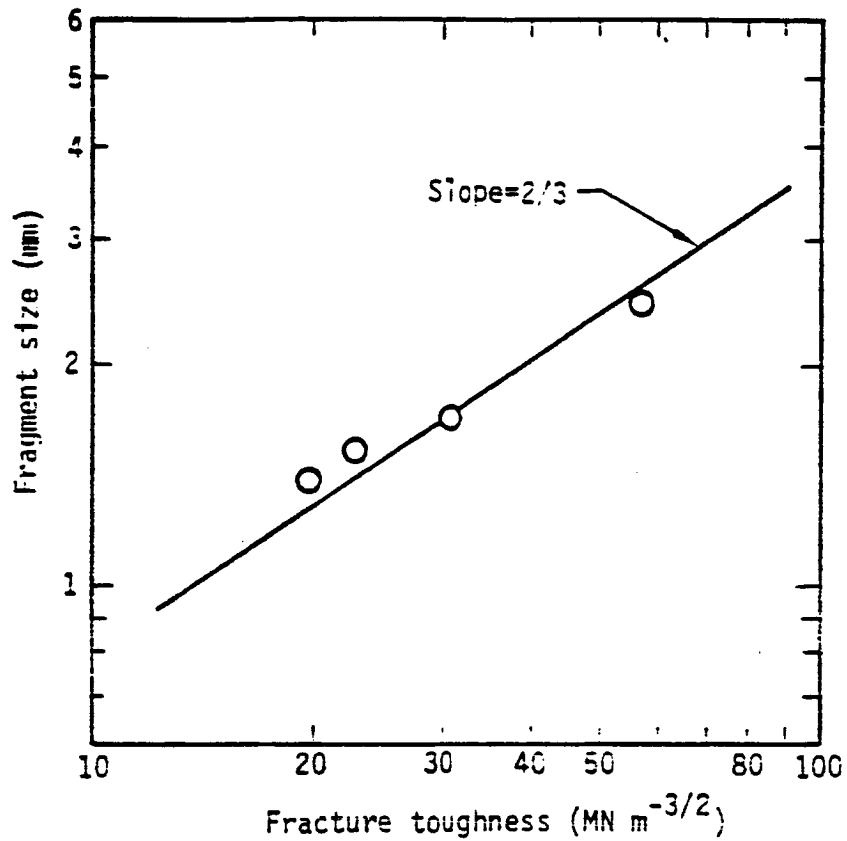


Figure 2-18 Measured dependence of average fragment size from an exploded case on the fracture toughness of the case.

2. m_r/m is proportional to Y at fixed V , δ , t/d , and ratio of projectile and target material properties.

The first result agrees well with the test data shown in figure 2-16. However, the lack of dependence on projectile size appears to disagree with the THOR 47 test data of Ref. 11. The fracture strength dependence given by result 2 has never been tested by experiment.

The above results can be generalized to rate-dependent fragmentation by generalizing the stress parameter Y to a rate-dependent material parameter S . The dimensions of parameter S are not known, so no particular assumption is made. To be completely general, it is assumed S has the dimensions of (stress)(length)^a (time)^b, where the exponents a and b are constants.

Thus the assumption is,

$$m_r = f(d, V, t, S, Z_p/Z_t). \quad (43)$$

Again, there are 3 independent dimensionless groups of variables,

$$m_r/m = S/\delta V^{-(2-b)} d^{-(a+b)} f(t/d, Z_p/Z_t). \quad (44)$$

Note that Eq. 44 is dimensionally consistent with the rate-independent case, Eq. 42. For a rate-independent strength S , the exponents a and b are zero. Substituting a and b equal to zero into Eq. 44 gives Eq. 42.

An argument is made in Appendix C that the appropriate material parameter to use in Eq. 44 is the fracture surface energy. This result was worked out in detail in Appendix C and fitted to some mild steel cube striking aluminum plate data. The results of this fit for $R_p 90$ 1018 steel cubes striking aluminum plates were,

$$m_r/m = [K_{1c}/(\delta c)]^2 V^{-2} d^{-1} f(t/d, Z_p/Z_t). \quad (45)$$

where,

$$\begin{aligned} f(t/d) &= 9.17 \times 10^3 & t/d < 0.1 \\ &= 5.42 \times 10^3 (t/d)^{-0.23} & 0.1 < t/d < 0.2 \\ &= 1.90 \times 10^3 (t/d)^{-0.88} & 0.2 < t/d < 0.4 \\ &= 1.17 \times 10^4 (t/d)^{1.1} & 0.4 < t/d < 0.8 \\ &= 9.09 \times 10^3 & 0.8 < t/d. \end{aligned} \quad (46)$$

To obtain the largest residual fragment mass for 2024-T3 aluminum projectile divide Eq. 46 by 7.78. (See Appendix C, section C.3, for the development of the mass distribution for aluminum fragments.)

2.3.5.3 Power-law Roll Off Fragmentation. Figure 2-15 illustrates the effect of the roll-off fragmentation mechanism on m_r . It is not known at this time what causes the rapid roll-off in largest residual fragment size for impact velocities above 4 km/s impact velocity for R_p 90 1018 steel projectiles striking aluminum plates and 3 km/s impact velocity for 2024-T3 aluminum projectiles striking aluminum plates. It is hypothesized that shock heating is decreasing the fracture strength of the material, resulting in very small fragments. This hypothesis appears reasonable because one can show through calculation that the projectile is shock heated to nearly half the melt temperature at impact velocities near 3 to 4 km/s. One possible method to test this contention is to recover the fragments and metallographically examine them for evidence of high temperature affecting their strength. Once the fragmentation mechanism for power-law roll off is identified, an analysis can be performed to determine the functional dependence of m_r on V analogous to what was done for the power-law fragmentation mechanism.

Lacking a physical basis for selecting functional dependencies of m_r on V, t/d, and d in the roll-off fragmentation region, an empirical approach has been taken. The mathematically simple approach of "folding" the power-law fragmentation relation, Eq. 44, across a boundary separating the power-law mechanism from the roll-off mechanism was settled on. Not enough data exist to map out the boundary's dependence on t/d and d, and the data for mapping out the V dependence are limited. For simplicity the boundary was assumed to be a power-law on V only.

There were a few more aluminum impacting aluminum data than steel impact aluminum data collected near the boundary separating power-law from power-law roll off fragmentation mechanism. Hence the aluminum striking aluminum data plotted in figure C-6 of Appendix C were used for mapping out the boundary's dependence on V. The boundary chosen is shown plotted in figure C-6 as a dashed line. This curve was then shifted by a constant factor to pass through the R_p 90 1018 steel cube impacting 2024-T3 aluminum plate data shown plotted in figure 2-19. The translated boundary for steel cubes is shown plotted in figure 2-19 as a dashed line.

The procedure used to develop the largest residual roll-off fragmentation mechanism fragment size for 2024-T3 aluminum cylinders striking 2024-T3 aluminum plates is outlined below.

The boundary between the power-law and the roll-off fragmentation mechanisms for 2024-T3 aluminum cylinders striking 2024-T3 aluminum plates was given the functional form,

$$(m_r/m)_c = (V_c/3.56 \text{ km/s})^{8.93}, \quad (47)$$

based on the dashed line boundary drawn freehand through the test data plotted in figure C-6. The variable $(m_r/m)_c$ is the y coordinate of the boundary and V_c is the x coordinate.

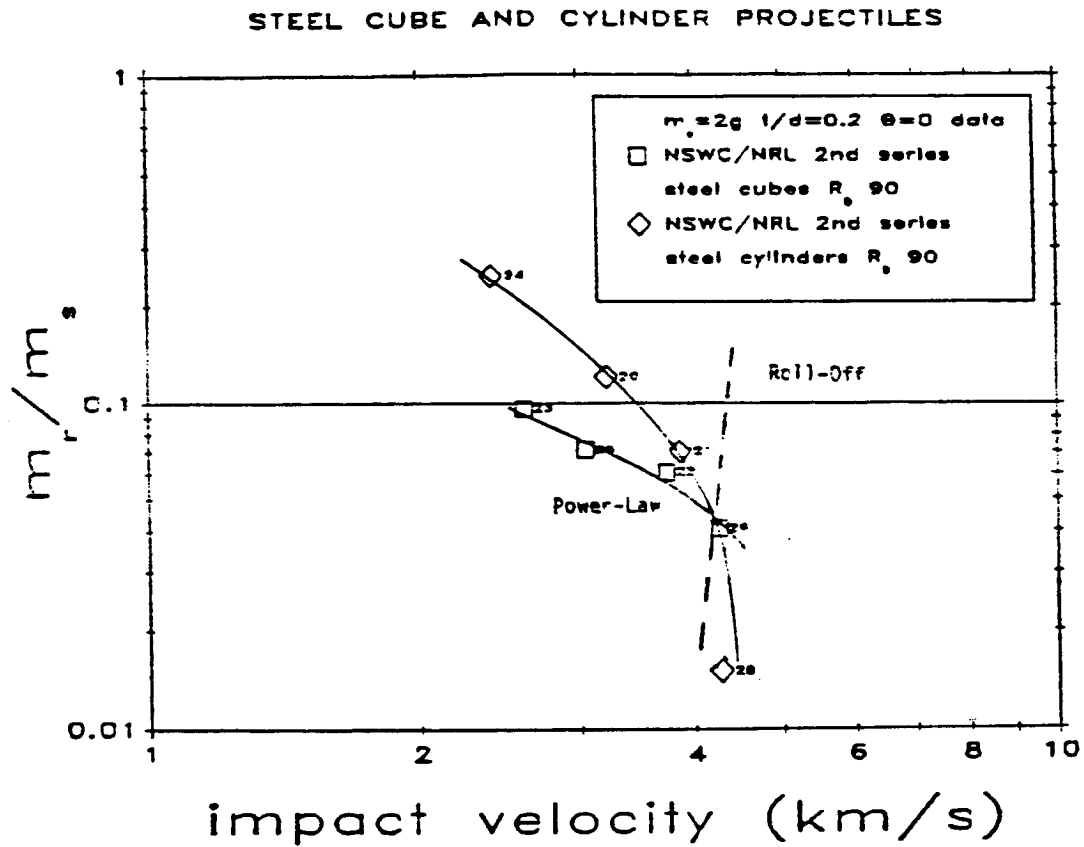


Figure 2-19 Boundary between power-law and roll-off fragmentation for R_B 90 1018 steel cubes striking 2024-T3 aluminum plates.

Equation 47 can be solved simultaneously with Eq. 45 to obtain V_c ,

$$V_c = (8.47 \times 10^4 \text{ (km/s)}^{8.93} [K_{1c}/(\delta c)]^2 d^{-1} f(t/d))^{0.0915} \quad (48)$$

The equation for the largest residual roll-off fragmentation mechanism fragment mass for 2024-T3 aluminum cylinders striking 2024-T3 aluminum plates can then be written in terms of the boundary as follows,

$$m_r/m = (m_r/m)_c (V/V_c)^{-6.2}, \quad (49)$$

where $(m_r/m)_c$ and V_c are evaluated using Eqs. 47 and 48, using the appropriate values for K_{1c} , d , and c . As mentioned above, the boundary for R_B 90 1018 steel cubes striking 2024-T3 aluminum plates was found by translating Eq. 47 to the position plotted as a dashed line in figure 2-19. The resulting equation for the boundary separating power-law fragmentation from roll-off fragmentation of R_B 90 1018 steel cubes striking 2024-T3 aluminum plates is,

$$(m_r/m)_c = (V_c/6.12 \text{ km/s})^{8.93}. \quad (50)$$

Analogous to what was done for aluminum striking aluminum, the largest residual roll-off fragmentation fragment mass is calculated by substituting Eqs. 50 and 48 into Eq. 49, using the appropriate material parameters, K_{1c} , d , and c , for R_B 90 1018 steel.

2.3.5.4 Oblique Impacts. Inclusion of impact obliquity angle, θ , into the dimensional analysis leading to Eq. 44 leads to an additional pi group, θ , in the functional dependence f in Eq. 44. However, this provides little guidance on how to include obliquity effects, since test data must be used to derive an empirical relation for the θ dependence.

Using the steel cube test data (which were used in Appendix C to develop Eq. 45 for normal impacts) to develop an empirical relation for the effect of θ on m_r immediately runs into trouble, though. The complicating factor stems from the known large effect of projectile yaw upon m_r . Therefore, even if the effort were expended to develop a relation from those data, the central question remains, "What is the relevance of steel cube oblique impact data to the problem of interest, the oblique impact of randomly shaped orbital debris fragments?"

Rather than spend considerable effort developing a precise equation for the wrong problem, it was decided to develop a relation for obliquity effects based on some simple expectations. Those expectations being: 1) the projectile fragments are thought to get smaller with increasing angle of obliquity and 2) the target plate fragments are thought to get larger with increasing angle of obliquity. Hence two functions are used,

$$m_r/m = ([K_{1c}/(\delta c)]^2 V^{-2} d^{-1} f(t/d, Z_p/Z_t)) \cos \theta, \quad (51)$$

and,

$$m_r/m = C [K_{1c}/(\delta c)]^2 (V \cos \theta)^{-2} d^{-1} f(\tau/d, Z_p/Z_t), \quad (52)$$

Both Eqs. 51 and 52 are calculated and the larger of the two is used to calculate the largest residual fragment mass.

Equation 51 is thought to approximately account for the decrease in projectile fragment size resulting from oblique impact. Two of the steel cube oblique impact data from Ref. 26 were examined and seemed to approximately follow the cosine dependence shown in Eq. 51. The decreasing fragment mass is thought to result from the increased amount of target material the projectile must pass through along the line-of-sight shotline at oblique impacts.

Equation 52 is thought to approximate the increase in target fragment size resulting from oblique impact. It is thought that the target plate fragments from the superposition of stress waves within the target plate, and thus the fragment size is governed by the P-wave amplitude, as was argued for the fragmentation threshold velocity in section 2.3.4.2. Since the P-wave amplitude is governed by the normal component of impact velocity, the normal component of impact velocity has been used in Eq. 52.

Note that, in general, the functional dependencies f in Eqs. 51 and 52 will not be equal; however, for the impact of aluminum orbital debris onto aluminum shield material, it is assumed that the target functional dependence is the same as the projectile and is given by Eq. 46 when divided by 7.78. Thus, for the impact of aluminum onto aluminum, the coefficient C in Eq. 52 is the ratio of the largest residual target fragment mass to the largest residual projectile fragment mass at zero obliquity angle. The coefficient C has not been measured for aluminum impacting aluminum, so $C = 1$ was chosen. This forces the largest residual target fragment to be larger than the largest residual projectile fragment for angles of obliquity larger than 0. This choice was made since it is known that the largest residual fragment comes from the projectile at zero angle of obliquity at impact velocities between 1 and 3 km/s, while it is thought that still larger fragments are needed to explain the NAS8-36426 oblique impact data discussed in section 4.2.

For steel impacting aluminum, C is set equal to zero. This is done because the steel fragments are assumed more lethal than the plate fragments, even when the plate fragments are somewhat larger.

2.3.6 Projectile Residual Mass Distribution

The projectile residual mass distribution developed here is a generalization and expansion on the work of others. Section 2.3.6.1 below lays down the necessary definitions and summarizes the major empirical results the PEN4 fragment mass distributions are based on. Section 2.3.6.2 is a dimensional analysis which ties together some fragment mass distribution concepts propounded by others. Section 2.3.6.3 lists the fragment mass distributions developed for use in PEN4.

2.3.6.1 Definitions and Important Empirical Results. The cumulative mass fraction of fragments with mass less than m_f , called $M(<m_f)$, is defined as,

$$M(<m_f) = \sum_{i=1}^{n_f} m_i/m, \quad (53)$$

where the subscript i on m_i indexes all fragments with mass less than m_f , n_f is the number of fragments with mass less than or equal to m_f , and m is the original projectile mass.

The cumulative mass fraction $M(<m_f)$ is often assumed to be described by a Weibull distribution (Ref. 31):

$$M(<m_f) = 1 - \exp[-(m_f/\langle m \rangle)^s e^a], \quad (54)$$

where $\langle m \rangle$ is the mean fragment mass and the exponents a and s are constants dependent on the material properties. Note that the only dependence on impact velocity and t/d in Eq. 54 occurs in the mean mass.

One consequence of using the Weibull distribution is that it approaches a power-law on fragment diameter for fragment masses less than the average fragment mass,

$$M(<m_f) = e^a (m_f/\langle m \rangle)^s, \quad (55)$$

in agreement with a large body of test data. Furthermore, Grady has reviewed these data and shown in Ref. 32 that the power on fragment mass (i.e. the power s in Eq. 55) is dependent on the fragmentation mechanism. Figure 2-20 is a summary of the power-law exponents s Grady found for four fragmentation mechanisms, along with an upper limit on s Grady derived from theoretical considerations (see Ref. 33).

The other major empirical result is related to Grady's observation that the exponent s of the distribution in fragment masses is related to the fragmentation mechanism. Since the exponent s is dependent on the fragmentation mechanism, any change in fragmentation mechanism is expected to result in a change in the fragment mass distribution exponent s .

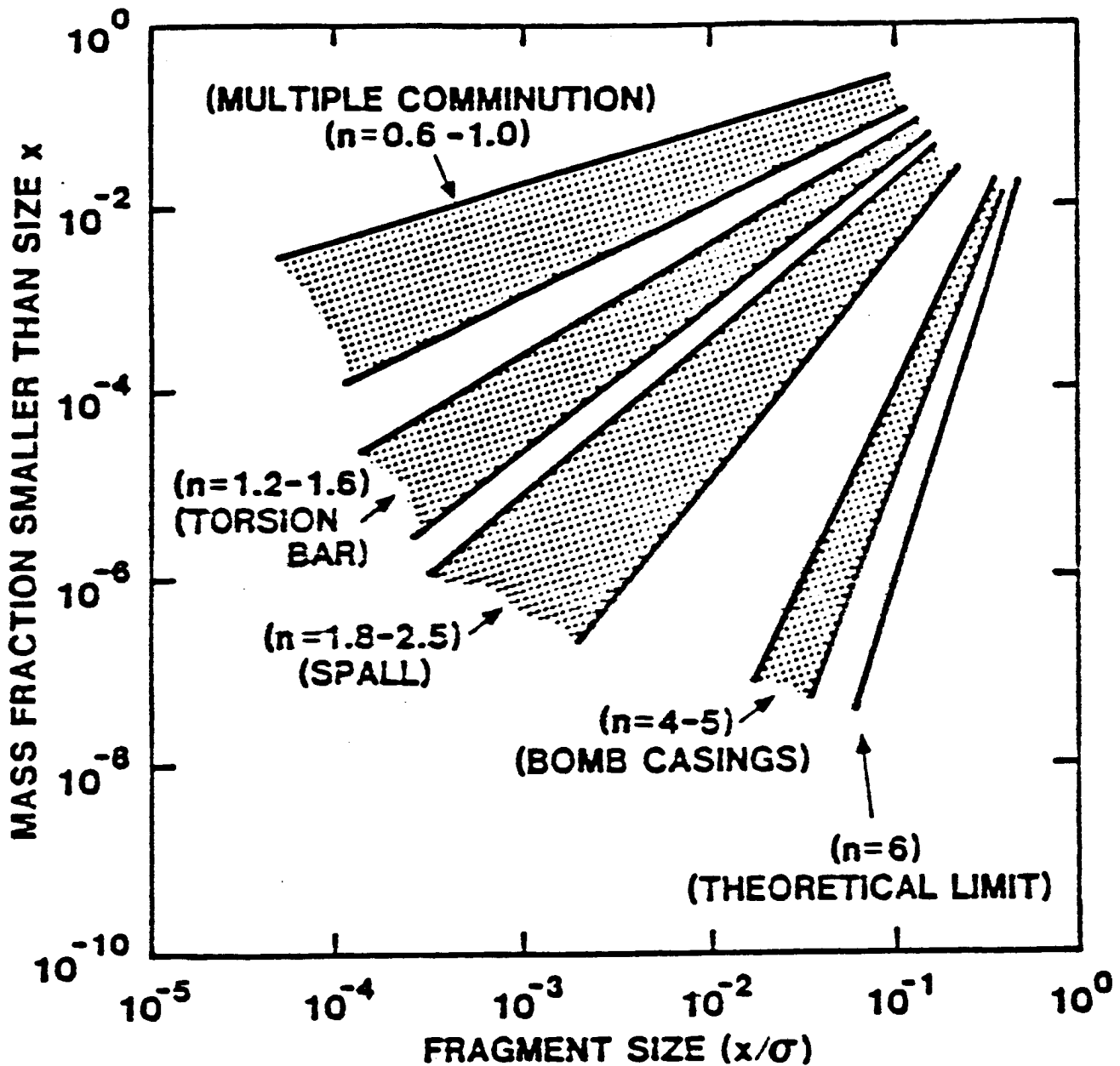


Figure 2-20 Cumulative fragment mass fraction distribution for four fragmentation mechanisms.

This postulated change in exponent of the fragment mass distribution was found in some recent NSWC/D tests (see Ref. 4). These data are plotted in figure 2-21. Note that the parts of the distributions to the right of the dashed line appear to have an exponent near two thirds, while the parts of the distribution to the left of the boundaries appear to have a smaller slope.

It is thought that the two slopes evidenced in figure 2-21 indicate that there are two fragmentation mechanisms occurring in the cubical projectile during the impact. Radiographs of the fragmented cubes as they exit the target plate indicate that the smallest fragments come from the corners. The cube corners will experience the largest radial velocities and hence large cumulative damage. It is hypothesized that the corners enter the roll-off fragmentation mechanism at smaller impact velocities than the cube center because of the large cumulative damage. Furthermore, it is thought that the large cumulative damage progresses towards the cube center as the impact velocity increases, until the entire cube is fragmenting by the roll-off fragmentation mechanism at impact velocities above 4 km/s.

2.3.6.2 Fragment Mass Distribution Dimensional Analysis. Even though the Weibull distribution was picked by empiricism, a dimensional analysis can be performed to show that it is a reasonable choice.

The cumulative mass fraction of projectile fragments produced by impact with plates is thought a function of the following variables,

$$M(<m_f) = f(d, V, t, S, Z_p/Z_t, m_f), \quad (56)$$

where d is the original projectile diameter, V is the impact velocity, t is the target plate thickness, S is the rate-dependent fracture material parameter with the units (stress)(length)^a(time)^b, Z_p/Z_t is the ratio of the projectile shock impedance to the target's, and m_f is the fragment's mass.

There are three fundamental units in Eq. 56 and 7 parameters, so there are 4 independent dimensionless groups of variables. One possible choice of π groups is,

$$M(<m_f) = f(m_f/m \delta V^{(2-b)} d^{(a+b)} / S, t/d, Z_p/Z_t), \quad (57)$$

where δ is the projectile density.

An important consistency check on Eq. 57 can be made by showing that it reduces to the equation for largest residual fragment mass, Eq. 44, developed in section 2.3.5. This is done as follows.

15:10:38 30-MAY-84

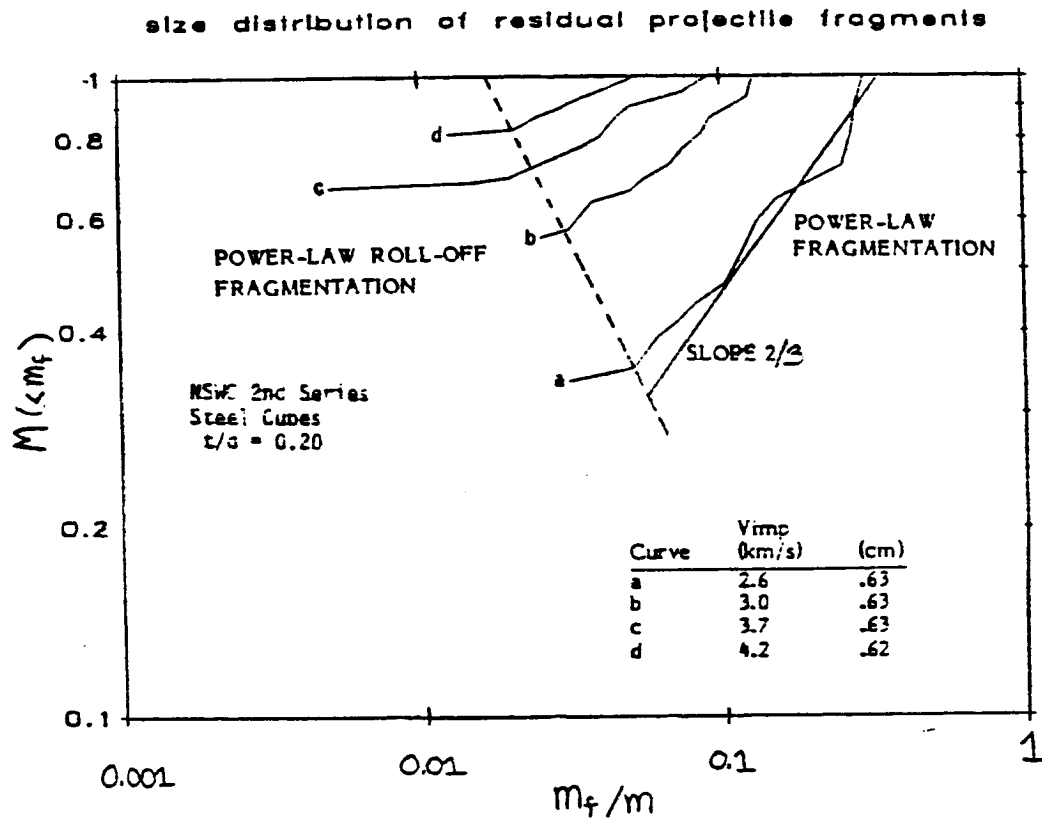


Figure 2-21 Cumulative fragment mass fraction distributions from steel cubes striking aluminum.

If $M(\langle m_f \rangle)$ equals one then all fragments are less massive than m_f , hence m_f is the largest residual fragment mass m_r . It is assumed that Eq. 57 can be solved explicitly for the first pi group on the right hand side of the equals sign to give,

$$m_r/m \propto V^{(2-b)} d^{(a+b)} / S = f(t/d, Z_p/Z_t). \quad (58)$$

Rearranging the pi group terms on the left hand side of Eq. 58 gives,

$$m_r/m = S / \delta V^{-(2-b)} d^{-(a+b)} f(t/d, Z_p/Z_t). \quad (59)$$

Note that Eq. 59 has the same form as Eq. 44 and thus is consistent as far as dimensional analysis can demonstrate. What is required to force complete consistency is to make the function f of Eq. 59 the same as the function f in Eq. 44, which was determined from fits to test data in Appendix C. This constrains the form of f in Eq. 59.

An even stronger result than Eq. 57 can be derived when the empirical result, that $M(\langle m_f \rangle)$ depends only on m_f and $\langle m \rangle$, is folded into the dimensional analysis. The above experimental result requires that all the V , t/d , S , d , and Z_p/Z_t dependence in Eq. 56 be incorporated into a single variable the mean fragment mass, $\langle m \rangle$. The above expressed in mathematical notation reduces Eq. 56 to,

$$M(\langle m_f \rangle) = f(m_f, \langle m \rangle). \quad (60)$$

There are three parameters in Eq. 60 and 1 fundamental dimension, hence Eq. 60 can be rewritten in terms of two independent dimensionless groups of variables,

$$M(\langle m_f \rangle) = f(m_f / \langle m \rangle), \quad (61)$$

which is consistent with the Weibull distribution, Eq. 54.

There are two consequences from assuming all the V , t/d , S , d , and Z_p/Z_t dependence is in the mean mass.

Consequence 1: The mean fragment mass $\langle m \rangle$ has the same functional dependence on V , t/d , S , d , and Z_p/Z_t as the largest residual fragment mass m_r . This consequence follows from a dimensional argument. Since $\langle m \rangle$ has the same parameter list as m_r in Eq. 43, dimensional analysis will lead to an equation analogous to Eq. 44. However, this consequence also results from a physical argument. If the fragmentation mechanism that governs the formation of the largest fragment also governs the formation of the mean mass fragment, then it is reasonable to expect the mean fragment mass to have the same functional form as m_r . (Note, we are not requiring the function $f(t/d, Z_p/Z_t)$ be the same for m_r and $\langle m \rangle$ since this is not fixed by the dimensional analysis.)

Consequence 2: Equation 61 requires a constant cumulative fragment mass fraction for all fragments with mass less than $\langle m \rangle$. This can be shown approximately true for the Weibull distribution as follows.

The mean value of m_f is calculated with the Weibull density function using the standard definition of expectation value given a continuous density function (in the present case the Weibull density function),

$$\langle m_f / \langle m \rangle \rangle = \int_0^\infty x e^{a/s} x^{s-1} \exp[-e^{a/s} x^s] dx, \quad (62)$$

where x is $m_f / \langle m \rangle$. Integrating Eq. 62 results in,

$$\langle m_f / \langle m \rangle \rangle = \exp(-a/s) \Gamma(1+1/s), \quad (63)$$

where $\Gamma(1+1/s)$ is the gamma function. Clearly the expectation value of $m_f / \langle m \rangle$ is one, so the right hand side of Eq. 63 must equal one. The gamma function varies in value from 1 to 0.89 for all values of the argument. Solving Eq. 63 for the exponent a given the exponent s and substituting the results into the Weibull distribution, Eq. 54, and solving for the cumulative mass fraction of all fragments with mass less than $\langle m \rangle$ gives the following table of values,

s	a	$M(< \langle m \rangle)$
1/3	0.0	0.63
2/3	-0.0777	0.60

for the most common values of the exponent s measured from fits to the fragment mass distribution data from Ref. 26. Note that the values for $M(< \langle m \rangle)$ vary by a factor smaller than the experimental scatter in the values, indicating an approximate agreement with the original contention.

In summary, we have been able to show in an approximate fashion that the Weibull distribution is consistent with the largest residual mass formula derived in section 2.3.5. Furthermore, we have argued that the mean mass occurs at an approximately constant value of cumulative mass fraction and that the mean fragment mass has at least the same functional dependence on V as the largest residual fragment mass.

2.3.6.3 Fits to Cumulative Fragment Mass Fraction Data. It is already known from the discussion of largest residual fragment mass given in section 2.3.5 that there are three fragmentation mechanisms governing fragment size.

According to figure 2-20, spall, which occurs at impact velocities around 1 km/s, is expected to result in a cumulative mass fraction distribution with

an exponent of approximately $2/3$ on the ratio of fragment mass to mean fragment mass.

The power-law fragmentation mechanism, which occurs at impact velocities between 1 and 4 km/s, is apparently associated with the portion of the cumulative mass fraction distribution to the right of the dashed boundary in figure 2-21. This is hypothesized on the basis of the distribution to the right of the dashed boundary governs m_r for impact velocities between 1 to 4 km/s. The values of exponent s in this region are between $1/3$ and $2/3$.

At impact velocities larger than 4 km/s, it was shown in Ref. 24 that the exponent s on Eq. 54 is approximately $1/3$.

Since the test data of figure 2-21 evidence two distinct distributions, it was decided the data would best be fitted with two distributions: one using exponents typical of power-law fragmentation and the other exponents typical of roll-off fragmentation.

The power-law and roll-off fragmentation modes have been least squares fitted using two separate Weibull distribution functions.

The values of exponents a and s determined from the least squares fit for the power-law fragmentation mechanism are:

$$a = -1.17 + .313 (t/d)/\cos(\theta) + .0675m + .508V \quad (64)$$

$$s = 1.38 - .510 (t/d)/\cos(\theta) + .036 m - (1-\exp(-.39V)), \quad (65)$$

where projectile mass m is in units of grams, and impact velocity V is in units of km/s. The variable θ is the impactor obliquity angle.

The values for a and s determined from the least squares fit to the roll-off fragmentation mechanism are:

$$a = -2.3 - 1.1(t/d)/\cos(\theta) + .0675m - .27V \quad (66)$$

$$s = 1.8 - .04(t/d)/\cos(\theta) - .0420m - (1-\exp(-.64V)), \quad (67)$$

and again m is in units of mass and V is in units of km/s. For a given fraction of the mass, the distribution yielding the smallest fragments is used.

Note that because the selection of a linear dependence on t/d and m Eqs. 66 and 67 cannot be used for values of t/d and m , much outside those of the data to which they were fitted. In fact, values of t/d larger than 2 and mass larger than 30 grams will probably lead to negative exponents and hence problems with calculating negative values of cumulative mass fraction.

The function used to describe the mean mass is,

$$\langle m \rangle = 0.0109 - 0.00879 t/(d \cos \theta) + 0.000506 m - 0.00428 V. \quad (68)$$

If the input values of t/d , m and V are such that Eq. 68 results in a value less than 5 milligrams, then $\langle m \rangle$ is set equal to 5 milligrams. To approximately factor in the effect of the roll-off fragmentation mechanism on $\langle m \rangle$, above 3 km/s Eq. 68 is multiplied by,

$$\langle m \rangle = \langle m \rangle_{\text{Eq. 68}} [V/(3 \text{ km/s})]^{-6.2}. \quad (69)$$

To show the degree of goodness of fit, Eqs. 64 through 69 have been used to calculate the cumulative fragment mass fraction distribution for the data plotted in figure 2-21. The results of the calculation are plotted in figure 2-22 along with the test data from figure 2-21.

The fit is less than satisfactory for several reasons. The first reason is it does not fit the large impact velocity data in figure 2-22 well. Part of the reason for the poor fit is that Eqs. 64 through 68 are least squares fits to smaller impact velocity test data (mostly 1 to 2.5 km/s) extrapolated out of the region of V , t/d , and m they were fitted to. The second reason for the poor fit is that no effort was made to assure that the fits were consistent with the dimensional arguments made in section 2.3.6.2, hence the least squares fitting was made to the wrong functional forms. In the cases of Eqs. 64 to 68 the choice of a multilinear regression on V , t/d , and m guarantees that the exponents a and s will go negative for some choice of V , t/d , and m leading to nonsensical results. A further drawback to least squares fitting to the wrong functional dependencies is that it sometimes gives nonphysical results, as in the case of Eq. 64. The coefficient on the V dependence is positive, leading to fragment mass increasing with impact velocity in the power-law region of fragmentation, contrary to experiment.

At sometime the data must be refitted using the correct functional dependencies. The effect on the present calculations is unknown and will require a parameter study with the correct fits to the cumulative mass fraction data to determine the magnitude of the problem.

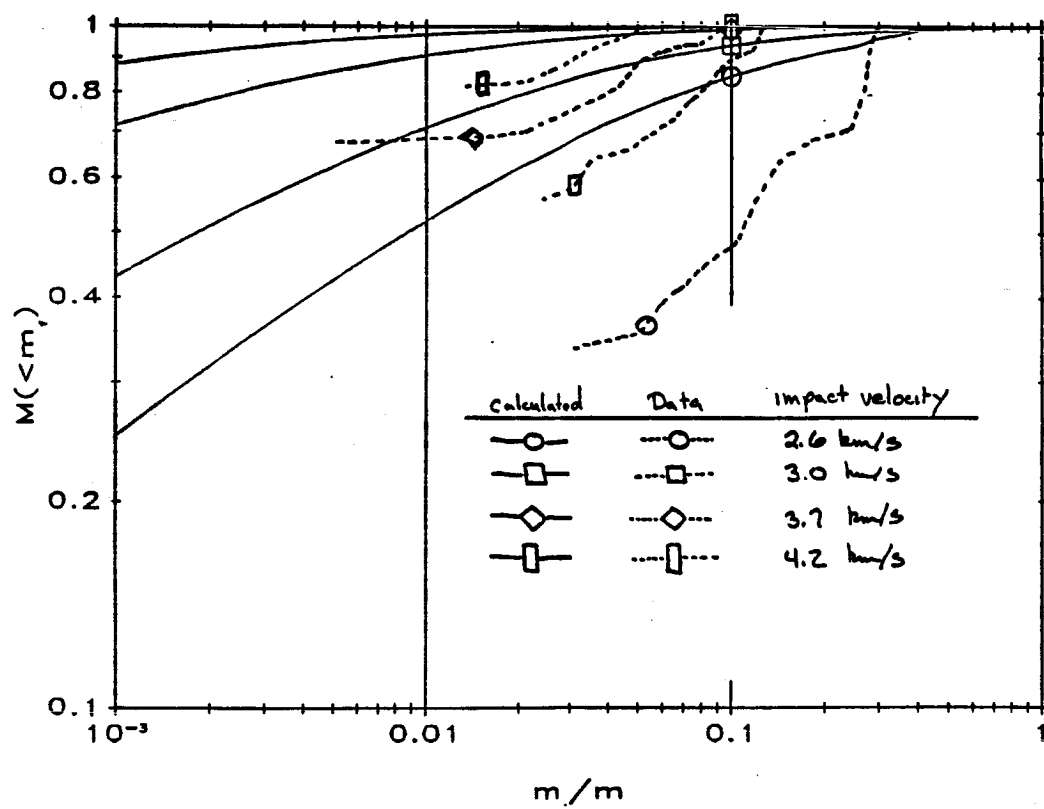


Figure 2-22 Comparison of PEN4 cumulative mass distribution with test data.

2.3.6.4 Oblique Impacts. Test data from shots at oblique angles of impact were also least squares fitted, and the resulting fit to the functional dependence on θ shown in Eqs. 64 to 68 is used in PEN4. It is not clear whether this is the correct functional dependence to use. Further analysis is required to validate the choice.

2.3.6.5 Fragment Mass Bins. The continuous cumulative mass fraction distribution described in section 2.3.6.3 must be divided into a discrete distribution composed of several bins before it can be used in PEN4.

The procedure for dividing the continuous distribution into a discrete distribution is illustrated in figure 2-23: For the purpose of illustration the continuous mass fraction distribution labeled "A" in figure 2-23 has been divided into three mass bins. (The effect of varying the number of mass bins on the results will be discussed below.) The largest residual mass is put into a bin of its own, comprising Section I in figure 2-23. The rest of the continuous distribution will be approximated by the intermediate mass fragments in bin II, and the smallest mass fragments in bin III.

To determine the number of fragments in a bin a characteristic mass of fragments in the bin must be chosen. This is done by computing the mean of upper and lower bounds of the cumulative mass fraction in each bin, points a and b in figure 2-23, and using the continuous cumulative mass fraction distribution A to project the mean onto the fragment mass axis (i.e., the intersection of the horizontal dashed lines in figure 2-23 with the continuous distribution curve "A"). The characteristic masses are labeled as m_2 and m_3 in figure 2-23 for bins II and III, respectively. Each bin is then considered to only contain fragments with that characteristic mass.

It is important that the choice of upper and lower limits of cumulative mass fraction in each bin (and the resulting characteristic mass of that bin) be representative of all significant populations of fragments, because penetration behavior is very dependent on the number and masses of the fragments.

This can be illustrated two ways. First, the characteristic mass of a bin affects the multiple cratering behavior of that bin because: 1) the hole area for a single impact is a direct function of fragment size, and 2) the number of fragments in the bin is the mass of the bin divided by the mass of its characteristic mass. (Both of these values decide the mean and standard deviation of the probability of multiple impacts.) Second, the crater depth is also a function of fragment size, so the number of coincident impacts required to create a perforation and the likelihood of experiencing them is very dependent upon the assumed characteristic mass.

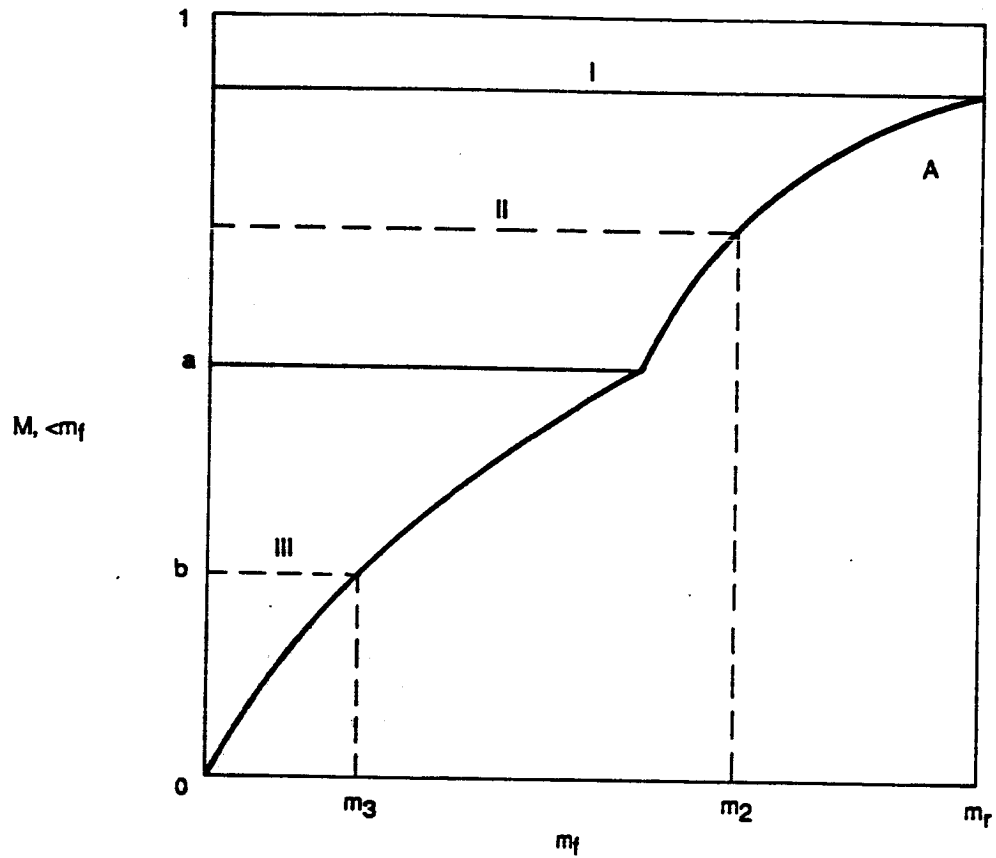


Figure 2-23 Determination of characteristic bin fragment mass using the cumulative mass fraction distribution.

Two procedures have been used to select the upper and lower bounds on the mass fraction in each bin. The first method divided the mass fraction less than that of the largest residual fragment mass evenly into the number of remaining bins. This procedure is illustrated in figure 2-24. Thus if five bins were used in a PEN4 calculation, then the first bin would contain the mass of the largest fragment and bins 2-5 would each contain 25% of the remaining projectile mass.

This procedure was found to adequately represent the larger and average sized fragments but not the smallest fragments. As a consequence, PEN4 output as a function of impact velocity contained large jumps resulting when the larger fragments changed size. Without large numbers of smaller fragments these jumps were not smoothed. This effect is illustrated in the plot shown in figure 2-25 of minimum projectile diameter required for perforating a two plate array as a function of impact velocity (hereafter referred to as a critical diameter plot). The peaks labeled A, B, and C could be reduced by increasing the number of bins, however, the PEN4 executed very slowly when the number of bins got above 10. A critical diameter plot over the same range of diameters and impact velocities up to 10 km/s calculated with 15 bins took one half hour CPU time on a VAX 11/750.

The current method used in PEN4 to allocate the upper and lower bounds on the cumulative mass fraction of the bins for the most part eliminates the peaks so evident with the previously described method. The current method assigns to bin 5 all the mass between a cumulative mass fraction of 0.0 and 0.01 (Where cumulative mass fraction is normalized projectile mass minus the largest residual fragment mass). This procedure recognizes the existence of smaller fragments that were ignored by the previous apportionment of mass between the bins. The upper limits on mass fraction of the remaining bins are set at 0.5, 0.8 and 1 of the mass fraction, for bins 4, 3, and 2, respectively (Again normalized by the projectile mass minus the largest residual fragment mass). As before, bin 1 contains the largest residual fragment mass.

The critical diameter curve plotted in figure 2-24 was recalculated using the above apportionment of fragment mass. The resulting critical diameter curve is plotted in figure 2-25. Comparing figures 2-24 and 2-25 illustrates the smoothing effect of the smaller particles. Their smaller steps in cumulative crater depth give a finer resolution to the threshold for two plate perforation since there are more different combinations of fragments that are likely to occur.

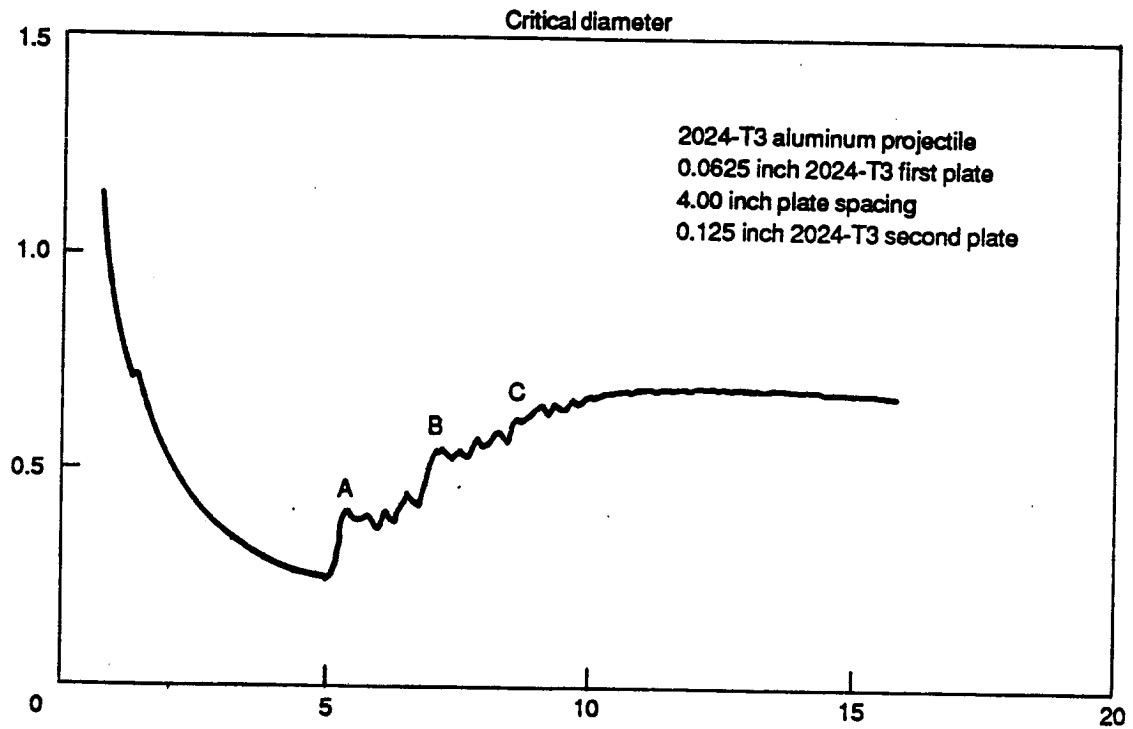


Figure 2-24 Critical diameter curve calculated with equal amounts of mass allocated to each bin. Not used in PEN4 version 10.

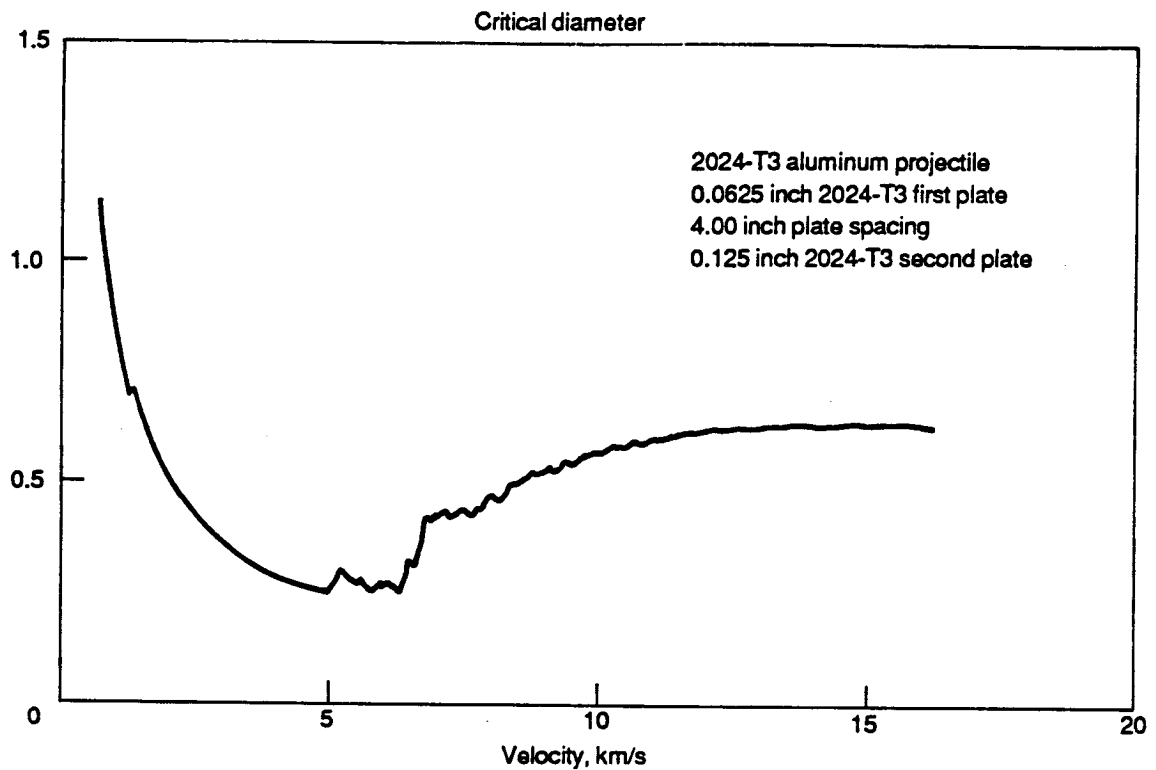


Figure 2-25 Critical diameter curve calculated with unequal amounts of mass allocated to each bin. Method used in PEN4 version 9.

2.3.7 Projectile Fragment Number

Projectile fragment number is calculated from:

$$N_R = (m/m_f) F_A F_M, \quad (70)$$

where N_R is the number of fragments in the size bin of interest, m is the original projectile mass, m_f is the fragment mass, F_A is the function describing the fraction of original projectile mass transmitted through the first plate when the projectile strikes obliquely (i.e., the fraction of the projectile not ricocheted off the target plate), and F_M is the amount of mass in the size bin of interest.

The function F_A used in PEN4 for calculating the projectile mass fraction transmitted through the target plates for oblique impacts is shown plotted in figure 2-26. The points plotted in figure 2-26 are 2-d hydrocode calculations of infinitely long round steel bar stock striking aluminum plate. The function drawn through the points is,

$$F_A = -2.423 \times 10^{-4} - 1.643 \times 10^{-2} \cos \theta + 3.201 \cos^2 \theta - 2.184 \cos^3 \theta, \quad (71)$$

where θ is the impact projectile obliquity angle relative to the normal of the impacted plate.

Equation 71 was calculated for only one t/d ($t/d = 0.6$) and one impact velocity ($V = 5.2$ km/s). Therefore, Eq. 71 is best applied to $V = 5.2$ km/s and $t/d = 0.6$, and its applicability to other t/d 's and impact velocities is uncertain.

2.3.8 Plate Fragment Mass Distribution and Number

PEN4 does not currently model the cumulative mass fraction distribution of plate fragments separately from projectile fragments. The total mass of material holed out of the shield is determined from the hole diameter calculation described in section 2.3.2. This mass is then added to the projectile mass, and the projectile size distribution and plate fragment aggregate is determined from the relations given in section 2.3.6. The number of fragments from the projectile and plate fragment aggregate is determined by the relations given in section 2.3.7.

This procedure is thought to be reasonable for two cases. The first case occurs when the projectile density is significantly larger than the target material, hence the most penetrating damage to the second plate will come from the projectile fragments and the plate fragments may be safely ignored. The second case for which modeling the details of the shield plate fragment mass distribution is not thought significant arises when the projectile mass is significantly larger than the holed out shield mass.

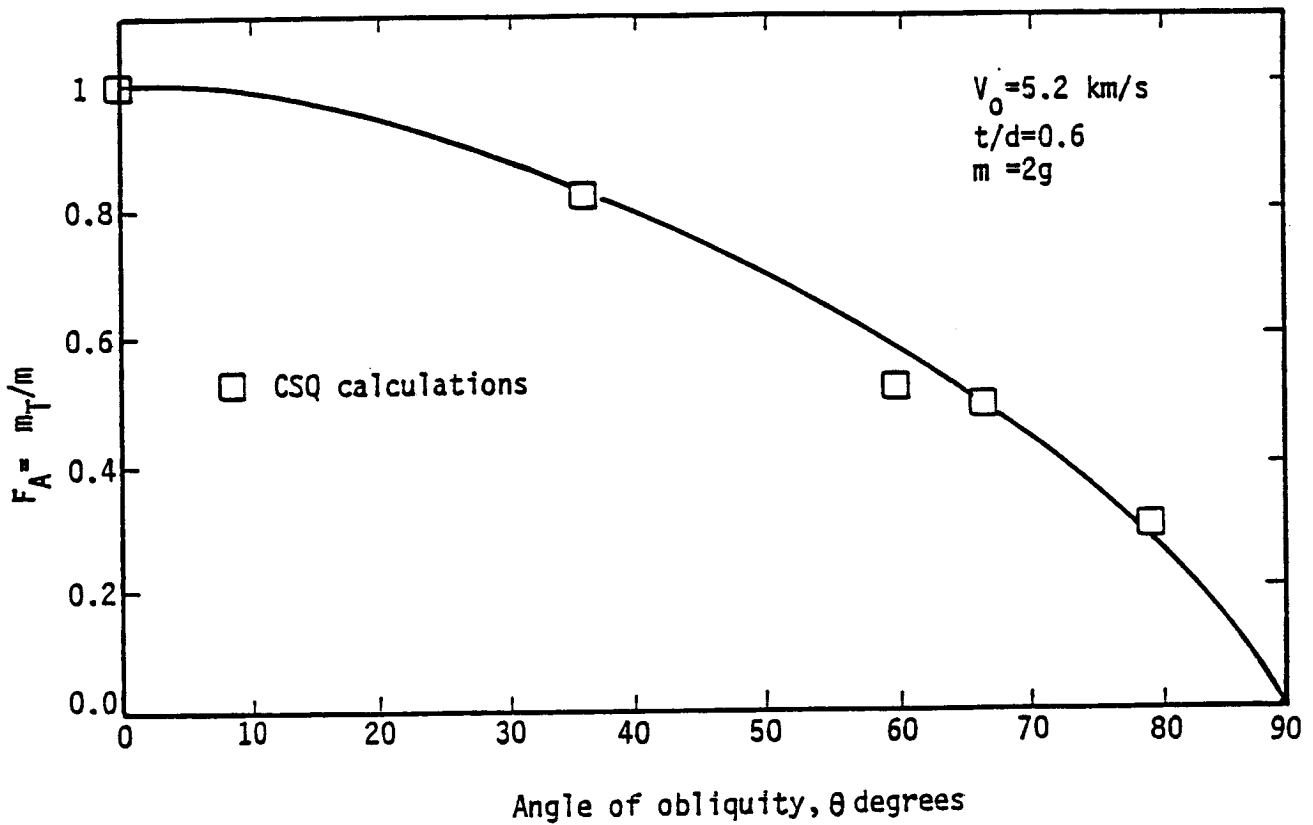


Figure 2-26 Transmitted cumulative mass fraction as a function of angle of impact obliquity.

PEN4 was originally developed to model the penetration of tantalum and steel warhead fragments into arrays of aluminum plates, both satisfying the first case, and hence considered satisfactory. However, modeling the penetration of aluminum orbital debris into arrays of aluminum plates does not satisfy the first case. Furthermore, the orbital debris problem also does not satisfy the second case, as illustrated by the following.

The two plate configuration tested most often at NASA/MSFC consisted of a 63-mil thick first plate separated 4 inches from a 125-mil second plate. The ratio of the PEN4 calculated critical aluminum projectile diameter to perforate this array to the PEN4 calculated holed out area on the shield plate (the 63-mil plate) is shown in figure 2-27. Note that the projectile mass is larger than the mass removed from the shield plate only for impact velocities less than some 2 km/s. Hence, neglecting the details of the shield plate fragment mass distribution, as is done in PEN4, is best done for impact velocities smaller than 2 km/s or for projectile masses above the critical diameter curve. If the mass removed from the shield is to be kept to 10% of the projectile mass, then the minimum projectile diameter PEN4 should be applied to for this plate configuration is 1.8 cm.

The details of the shield plate fragment distribution are not thought significant for impacts at normal obliquity. This assertion follows from the successful modeling of the critical diameter curve for normal impacts. However, as discussed below in section 4.2, PEN4 is not successful at modeling the critical diameter curve for oblique impacts. Examination of NAS8-36426 series 206 and 208 oblique impact test data revealed several much larger than expected craters in second plate. Closer examination of the shield showed the entrance hole was dished in and had a ragged edge caused by 2 or 3 large pieces being torn from the hole periphery. The dishing in the plate around the hole indicates that some low speed deformations of the hole were occurring at times late in the formation of the hole. These motions could have resulted from or caused the large pieces to be torn from the hole edge. It is thought that these large pieces are responsible for the perforating damage to the second plate.

In summary, PEN4 as it is constituted now adequately reproduces the critical diameter curve for normal impacts; however, if increased fidelity to the aluminum projectile oblique impact test data is required, then more testing is needed to quantify the size and velocity distribution of the fragments produced by the impact with the shield plate.

2.4 SECOND PLATE PENETRATION

The fragments generated in the first plate impact were assumed to

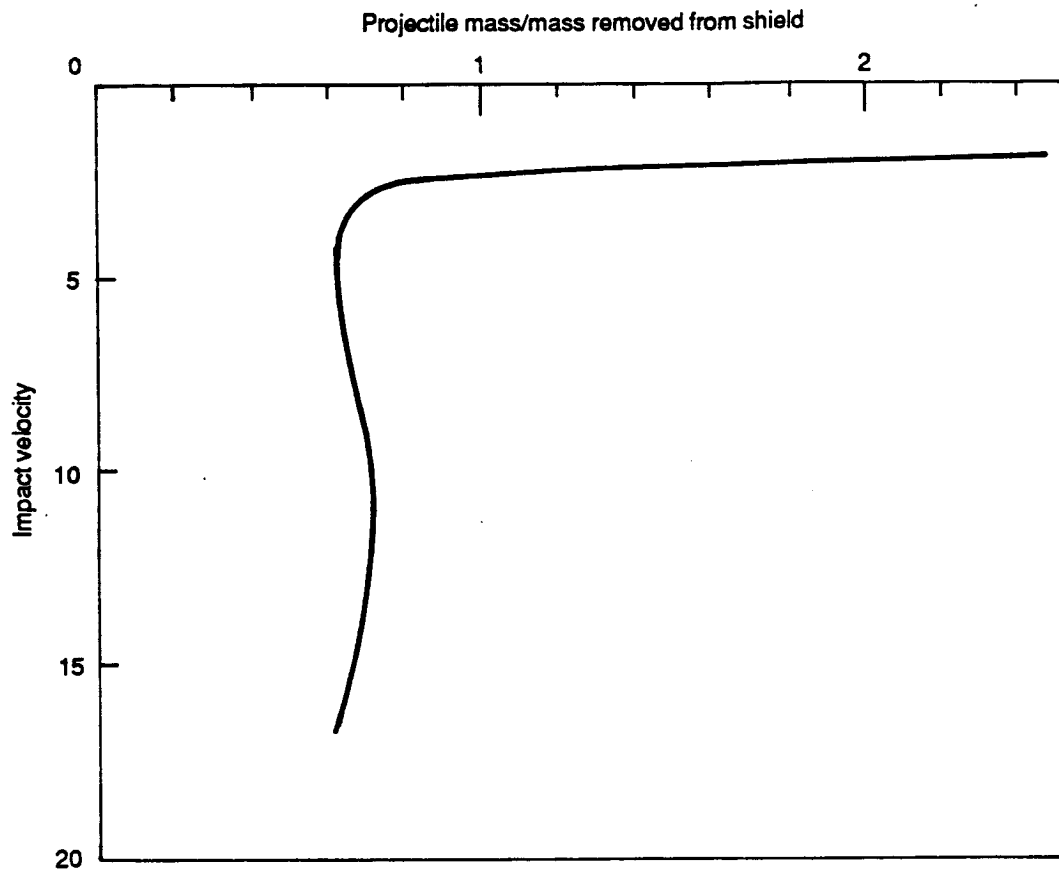


Figure 2-27 Ratio of first plate mass loss to projectile mass along the critical diameter curve for a 125-mil plate shielded by a 63-mil plate separated by 4 inches.

form a conical pattern with the half angle of the cone determined from test data. The intersection of the spray cone with the second plate produces the fragment spray area, A_s , on the second plate. This spray area therefore is impacted by the total number of fragments, N_t . Each individual fragment produces a crater having effective area A_c . The multiple impact model assumes second plate penetration results from craters being formed inside other craters that exist from earlier fragment impacts. The number of impacts required for penetration is determined by adding multiple impact crater depths until their total depth equals the second plate thickness.

If the crater from a single impact has a radius R_c , then only those additional fragments that strike inside $R_c/2$ are considered as forming additive craters. Thus, the effective crater area, A_c , is only one-fourth of the single crater area. The number of impacts that contribute to the multiple crater is determined statistically using A_c . The appropriate statistics depend upon the number of impacts that contribute to the multiple crater.

2.4.1 Spatial Distribution of Fragments on Second Plate

The calculation of the spatial distribution of fragments is broken down into two steps in PEN4. First, the area on the second plate covered by projectile fragment impacts is calculated using a formula for the spray area. Second, the fragments are distributed across the spray area. This step is built into the calculation of probability of multiple impacts in version 10 of PEN4.

The area on the second plate enclosing the impacts by projectile fragments is circumscribed by the half-angle, ϵ , which was derived from fits to spray area test data. The experimentally measured spray area diameter on the second plate and diameter of the area on the second plate covered by overlapping craters are recorded for some shots of Ref. 17. An ad hoc assumption was made equating the spray area of the projectile debris with the spray area of the overlapping craters.

The equation for spray angle used in PEN4 is,

$$\epsilon = \epsilon_{\max} \{1 - \exp[-(V - V_f)/V_c]\} \quad (72)$$

$$\epsilon_{\max} = 52 \text{ degrees} \quad (73)$$

$$V_c = 1.5 \text{ km/s } (t/d)^{2.3}, \quad (74)$$

which is a fit to spray angle data taken from Ref. 17. The test data and Eq. 72 are plotted together in figure 2-28.

The spatial distribution in Version 10 of PEN4 is implicit in the calculation of probability of multiple impacts. Since a binomial

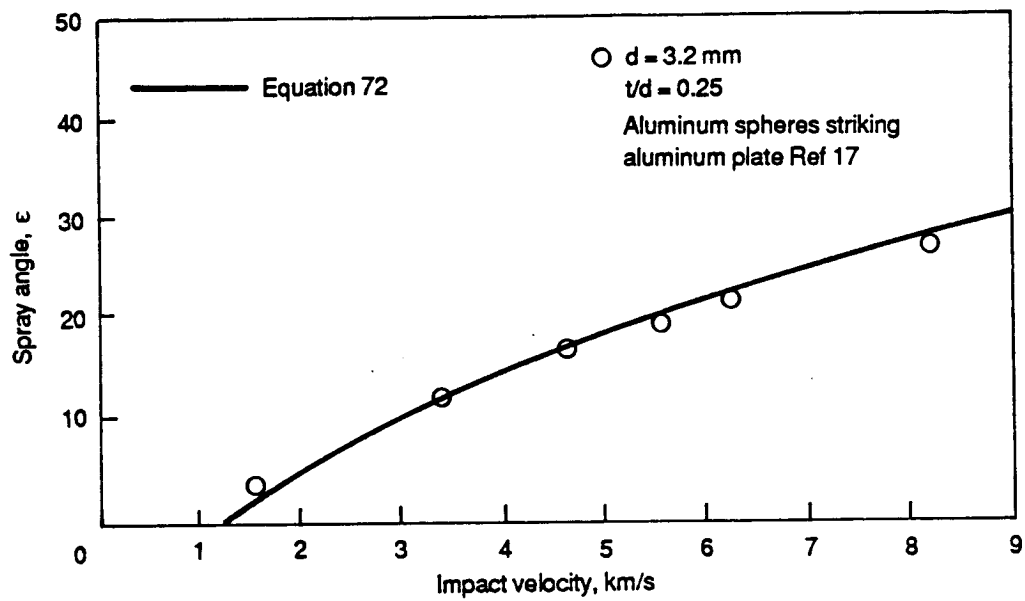


Figure 2-28 Dependence of projectile spray angle on impact velocity.

distribution is used to calculate the probability of multiple impacts, there is an implicit assumption that there is an equal probability of fragments impacting any area within the spray area.

For situations where the plate spacing is sufficiently large to spread the fragments so that there is not much multiple cratering, the implicit spatial distribution of equal probability of impacting any is most likely adequate. However, for some situations the shield/projectile debris cloud has been observed to have more fragments along the shotline than at the spray area periphery. To test the effect of concentrating the fragments along the shotline, another spatial distribution (in combination with a new assumption on the probability of multiple impacts) was tried. This study is documented in Appendix D, where it is concluded that the present equal probability of impacting any spot within the spray area spatial distribution is adequate for the space station applications.

2.4.2 Crater Depth and Radius

As was the case in section 2.3.2 on hole diameter, the scaling of crater depth is simpler at large impact velocities than it is at small impact velocities. Thus, there are two types of PEN4 crater depth relations: the first type is one equation, applicable to large impact velocities, is quite reliable and applicable to any homogeneous isotropic rate-independent metal; the second type is only applicable at smaller impact velocities, is less reliable, and is applicable to only one projectile/target material combination. Hence there is one equation for steel striking aluminum at small impact velocities and another for aluminum striking aluminum. The equations used in PEN4 to calculate crater depth and diameter for impacts at normal obliquity are discussed in section 2.4.2.1 below. Modifications to the equations to describe oblique impacts are discussed in section 2.4.2.2.

2.4.2.1 Normal Impacts. The large impact velocity crater depth relation for normal impacts was developed from a coupling parameter analysis (See Ref. 35 for details on scaling crater dimensions using a coupling parameter.) and fit to test data from Ref. 36. The resulting equation used in PEN4 for large velocity impacts is,

$$P = 0.281 d (\rho/\delta)^{1/3} [\delta V^2/(2Y)]^{0.31}, \quad (75)$$

where d is the projectile diameter (or the fragment diameter $2R_f$ on second plate impacts), δ is the projectile density, ρ is the target density, and Y is the target ultimate tensile strength under uniaxial stress. Equation 75 applies mostly to impacts above 3 to 4 km/s. Equation 75 is shown cross plotted with the test data from Ref. 36 in figure 2-29.

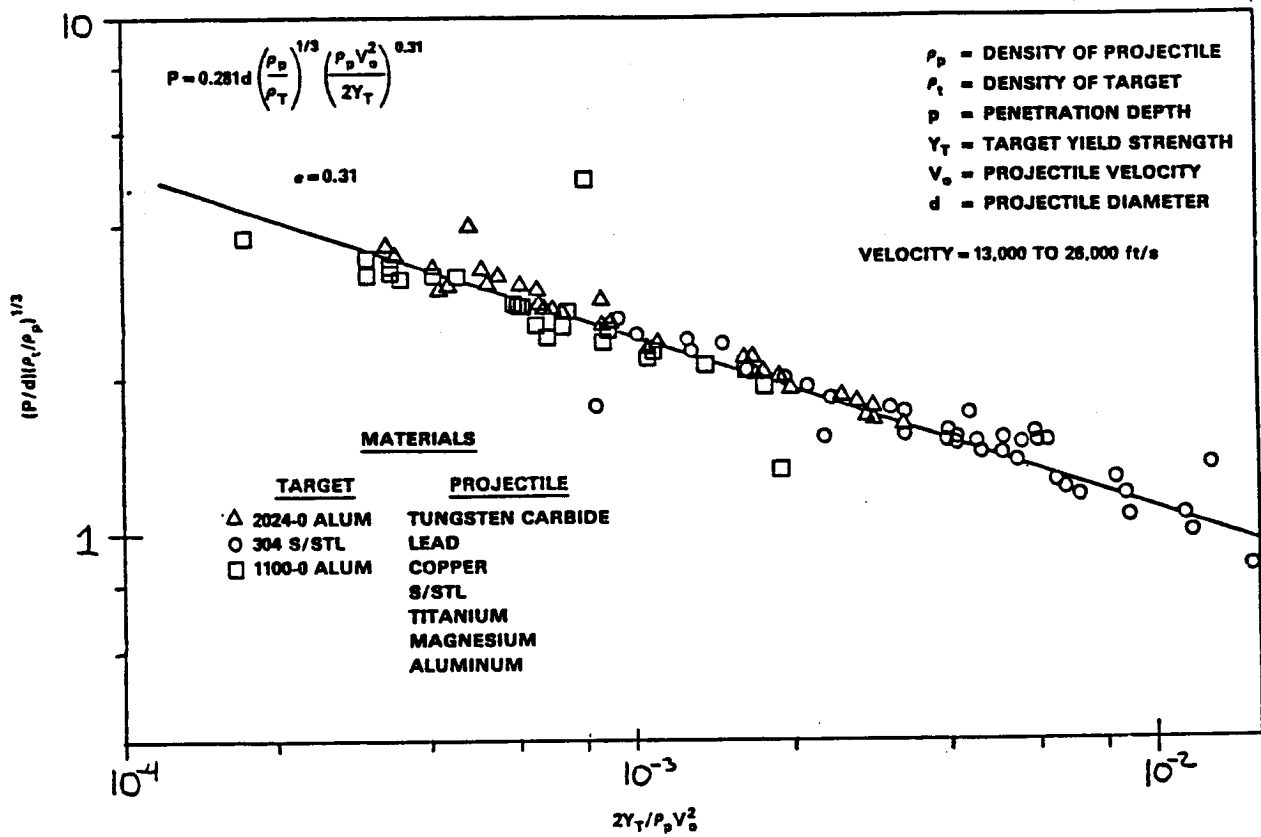


Figure 2-29 Large impact velocity crater depth relation.

The small impact velocity crater depth relations for normal impacts were developed from empirical fits to test data. Steel impacts of 2024-T3 aluminum semi-infinite target data from Ref. 37 is shown in figure 2-30. The fit used in PEN4 for small impact velocities and shown as the line in figure 2-30 is expressed mathematically as,

$$P = d [V/(3.8 \text{ km/s})]^{1.32}. \quad (\text{steel striking al}) \quad (76)$$

The fit made to 2024-T3 impacts of 2024-T3 semi-infinite plates test data from Ref. 17 is also shown in figure 2-30 and is expressed mathematically as,

$$P = d [V/(3.0 \text{ km/s})]^{1.16}. \quad (\text{al striking al}) \quad (77)$$

The decision of whether to use the large or small impact velocity crater depth relation is made by determining which relation calculates the smallest crater depth and using that relation. For most typical impact conditions, the transition between the small and the large impact crater depth relations occurs near 3 km/s impact velocity.

Large impact velocities typically produce hemispherical craters. However, for small impact velocities, the crater depth to diameter ratio depends on the ratio of projectile to target densities and the projectile and target strength. Steel onto aluminum impacts at small impact velocities produce deep and narrow craters, while aluminum on aluminum impacts at small impact velocities produce broad and shallow craters.

This behavior is modeled empirically in PEN4. Crater depth to diameter data are plotted in figure 2-31 for steel onto aluminum impacts and for aluminum on aluminum impacts. The relation used to fit the steel impacting aluminum data is

$$P/D = (V/4.6 \text{ km/s})^{-0.2} \quad (\text{for } V > 3.90 \text{ km/s}) \quad (78)$$

$$P/D = (V/3.8 \text{ km/s})^{1.32} \quad (\text{for } V < 3.90 \text{ km/s}). \quad (79)$$

Equation 79 was constructed from Eq. 76 because at the smallest impact velocities the crater depth grows without the diameter getting larger. Thus Eq. 76 can be used to estimate the crater depth to diameter ratio by setting the projectile diameter d equal to the crater diameter D .

The relation used for calculating the crater depth to diameter ratio for aluminum onto aluminum impacts is,

$$P/D = 0.5 [1 - \exp(-V/1.7 \text{ km/s})]. \quad (80)$$

Equations 78 through 80 are plotted in figure 2-31 and fit the data well.

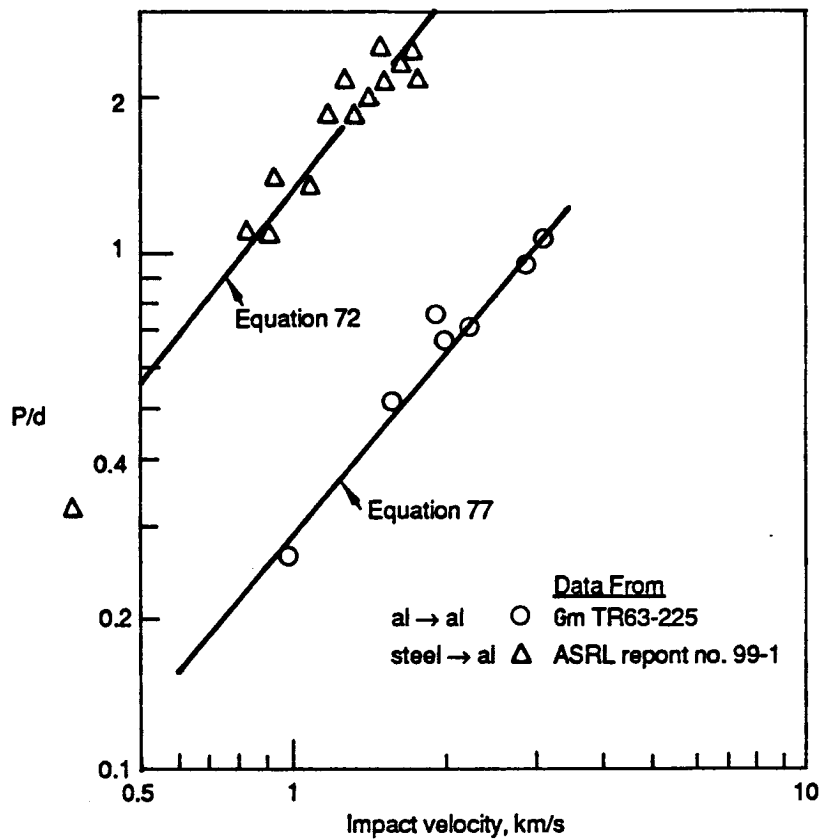


Figure 2-30 Small impact velocity crater depth relations.

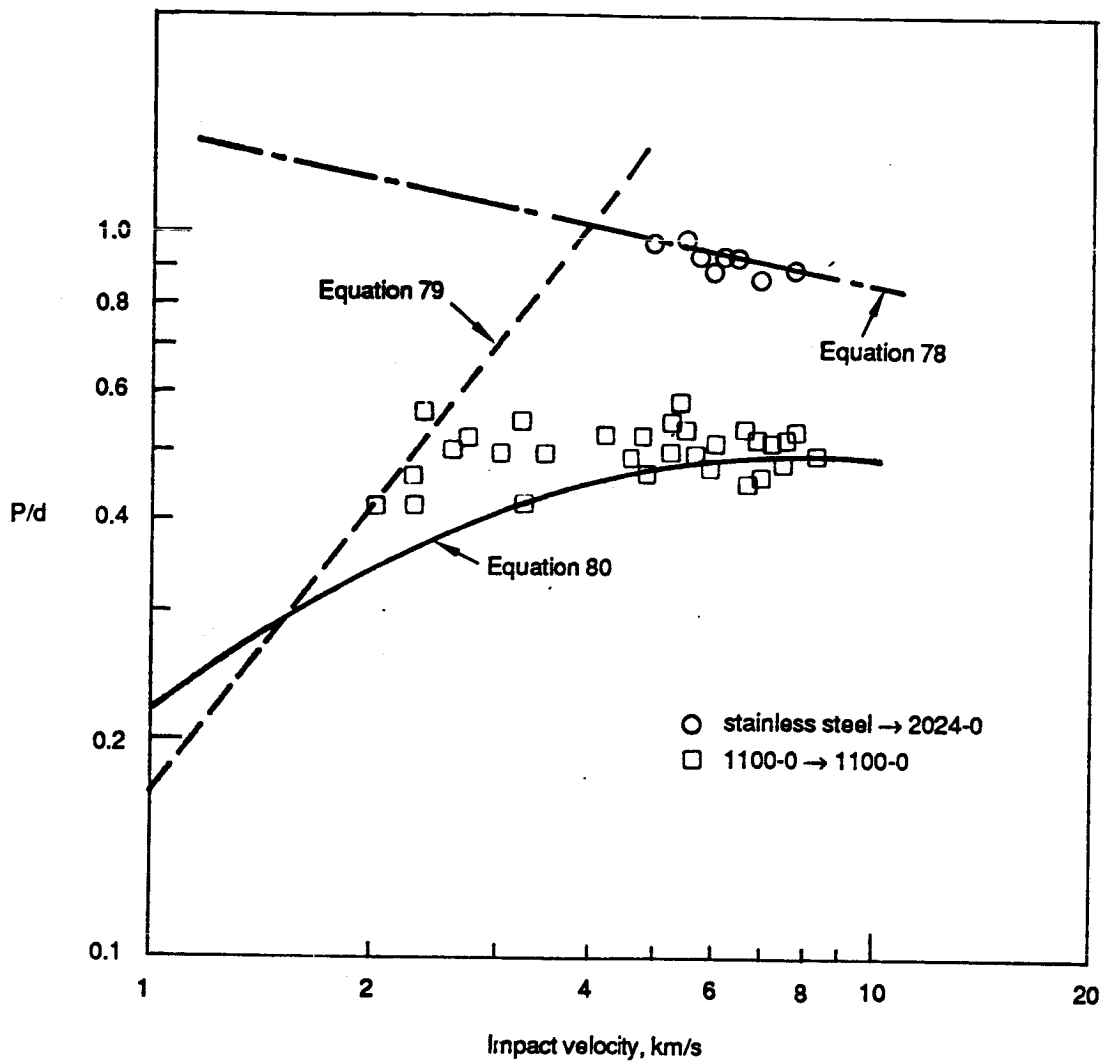


Figure 2-31 Crater depth to diameter relations for small impact velocities.

2.4.2.2. Oblique Impacts. Few tests have been performed to determine the effect of angle of obliquity on the impact crater dimensions. What data that were collected are reviewed in Ref. 37. It is claimed for the large impact velocity case that angle of obliquity effects on the crater volume can be accounted for by replacing the impact velocity V in the crater volume relation with V_n , the normal component of the impact velocity, i.e., $V_n = V \cos \theta$. Lacking anything better, V_n is also used in the small impact velocity crater depth relations, Eqs. 76 and 77, as well as the large impact velocity crater depth relation, Eq. 75. Furthermore, this empirical result is applied to the ratio of crater depth to crater diameter in PEN4, i.e., Eqs. 78 through 80. This is certainly an oversimplification of what occurs in the small impact velocity case; however, it has at least the right trend.

2.4.3 Multiple Cratering and the Probability of Perforation.

PEN4 superimposes multiple projectile and first plate fragment impacts to determine whether the craters formed by these combined effects are deep enough to perforate the second plate. Each unique combination of multiple impacts of fragments that forms a crater is referred to as a hole type. The cumulative crater depth from multiple impacts for any hole type is calculated by summing the crater depths of the individual fragments involved.

The probability of perforation of the second plate is calculated in four steps. First, a list of all nonperforating hole type descriptions is generated. Second, a table of the probability of k multiple impacts $P(\text{Bin}, k)$ is generated for each fragment size bin. Third, the probability of occurrence for each hole type is calculated by multiplying the $P(\text{Bin}, k)$ entries to create a compound probability of occurrence of each hole type description. Fourth, the nonperforating hole type probabilities are summed together to calculate the probability of no perforation, which is subtracted from one to obtain the probability of perforation for the given spray area.

This process is illustrated in figure 2-32 for a three size bin example. The first step in figure 2-32 builds up a list of hole types, or combinations of multiple fragment impacts that do not perforate the plate. The columns in step 1 are the bin numbers. Bin 1 is the smallest size, bin 2 is the intermediate size, and bin 3 is the largest size fragment. The rows in the table are the iteration numbers for the calculation; each row describes a hole type. The elements of the table are the number of impacts at a single point by that size bin. To determine the total number of impacts at a point add across the row.

The first hole type of step 1 is the trivial calculation of whether no impacts will perforate the plate. The number of impacts by the smallest fragment, bin 1, is incremented until the multiple crater depth is calculated to exceed the thickness of

D180-30550-2

STEP 1 Combinations of Fragments that do not Perforate.

<Cycle 1>					<Cycle 3>				
Hole \ Bin number	1	2	3	Perforated	Hole \ Bin number	1	2	3	Perforated
type					type				
1	0	0	0	No	8	0	2	0	Yes
2	1	0	0	No					
3	2	0	0	No					
4	3	0	0	Yes					
					<Cycle 4>				
					9	0	0	1	Yes
<Cycle 2>									
5	0	1	0	No					
6	1	1	0	No					
7	2	1	0	Yes					

STEP 2 Calculation of Probability of Multiple Impacts by Fragments of One Size.

Bin \ number \	k	0	1	2	3	...
1		P(1,0)	P(1,1)	P(1,2)	P(1,3)	...
2		P(2,0)	P(2,1)	P(2,2)	P(2,3)	...
3		P(3,0)	P(3,1)	P(3,2)	P(3,3)	...

STEP 3 Calculation of Hole Type Probabilities

$$\begin{aligned}
 &P(0,0,0) - P(1,0) P(2,0) P(3,0) \\
 &P(1,0,0) - P(1,1) P(2,0) P(3,0) \\
 &P(2,0,0) - P(1,2) P(2,0) P(3,0) \\
 &P(0,1,0) - P(1,0) P(2,1) P(3,0) \\
 &+ P(1,1,0) - P(1,1) P(2,1) P(3,0) \\
 &\text{Compound} \\
 &\text{Probability of} \\
 &\text{no perforation}
 \end{aligned}$$

STEP 4 Second Plate Hole Area

$$\text{Hole Area} = \text{Spray Area} * (1 - \text{Compound Probability of no Perforation})$$

Figure 2-32 Schematic Representation of the Calculation of probability of Perforating the Second Plate.

the target plate. In figure 2-32 this occurred at hole type 4 with the multiple impact of three of the smallest size fragments. In cycle 2 of step 1 in figure 2-32 the number of smallest fragments is reduced to zero and the second largest fragment size bin, bin 2, is incremented to 1 fragment. Hole type 5 of figure 2-32 did not perforate, so on hole type 6 the number of fragments in the smallest bin, bin 1, is incremented to 1. Bin 1 is incremented until a perforation is calculated at hole type 7. Bin 1 is again reduced to zero and bin 2 is incremented to 2. Hole type 8 in cycle 3 also perforated the plate. Finally in Cycle 4, Bin 2 is reduced to zero and bin 3 is incremented to 1 to determine whether the largest size fragment will perforate. Thus a total of 5 hole types were determined to not perforate the target plate in the example shown in step 1 of figure 2-32.

In step 2 the probability of k impacts by fragments with radius r (i.e., all of one size bin) is calculated. This probability is denoted as $P(\text{Bin}, k)$ in the table listed as step 2 of figure 2-32. For example the probability of two fragments from bin 1 landing in the same crater would be denoted as $P(1, 2)$ and would be found in the third column of the first row. The binomial probability distribution is used to calculate $P(\text{Bin}, k)$ and is described more fully below in section 2.3.4.1.

Step 3 illustrates the calculation of probabilities of non perforating hole types. The $P(\text{Bin}, k)$ values calculated in step 2 of figure 2-32 are multiplied together for those hole types found in step 1 that do not penetrate.

The probability of multiple impacts by fragments of one size is discussed below. As discussed in section 2.4.1, all projectile/target debris fragments are assumed to have an equal probability of impacting in any multiple crater, no matter what the fragment size or where it came from: within the projectile or the target plate plug. Furthermore, the probability of any fragment impacting within a multiple crater is not assumed dependent on the fragments that impacted before it, i.e., the impacts are independent events. Thus, the pertinent statistical distribution for calculating the probability of k fragments impacting the same point, $P(k)$, is the binomial distribution.

The parameters defining this distribution are the average number of impacts within the crater area, λ , the actual number of impacts, k , and the total number of fragments with radius r , N_r . The probability, P_c , that a fragment impacts within the effective crater area is,

$$P_c = \lambda/N_r = A_c/A_s. \quad (81)$$

The variable P_c is also called the probability of success. The probability of failure, q , is

$$q = 1 - P_c. \quad (82)$$

For certain parameters the binomial distribution becomes too time consuming

to calculate, or too difficult to calculate accurately. Thus, the Poisson and normal distributions are used to approximate the binomial distribution for certain values of N_r , λ , and P_c . The appropriate statistical distribution to use in PEN4 for calculating $P(k)$ is determined by the following relationships:

- a) The binomial distribution is used whenever the tests for using the Poisson or normal distributions fail. Thus, the binomial distribution is generally used for impacts involving small numbers of fragments, e.g. $N_r < 50$.
- b) The Poisson distribution is used when $N_r > 50$ and $0 < \lambda < 10$. That is, the Poisson distribution applies to few successes, λ , occurring during large numbers of trials, N_r . The probability of success, P_c , is small ($P_c < 0.1$) when the Poisson distribution is used.
- c) The normal distribution is used when the probability of success is not too close to zero or one ($0.1 < P_c < 0.9$), and the number of fragments is large ($N_r > 9/P_c (1-P_c)$).

The three distribution functions for the probability of k hits, $P(k)$, are:

$$P(k) = N_r! / [k! (N_r - k)!] P_c^k (1 - P_c)^{N_r - k}, \quad \text{binomial (83)}$$

$$P(k) = \lambda^k \exp(-\lambda) / k!, \quad \text{Poisson (84)}$$

$$P(k) = 1 / [(2\pi)^{1/2} \sigma] \exp(-1/2 [(x - \mu) / \sigma]^2), \quad \text{normal (85)}$$

where $\sigma^2 = N_r P_c (1 - P_c)$.

2.4.4. Holed Out Area on the Second Plate.

Each probability can also be interpreted as the fraction of spray area A_s covered by holes of this description. The sum of the probabilities for all nonperforating hole types is the compound probability of no perforation. This is shown on step 3 of figure 2-32. The probability of perforation is just one minus the compound probability of no perforation. The second plate hole area is the spray area times this probability of perforation as in step 4.

2.4.5 Number of Fragments Residual After the Second Plate

Calculation of the number of fragments in a given bin that are stopped by the second target plate is performed in four steps.

1. The area covered by each nonperforating hole type is calculated. This variable is called HOLETYPEAREA in PEN4 and is calculated by multiplying the hole type probability times the spray area.
2. Divide each HOLETYPEAREA by the crater area to determine the number of these holes.
3. Multiply the number of holes for each hole type by the number of fragments from each bin that are in that kind of hole. This gives the number of fragments stopped for each hole type.
4. Sum the number of fragments stopped by all hole types, producing the total fragments stopped by the target plate.

2.4.6 Increased Penetration From Plate Spall

Calculation of the number of fragments in a given bin that are stopped by the second target plate is performed in four steps.

1. The area covered by each nonperforating hole type is calculated. Hole type area is the hole type probability times the spray area.
2. Divide each hole type area by the crater area to determine the number of these holes.
3. Multiply the number of holes for each hole type by the number of fragments from that bin are in that kind of hole.
4. Sum the number of fragments stopped by all hole types, producing the total fragments stopped by the target plate.

Short duration stress waves from impact of thin plates can reflect from the rear surface of the target plate as tensile waves. If the tensile stress amplitude is large enough, then the target material may fail by fracture along a plane parallel to the rear target surface forming a spall. If sufficient impulse is applied to the spall by the impact, then the spall will fragment. Thus it is possible under certain impact conditions to damage a second target plate by more than multiple cratering.

Examination of second plates from tests performed for Ref. 15 showed that spall occurred during many of the tests. It was thought that the increased penetration resulting from spall would significantly reduce the critical projectile diameter required for perforation of an aluminum plate array by an aluminum projectile, and to a lesser degree, the perforation of an aluminum plate array by a steel projectile. Thus a relation for spall was thought mandatory.

Section 2.4.6.1 below gives the derivation of the relation used in PEN4 to determine the critical velocity for rear-face spall from fragment cloud impact of the second plate. The rear-face spall fragment distribution used in PEN4 is described in section 2.4.6.2.

2.4.6.1 Spall Threshold Velocity. An analytic relation for threshold velocity for plate spall from the impact of a fragment cloud is developed in this section using an energy criterion analogous to that used for the residual velocity in section 2.3.3.

Second plate spall geometry is illustrated in figure 2-33. A disk-shaped plug of material removed from the target second plate by the shock loading from the impact with the projectile/target-first-plate debris. Work must be done to plug the target first plate and to shear the target second plate along the cylindrical surface with height h_s and to fail the target second plate in tension along the circular surface of radius x . The work done to form plug from the first plate and the two fracture surfaces in second plate is,

$$W = (2\pi a_1 \tau t^2) + (2\pi x h_s^2 \tau) + (\pi x^2 \Gamma) \quad (86)$$

where τ is the dynamic shear strength, t is the target first plate thickness, d is the projectile diameter, h_s is the target second plate spall height, Γ is the fracture surface energy of the target second plate material, a_1 is the fragment cloud thickness from the projectile/first-target-plate debris, and a_2 is the maximum radius of impact of the projectile/first-target-plate fragment cloud on the target second plate. The first term on the right-hand side of Eq. 86 is the plastic work done to remove the plug from the target first plate. The second term on the right-hand side of Eq. 86 is the work done to shear the second plate along a cylindrical surface. The third term on the right-hand side of Eq. 86 is the work done to form the circular fracture in the second plate.

The following assumptions are made for the evaluation of Eq. 86,

- 1) $a_1 = t + d/2$
- 2) $a_2 = t + s + d/2$
- 3) x varies from 0 to $a_2 + t_2$.
- 4) the debris cloud thickness varies with radius x
 $y = h [1 + \cos(\pi x/a_2)]/2$
 where $h = d^3/1.78a_2^2 + (a_1^2 t/.3a_2^2)$
- 5) the spall thickness equals the debris cloud thickness
 $h_s = y$
- 6) projectile and first plate debris travel at the same velocity v_r .

The target material shear strength is assumed dependent on the impact velocity,

$$\tau = \tau_0 \exp(-V/V_c) \quad (87)$$

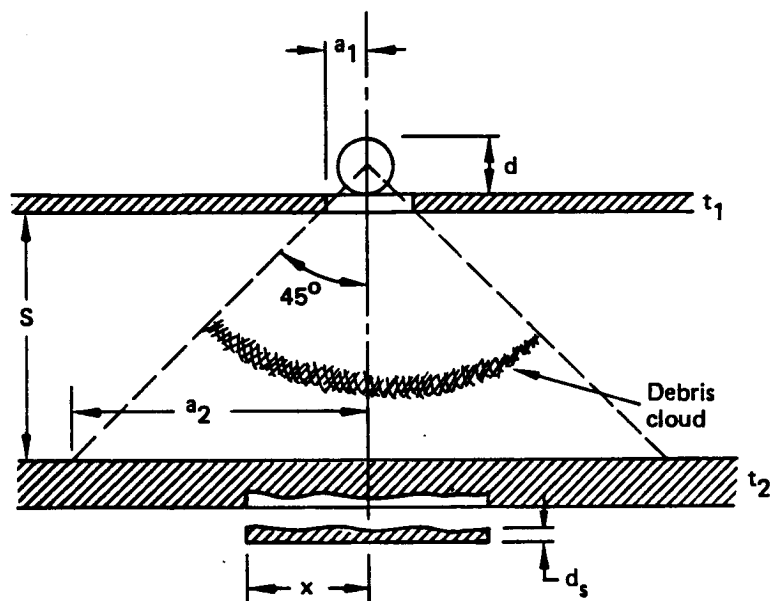


Figure 2-33 Geometry and definition of variables used to evaluate two plate spall.

and the fracture surface energy of the target second plate is assumed to be

$$\Gamma = K_{1c}^2 / (\rho c^2) \quad (88)$$

The total initial projectile energy E required to perforate the target first plate and just barely spall the target second plate (i.e., impart no velocity to the spall) is defined as,

$$E = 1/2 m V_s^2, \quad (89)$$

where V_s is called the projectile threshold velocity for second plate spall.

The energy E is also assumed equal to E_f , the energy of a free impact between the projectile and the target first plate plug, plus W , the work done to remove the plug from the target first plate and form the spall on the target second plate, plus T_r , the residual kinetic energy of the projectile and the target first plate plug after the projectile impacts the target first plate but before the projectile/target-first-plate debris impacts the target second plate,

$$E = E_f + W + T_r \quad (90)$$

The energy of a free impact E_f between the projectile and the target first plate plug with mass m_s is equivalent to Eq. 12, which is reproduced as Eq. 91 below,

$$E_f = m_s / (m + m_s) \cdot 1/2 m V_s^2 (1 - \epsilon^2). \quad (91)$$

The residual kinetic energy, T_r , of the projectile and the target first plate plug is,

$$T_r = 1/2 (m + m_s) V_r^2. \quad (92)$$

Substituting Eqs. 91 and 92 into Eq. 90 and solving for W gives

$$W = 1/2 m V_s^2 (m + m_s \epsilon^2) / (m + m_s) - 1/2 (m + m_s) V_r^2. \quad (93)$$

The residual velocity of the projectile and target first plate debris V_r is solved for using Eq. 21, reproduced below as Eq. 94,

$$V_r = m / (m + m_s) (V_s^2 - V_{50}^2)^{1/2}. \quad (94)$$

where V_{50} is the ballistic limit velocity of the projectile striking the target first plate. For analytic simplicity the aluminum onto aluminum V_{50} relation, Eq. 1, has been approximated by,

$$V_{50} = 1.2 \text{ km/s } (t/d)^{0.90} \quad (95)$$

Setting Eqs. 86 and 93 equal to each other and solving for V_s gives,

$$q_1 V_s^2 = q_2 + q_3 \exp(-V_s/V_c) \quad (96)$$

$$q_1 = 1/2 (m m_s \epsilon^2 / (m+m_s)) \quad (97)$$

$$q_2 = 1/2 [2\pi x^2 K_{1c}^2 / (\rho c^2) - m^2 V_{50}^2 / (m+m_s)] \quad (98)$$

$$q_3 = 2\pi r_0 (a_1 t^2 + x h_s^2) \quad (99)$$

The two parameters V_c and ϵ are treated as free parameters and are used to adjust the results of Eq. 96 to fit test data from Ref. 15. The result of the fit is shown in figure 2-34. Note that Eq. 96 is an implicit function, thus V_s must be solved for iteratively. (In PEN4 the impact velocity is substituted for V_s in Eq. 96, and a test is made to see whether the left-hand side of Eq. 98 exceeds the right-hand side. If so, then the impact velocity exceeds the spallation threshold velocity.)

2.4.6.2 Spall Fragment Mass Distribution. PEN4 does not keep track of the second plate spall fragments mass distribution separately, just as it does not kept track of the plate fragment mass distribution. The total mass of material spalled from the target plate is calculated from the spall radius x and the spall thickness h_s assuming a disk shaped volume,

$$M_{\text{spall}} = \rho \pi x^2 h_s \quad (100)$$

The spalled off target plate mass is factored into the projectile mass and used to calculate the number of fragments. The projectile mass distribution described in section 2.3.6 is then used to calculate the probability of multiple impacts.

2.4.7. Second Plate Penetration by Icy Meteoroids.

PEN4 was designed to solve the problem of perforation of aluminum plate arrays by dense tantalum and steel projectiles. Hence, it was thought unnecessary to model in detail the impact of shield plate fragments onto the second plate, because the projectile fragments would be much more penetrating. The work performed under the contract NAS8-36426, "Space Station Wall Design and Penetration Damage Control," and Boeing Independent Research and Development funds to extend the PEN4 methodology to impact of aluminum projectiles onto aluminum plates has pointed out the shortcomings of the PEN4 methodology when applied to problems with comparable projectile and target densities. Since the orbital debris projectile fragments have similar densities to the shield plate fragments, they are no more penetrating. Hence, the plate fragments make a significant contribution to perforation of the aluminum plate array, which can not be neglected.

Unfortunately, the SM-1 and NAS8-36426 testing did not quantify the plate fragment damage effects, since only witness plate data were collected and

Solid Line Represents Ideal Agreement.

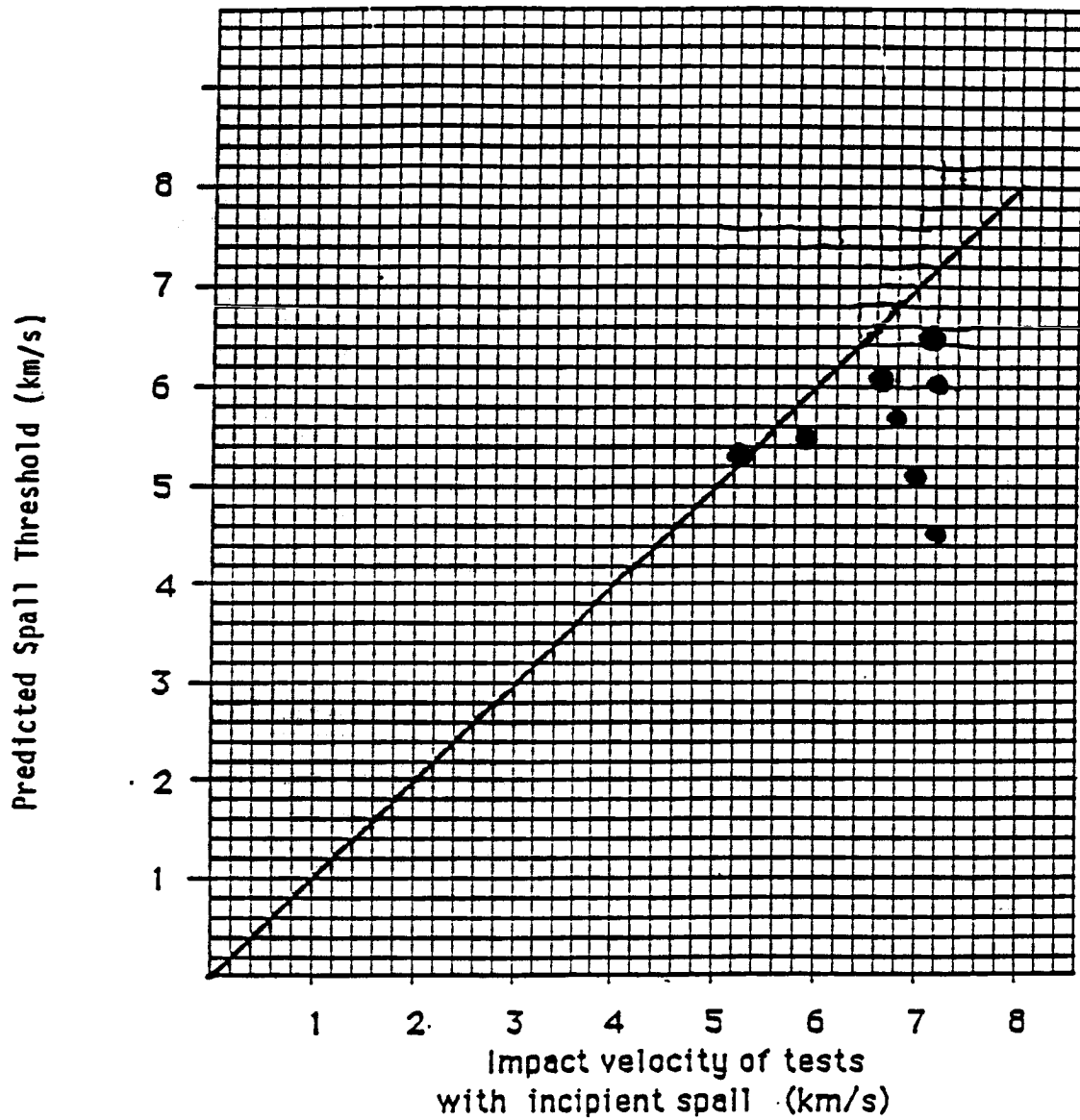


Figure 2-34 Comparison of results from Eq. 96 with SM-1 test data.

no attempt was made to capture the plate fragments produced by the impact. The witness plates from the SM-1 and NAS8-36426 testing performed at NASA/MSFC that were inspected, though, were thought to show perforation for oblique impacts that could only have come from plate fragments and not projectile fragments. To model this important phenomenon two fixes were applied to PEN4: 1) a model of the increased penetration from spallation of plate fragments from the target plate was developed in section 2.4.6, and 2) a model based on the hypothesized large differences between the plate and projectile largest residual fragment mass at oblique impact angles was developed in section 2.3.5.4.

The above mentioned problems are compounded for icy meteoroid impacts, since there are not even the witness plate data that were available for aluminum impacts. Hence, the following exposition on icy meteoroid impacts is at best speculative. Since nothing is known about the impact of ice onto aluminum, it is not thought prudent to develop a complicated model. Thus the perforation of aluminum plates by icy meteoroids is conceptualized as the icy meteoroid volatilizing when it impacts the shield for all impact velocities and thus not contributing directly to second plate perforation from cratering of aluminum by ice. Therefore, in this model, all second plate perforation comes from the aluminum shield plate fragments produced by the impact between the meteoroid and the shield. Therefore, the only changes made to PEN4 were to: 1) develop a ballistic limit velocity for ice impacting aluminum, 2) eliminate the projectile fragmentation threshold velocity calculation, and 3) modify the largest residual fragment mass calculations.

In lieu of any information on the ballistic limit velocity of ice striking aluminum, an estimate of the ice V_{50} was made as follows. The generalized ballistic limit velocity relation, Eq. 5, derived by a dimensional analysis argument is the starting point. Equation 5 requires V_{50} to be proportional to the target plate thickness, but does not specify the functional dependence on t/d and ρ/δ . The THOR 41 (Ref. 10) V_{50} relations for three projectile materials striking aluminum plate were cross plotted and the results are displayed in figure 2-35 for the purpose of determining these functional dependencies. The THOR 41 relations are equivalent to a power-law dependence on t/d as shown in figure 2-35. However, note that the curves are nearly parallel, indicating that the functional dependencies on t/d and ρ/δ in Eq. 5 are decoupled and can be written as,

$$V_{50} = (k/\rho)^{1/(2-n)} t^{-n/(2-n)} f(t/d) g(\rho/\delta). \quad (101)$$

The exponent on t was taken to be the average of the three values taken from the THOR 41 fits to aluminum, steel and tungsten striking aluminum. The THOR 41 exponents on t/d for the three projectile materials were also averaged. The functional dependence g on ρ/δ was determined by plotting the values of V_{50}

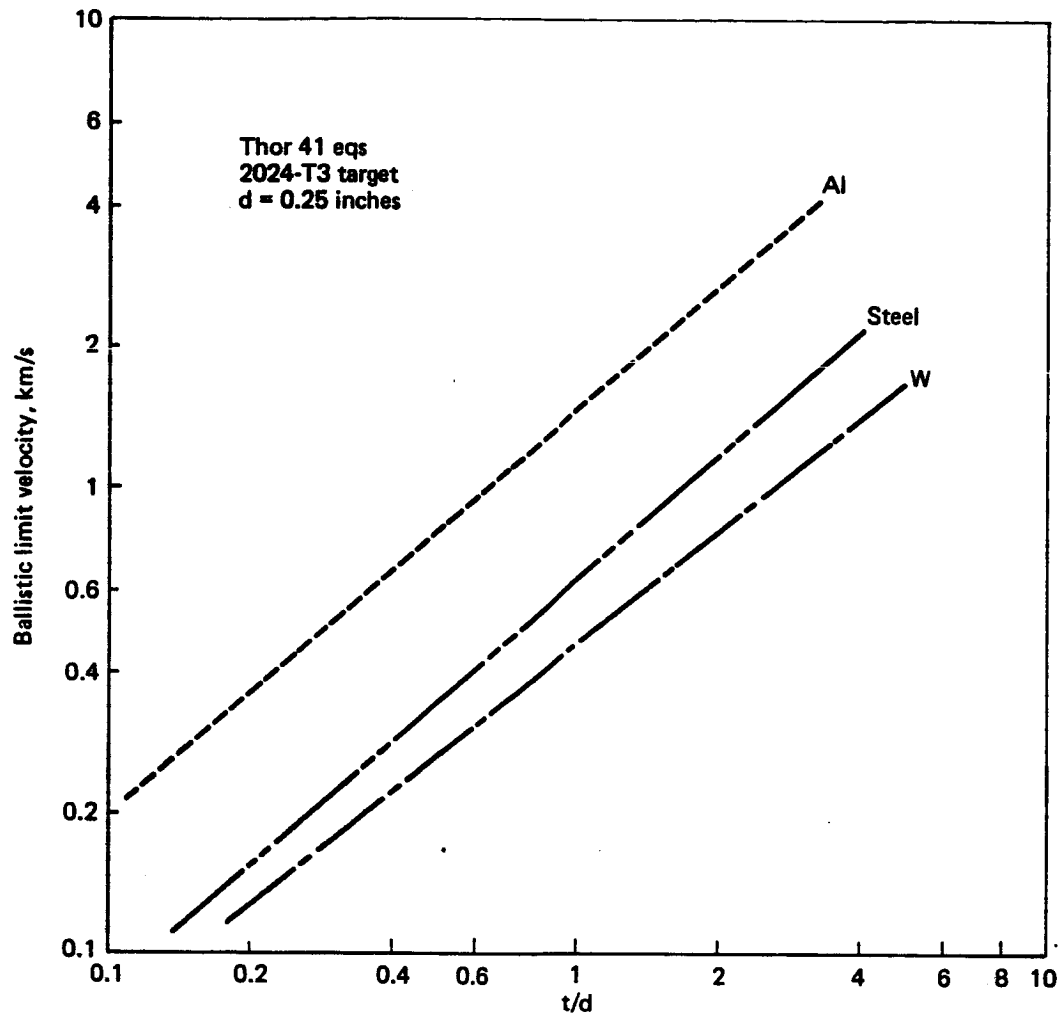


Figure 2-35 THOR 41 ballistic limit velocity relations for aluminum, steel, and tungsten striking aluminum.

versus ρ/δ for the three equations evaluated at $t/d = 0.5$ and $d = 0.25$ inches. The resulting plot is shown in figure 2-36. It was assumed that g is a power-law on ρ/δ ; however, there are insufficient data to verify this. The composite equation constructed from the two functional dependencies is,

$$V_{50} = 2.45 \times 10^5 \text{ cm/s cm}^{0.15} t^{-0.15} t/d (\rho/\delta)^{0.64}. \quad (102)$$

PEN4 only uses Eq. 102 to calculate the ballistic limit velocity for ice striking aluminum. Though Eq. 102 was derived by a procedure that should lead to a general equation applicable to all projectile materials, it is only applied to ice in PEN4. Too few data were examined to validate the claim that the only projectile material important to the ballistic perforation of aluminum plates is the projectile density. This is actually thought to be too simple; the projectile strength is also thought to enter the general ballistic limit velocity relation.

Since no information is available for quantifying the sizes of plate fragments produced from the impact of icy meteoroids onto aluminum shields, the simplest possible modifications were made to the PEN4 fragment masses calculations. The equations from section 2.3.5 and 2.3.6 for projectile fragments masses from the impact of aluminum projectiles onto aluminum plates were used to calculate the masses of the plate fragments. To preclude the plate fragment masses from becoming larger than the mass of the material holed out of the shield plate, the mass of the material holed out of the shield is used for m in the fragment mass fraction distribution calculation and the diameter of a sphere with mass equivalent to the mass holed out of the shield used for d in the largest residual fragment mass calculation. However, it is thought that the diameter of the icy meteoroid should be used to calculate t/d , since this is a measure of loading duration.

The critical diameter curve for icy meteoroids calculated using the above procedure is plotted in figure 2-37 for 0-, 45- and 60- degrees obliquity. Note that for 0 and 45 degrees obliquity the meteoroid diameter required for perforation at 1 to 4 km/s impact velocity is slightly larger than the orbital debris diameter required for perforation, while at larger impact velocities the meteoroid and orbital debris critical diameters are about the same. It is not known why the critical meteoroid diameter at 60 degrees obliquity and 10 to 16 km/s impact velocity is so large.

If it is decided later to develop a model of penetration by icy meteoroids that confidence can be placed in, then testing is required: 1) to quantify the ballistic limit velocity of ice impacting aluminum, 2) to check the residual velocity relation, and 3) most importantly to quantify the plate fragment distribution. Incorporating the measured plate fragment distribution will require recoding PEN4 to consider the impact of shield plate fragments onto the second plate distinct from the impact of projectile fragments onto the second plate.

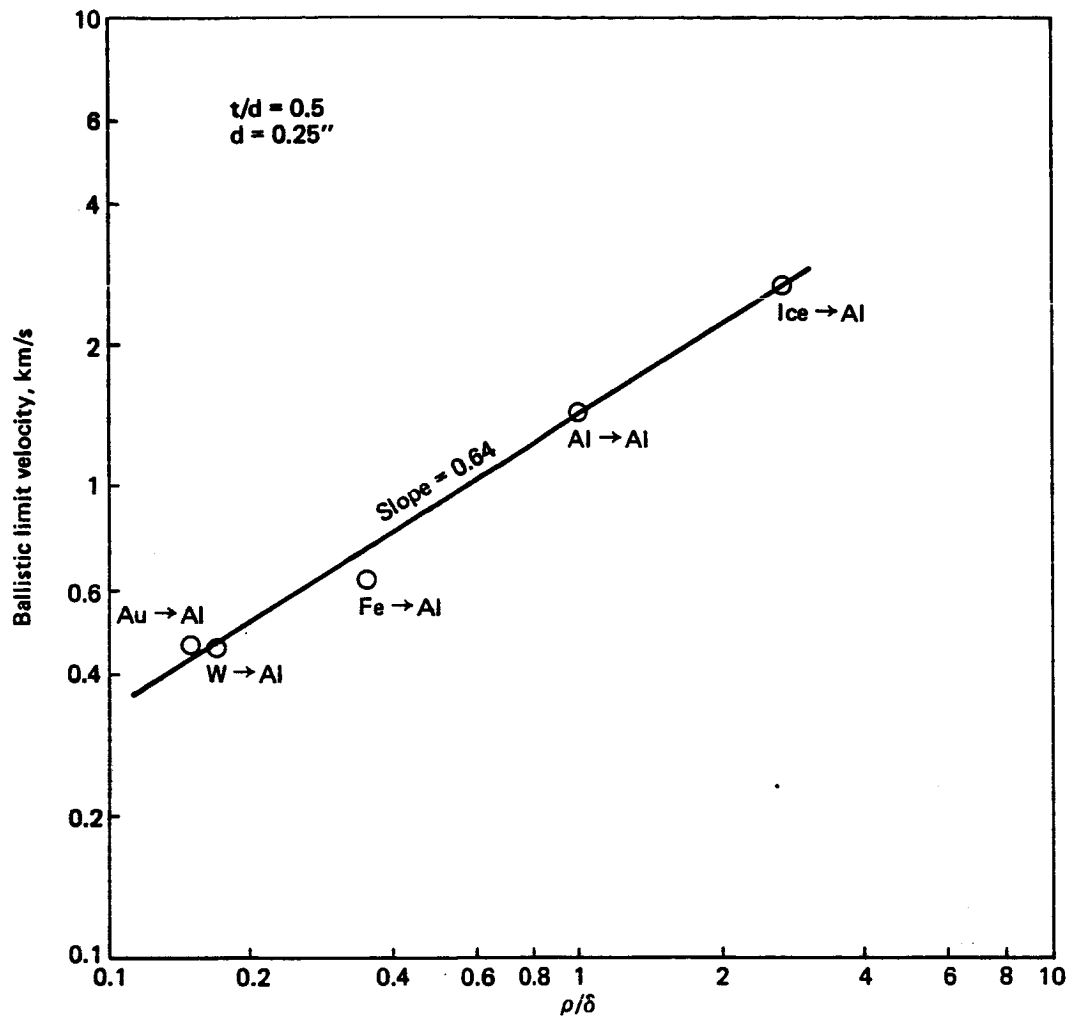


Figure 2-36 The ρ/δ dependence of the V_{50} relation for aluminum, steel, and tungsten striking aluminum.

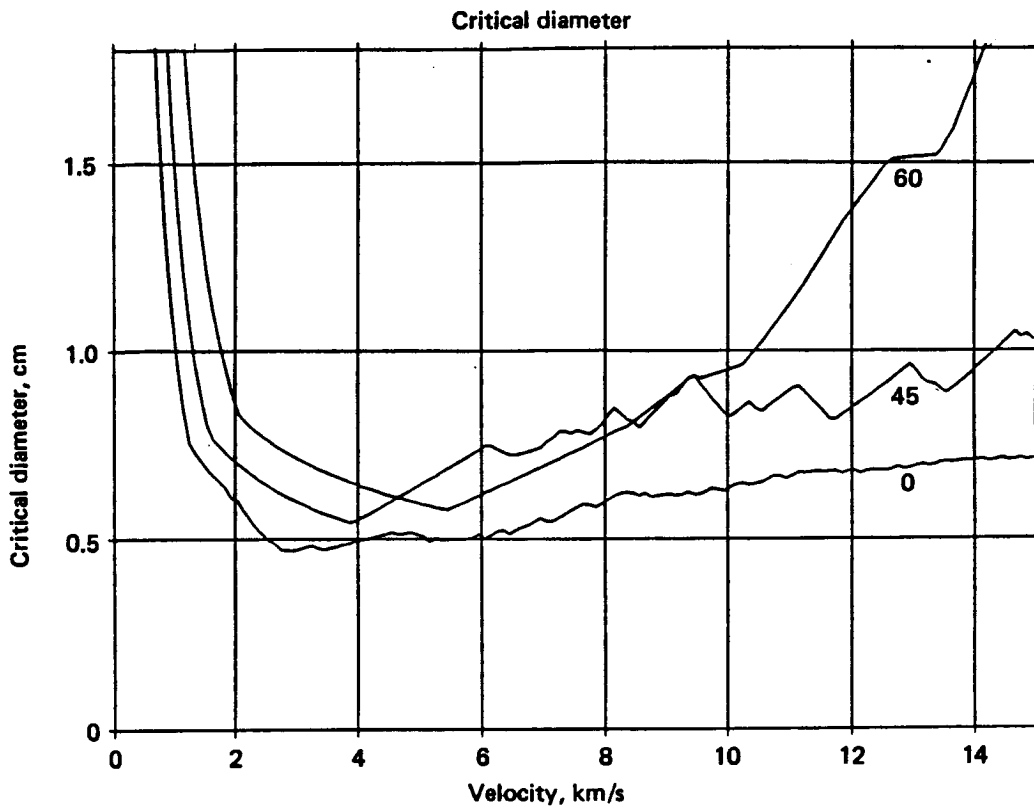


Figure 2-37 The calculated critical diameter curves for icy meteoroids striking aluminum for 0, 45, and 60 degrees angle of obliquity.

2.5 DATA OUTPUT

Data output consists of the following:

Yes/No decision on plate perforation

The following variables can be passed out of PEN4 by addition of the variables to the FORTRAN subroutine statement:

Residual velocity of the fragments

Diameters of the holes in the target plates

Fragment sizes

Number of fragments

Spray area

3.0 PENETRATION CODE LIMITATIONS

The limitations on materials, configurations, and intercept conditions are functions of the individual algorithms used in this analysis.

3.1 LIMITATIONS ON MATERIALS

PEN4 should be limited in application to 2024-T3 aluminum plates. This follows from the development of empirical relations for the ballistic limit velocity (and hence the residual velocity relation) from impact of 2024-T3 aluminum plate test data and the fits to fragment mass distribution test data from impacts of 2024-T3 aluminum plate material. Testing is required to determine whether other alloys of aluminum affect the critical diameter curve enough to warrant developing new relations.

The projectile material is limited to R_B 90 1018 steel and 2024-T3 aluminum projectile material. The relations developed for icy meteoroid projectiles are speculative and cannot be used with confidence. Testing is required to determine how to best implement an icy meteoroid projectile algorithm.

3.2 LIMITATIONS ON CONFIGURATIONS

The limitations on configuration are discussed for two factors, the projectile shape and the target plate arrangements.

3.2.1 Projectile Shape.

PEN4 is best applied to problems involving normal impact with blunt fragments. The ballistic limit velocity relation, the residual velocity relation, the fragmentation threshold relation, the largest residual mass relation, and the fragment mass distribution were all developed for flat impacts of blunt projectiles onto flat plates. The applicability of PEN4 to other shapes is unknown. It is known, however, that the impact of yawed cubes and cylinders can lead to fragments nearly an order of magnitude larger than for flat impacts (Ref. 26). This effect can easily lower the critical diameter curve by a third.

3.2.2 Plate Arrangements.

The target configurations are limited to the arrangement of two plates shown in figure 2-2. Note that a general angular dependence between the projectile and the two target plates, and the two target plates with each other, is not allowed. The impact configuration is limited to the case where the normals to the target plates and the projectile flight path all lie in the same plane.

3.3 LIMITATIONS ON INTERCEPT CONDITIONS

The limitations on intercept conditions are discussed for two factors, the impact angle and the impact obliquity.

3.3.1 Impact Velocity.

Intercept conditions are limited to the range from 0 km/s to impact velocities where the amount of melted projectile and target material becomes significant. The upper limitation on impact velocity is poorly defined at this time due to limited data quantifying the amount of melt. Recent hydrocode calculations indicate that this upper limit is around 11 km/s for $t/d = 0.25$. Thus PEN4 may not include the right phenomenology for impacts from 11 km/s and above.

3.3.2 Impact Angle.

Most of the testing with which PEN4 was compared with and most of the testing used to develop the PEN4 penetration relations were for normal impacts. Hence, the applicability of PEN4 to other than normal impacts is uncertain. As mentioned in section 3.2.1 the yawed impact of a cube or cylinder can result in significantly larger projectile fragments, and the same is true for the oblique impact of cubes and cylinders with zero yaw.

4.0 COMPARISON WITH TEST DATA

The two sections of this chapter compare PEN4 results with test data. The PEN4 results for mild steel cubes striking arrays of aluminum plates are compared with test data in section 4.1. The PEN4 results for 2024-T3 aluminum projectiles striking an array of aluminum plates are compared with test data in section 4.2.

Two more important checks on PEN4 have been made; however, they are of lesser interest than the comparisons with test data, so they have been included as appendices. Appendix E contains an important consistency check testing the convergence of the PEN4 technique; and, in appendix F, the large impact velocity behavior of PEN4 is compared with some hydrocode calculations.

4.1 Comparison With Steel Projectile Test Data.

PEN4 is expected to fit the steel projectile impacting aluminum plate test data best for two reasons. First, the PEN4 methodology assumes that the shield plate fragments do not significantly alter the penetration, hence they do not have to be modeled in detail. Second, all the projectile fragmentation relations in PEN4 come from fits to R_B 90 1018 steel projectile fragments test data.

The first comparison of PEN4 output with test data is a made to the total number of plates perforated in a 7 plate array. The test data were taken from NSWC TR-79-66, Ref. 38. The target plate array shot is described in the table below,

plate no.	thickness (in)	spacing (in)
1	1/16	10
2	1/8	10
3	1/8	10
4	1/8	3
5	1/8	3
6	1/8	3
7	1/8	

All the plates were 2024-T3 aluminum.

Comparisons were made with 9 shots. The table below lists the impact velocity, the projectile size, and the projectile shape and material type.

Shot no.	Impact Velocity (km/s)	Projectile Mass (g)	Projectile Type
1	1.98		R _C 30 sphere
9	2.21		R _B 90 cube
12	2.70		R _B 90 cube
4	2.86		R _C 30 sphere
13	3.23		R _B 90 cube
10	3.29		R _B 90 cube
5	3.67		R _C 30 sphere
3	4.69		R _C 30 sphere
11	4.69		R _B 90 cube

The test data are plotted in figure 2-38 as the hatched histograms, and the PEN4 results are plotted as solid histograms. All R_B 90 1018 steel cube data are fitted to within one plate. In all but one of the five cube shots PEN4 either predicted the number of plates perforated or predicted one fewer.

The R_C 30 4340 steel sphere data exhibit a different trend, however. Two of four PEN4 calculations predicted two fewer plates being perforated, and one of four calculations predicted one fewer plate being perforated. PEN4 appears to under predict the number of plates perforated by the harder and different alloy steel spheres. This result is not too surprising, since figure C-7 of Appendix C shows that the R_C 30 and 40 4340 steel cube largest residual mass data are larger than the R_B 90 1018 steel cube data for comparable t/d, d, and impact velocity. Therefore it is concluded that the material differences between R_B 90 1018 steel cube projectiles and R_C 30 4340 steel sphere projectiles is sufficiently large to preclude using PEN4 for another alloy of steel, without altering the fracture toughness used to calculate the steel largest residual fragment mass.

Examination of the PEN4 output indicated that multiple cratering did not determine the number of plates perforated. Each plate in the array that was perforated could be perforated by the largest residual fragment. This is illustrated in figure 2-39, which shows the critical diameter curves calculated for a R_B 90 1018 steel cubes striking an array of aluminum plates at 0, 45 and 60 degrees angle of obliquity. The target plate array used to compute figure 2-39 is different from that used to compute figure 2-38. The plate array used to produce figure 2-39 consisted of two plates, the first 1/16-inch thick spaced 4 inches from the second plate, which was 1/8-inch

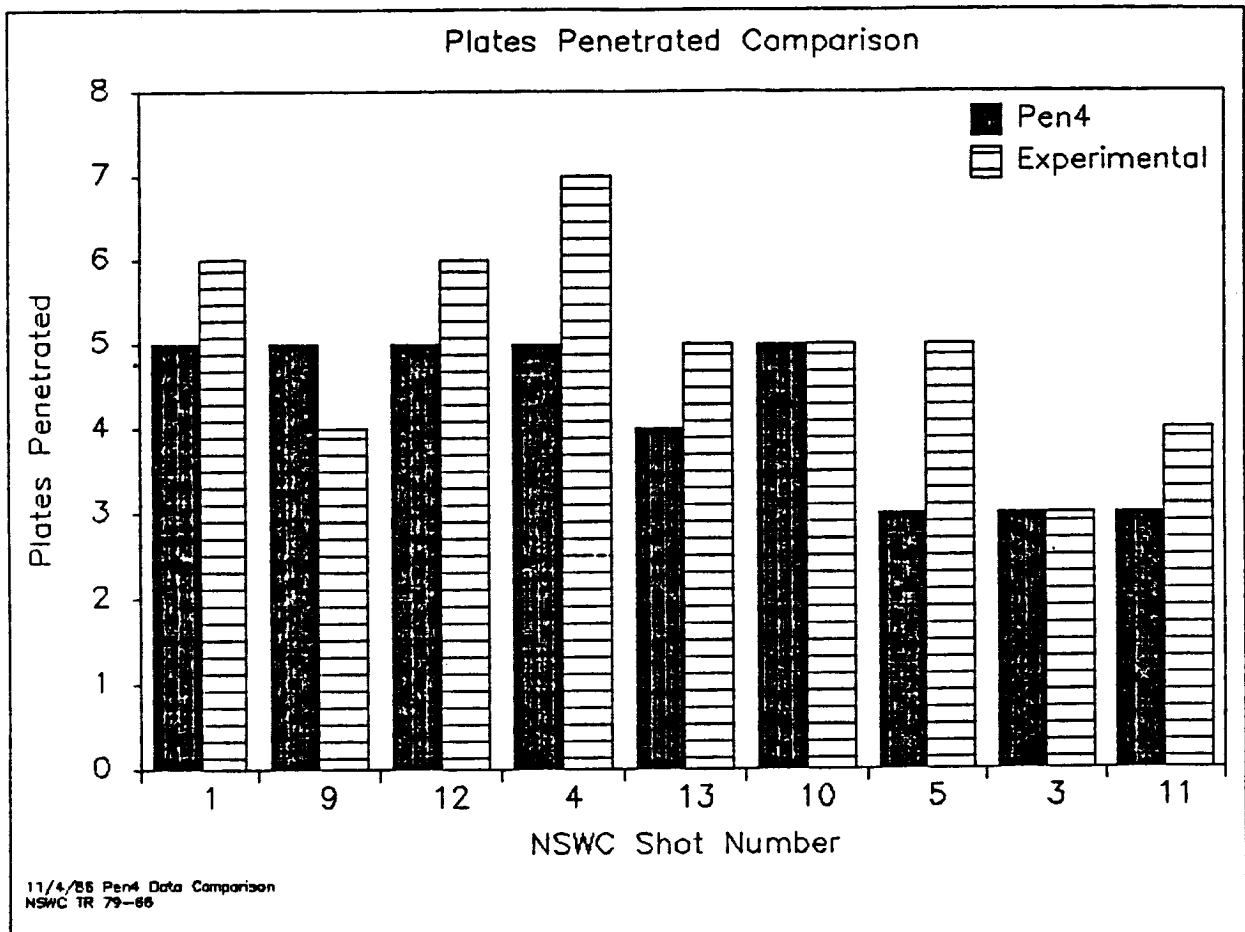


Figure 2-38 Comparison with NSWC TR-79-66 number of plates perforated data.

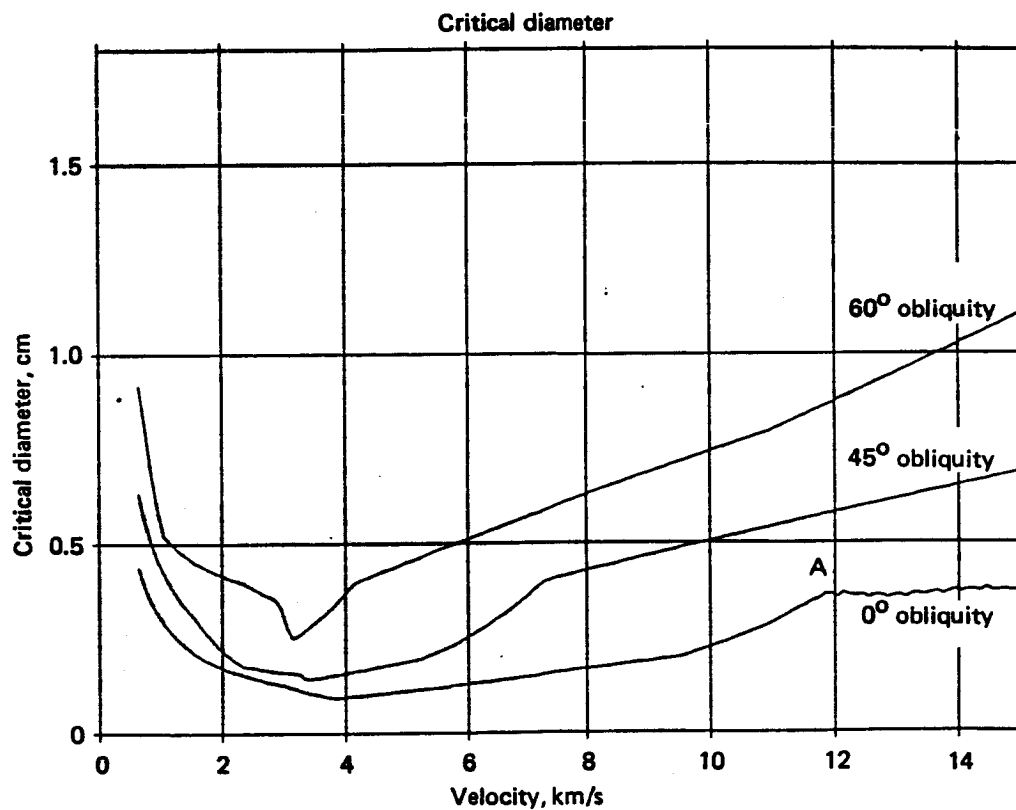


Figure 2-39 Critical diameter curves for R_B 90 1018 steel cubes striking 63 mil 2024-T3 shield plate spaced 4 inches from 125 mil 2024-T3 second plate.

thick. The curve to the left of point A on the 0-degree obliquity critical diameter curve is smooth indicating that the multiple cratering algorithm was not used, while the curve to the right of point A is jagged, indicating that the multiple cratering is determining the number of plates perforated. Note that the 45- and 60-degree obliquity critical diameter curves indicate that the multiple cratering algorithm was never used.

The test data are compared with the calculated second plate hole diameter from a previous version of PEN4 in figure 2-40. Note that the agreement is not good. It is not clear whether this indicates that the fragmentation of the shield plate fragments should be treated more accurately, the spatial distribution needs improvement, or a collective effect that is not modeled in PEN4, such as tearing out material between the holes or failure by impulse loading is important. This is the most significant issue remaining to be dealt with, and future testing must be directed towards resolving the problem. (See the recommendations in chapter 5.0.)

4.2 Comparison With Aluminum Projectile Test Data.

A critical diameter curve for perforation of a fixed two plate array by a 2024-T3 aluminum projectile at 0-degrees obliquity is plotted in figure 2-41. The first plate was 6061-T6 aluminum and was 63-mils thickness, while the second plate was 2219-T87 aluminum and was 125-mils thick. The separation between the two plates was 4 inches. (The test data were taken from Ref. 15.) Solid symbols indicate no perforation, open symbols indicate perforation, and half-filled symbols indicate perforation threshold. Note that PEN4 fits the data plotted in figure 2-41 well. This is by design. Two parameters in PEN4 are adjusted to cause the critical diameter curve to fit these data. The two adjusted parameters are the exponent on the velocity dependence of the largest residual fragment mass in the power-law roll off region (the exponent -6.2 in Eq. 49), and the minimum hole diameter counted as a perforation by PEN4. The first parameter adjusts the slope of the critical diameter curve for impact velocities between 3 and 8 km/s, while the second parameter adjusts the maximum critical diameter calculated for impact velocities larger than 10 km/s.

The critical diameter curve calculated by PEN4 was compared with the oblique impact data collected under the NAS8-36426 contract. The comparison with 45-degree impact data is shown in figure 2-42, and the comparison with 65-degree impact data is shown in figure 2-43. Note that the test data appear random and do not show a consistent threshold velocity for perforation.

Examination of series 206 and series 208 oblique impact tests suggested the following hypothesis for mechanisms governing perforation at oblique angles of impact. Inspection of the second plates from the series 206 and 208 tests revealed much larger craters in the plates than expected from

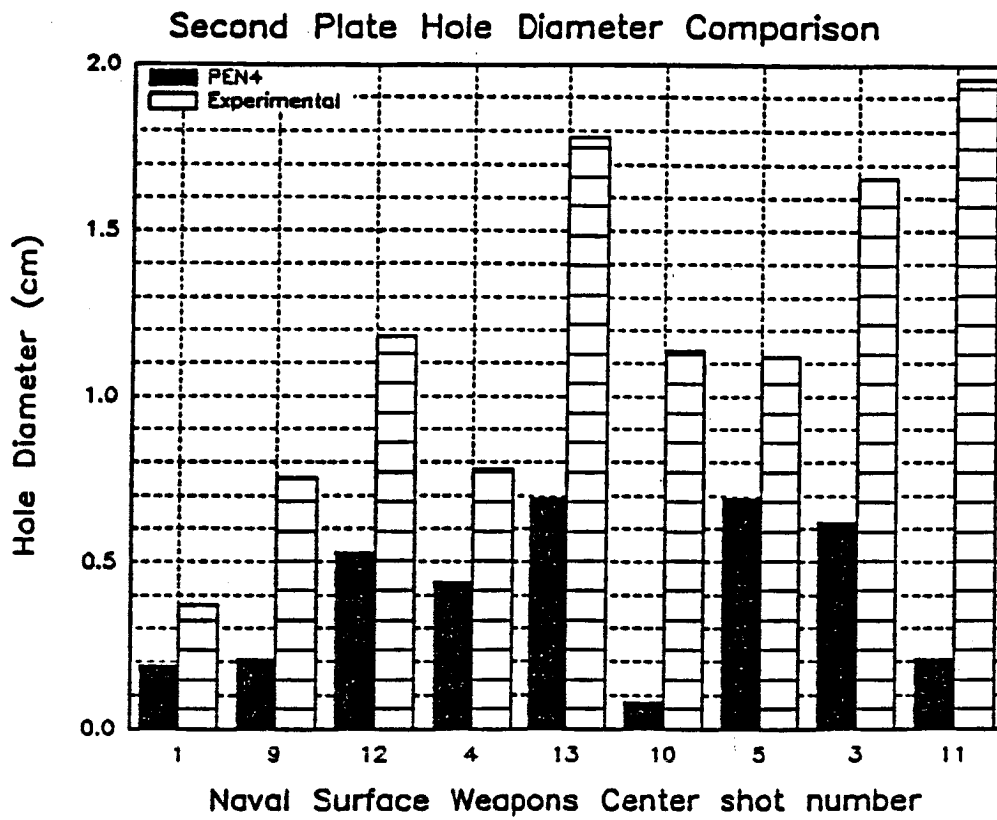


Figure 2-40 Comparison with NSWC TR 79-66 Plate Hole Diameter Data.

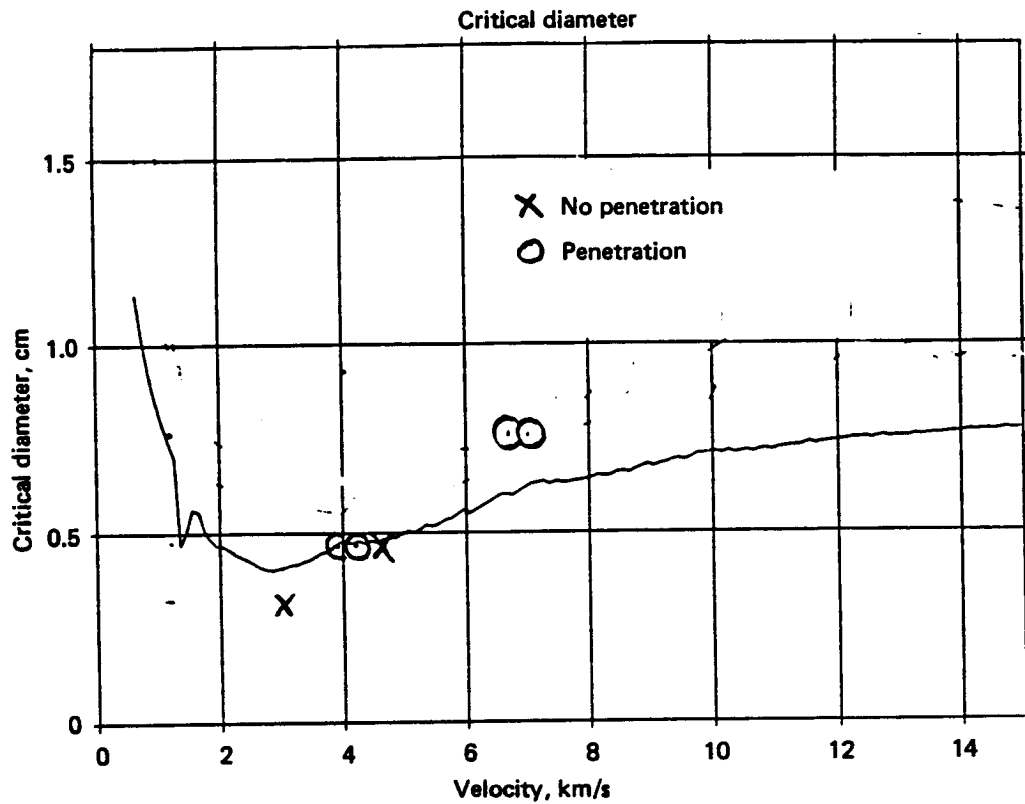


Figure 2-41 Comparison with SM-1 Critical Diameter Data.

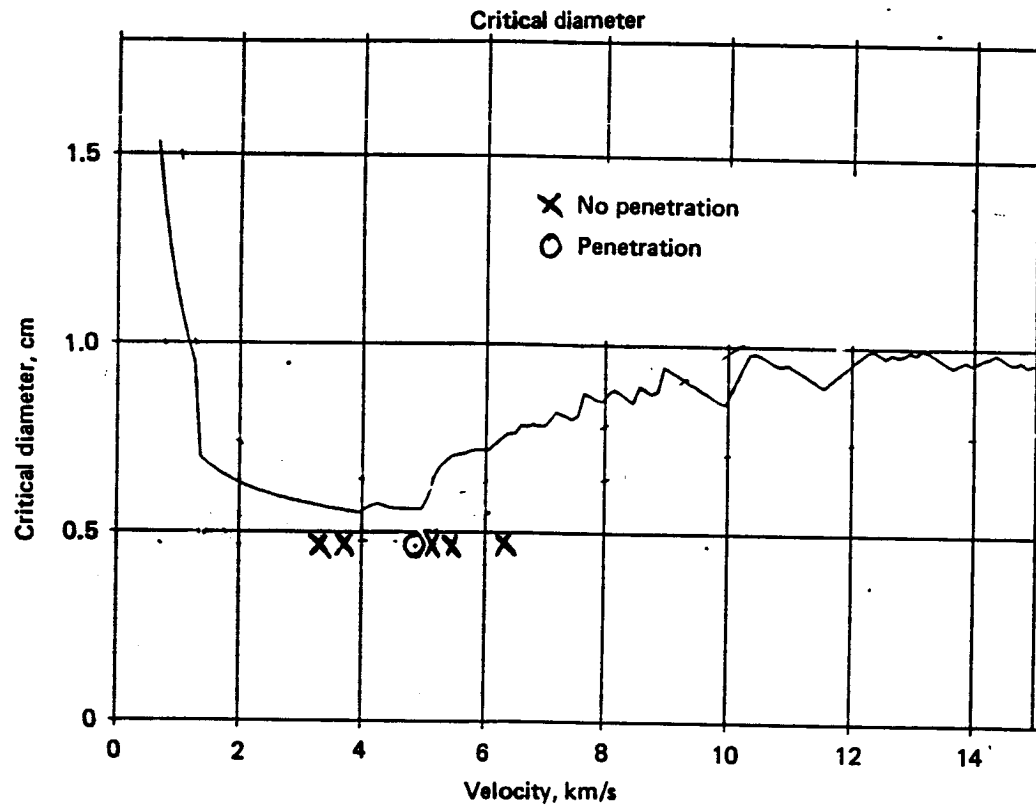


Figure 2-42 Comparison with NAS8-36426 45-degree obliquity critical diameter data

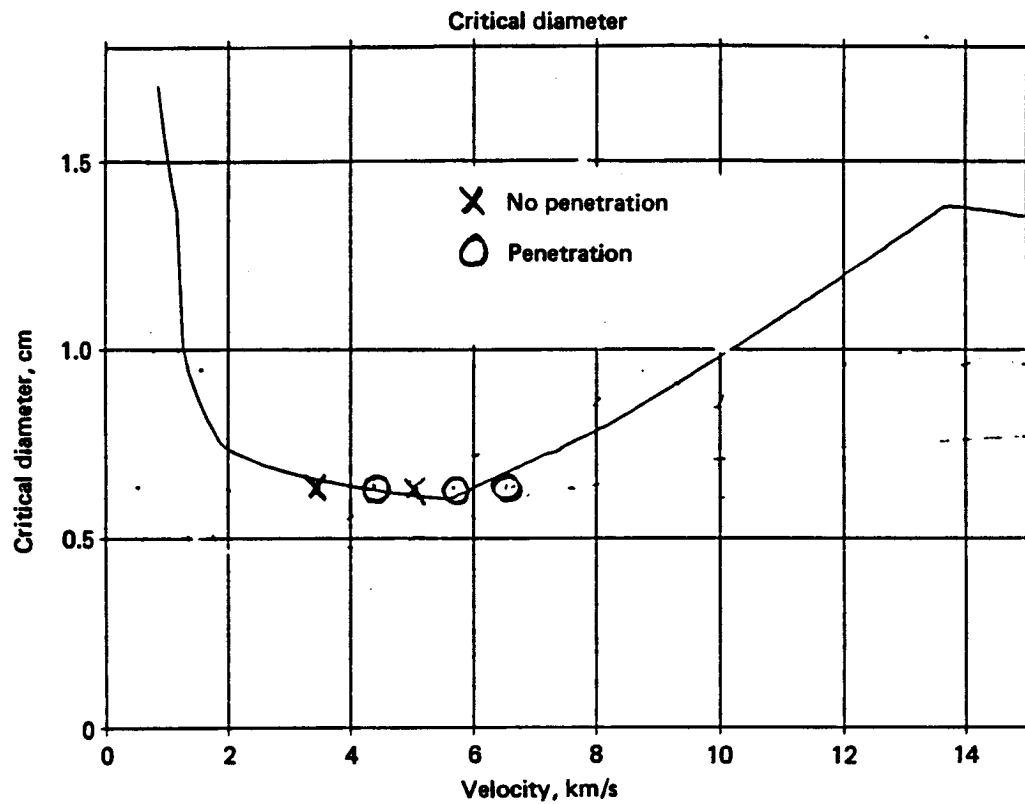


Figure 2-43 Comparison with NAS8-36426 60 degree obliquity critical diameter data

the theory for largest residual projectile fragment mass developed in section 2.3.5. This suggested that the craters were produced by fragments coming from the hole and not from the projectile. Inspection of the elliptical holes in the shield plates, caused by the oblique impacts showed them to be dished-in from the entrance side of the plate. Closer inspection of the edge of the hole itself showed it to be ragged. Both of these observations taken together suggest that substantial downwards motions are imparted to the edge of the hole by the oblique impact, leading in some cases to low speed fragments being torn loose. It is speculated that these downwards motions come from the projectile mushrooming along the shotline, and thus more effectively coupling a component of velocity normal to the shield at late times during the perforation. It is also speculated that since, the fragments come loose from the shield plate at later times, crack growth plays a significant role in the formation of the fragments and the crack growth is not very repeatable, leading the random velocity dependence of the perforating impacts measured for the tests plotted in figures 2-42 and 2-43.

It is concluded that, for oblique angles of impact, PEN4 does not accurately calculate the critical diameter required for perforating an aluminum plate shielded by a 6061-T6 shield. The numerous changes made under the NAS8-36426 contract to better model oblique impacts, though necessary, did not address what now appears to be the central feature of oblique impacts: large shield plate fragments.

The final comparison made was with the effect of plate spacing on the critical diameter curve. A parameter study was performed with PEN4 for a 63-mil shield and a 125-mil second plate separated by 1, 2, 4, 6, and 8 inches. The resulting critical diameter curves are plotted in figure 2-44. Some SM-1 data for a 6 inch plate spacing are also plotted in figure 2-44. The open circle denotes a shot resulting in perforation of the 2 plate array, while the x denotes a shot resulting in no perforation. Note that the PEN4 calculations under predict the critical diameter by 0.5 to 1 mm.

The under prediction of the 6-inch spacing critical diameter curve is not thought to be significant. Further adjusting of velocity exponent on the largest residual mass and the minimum hole diameter considered a perforation should improve the fit.

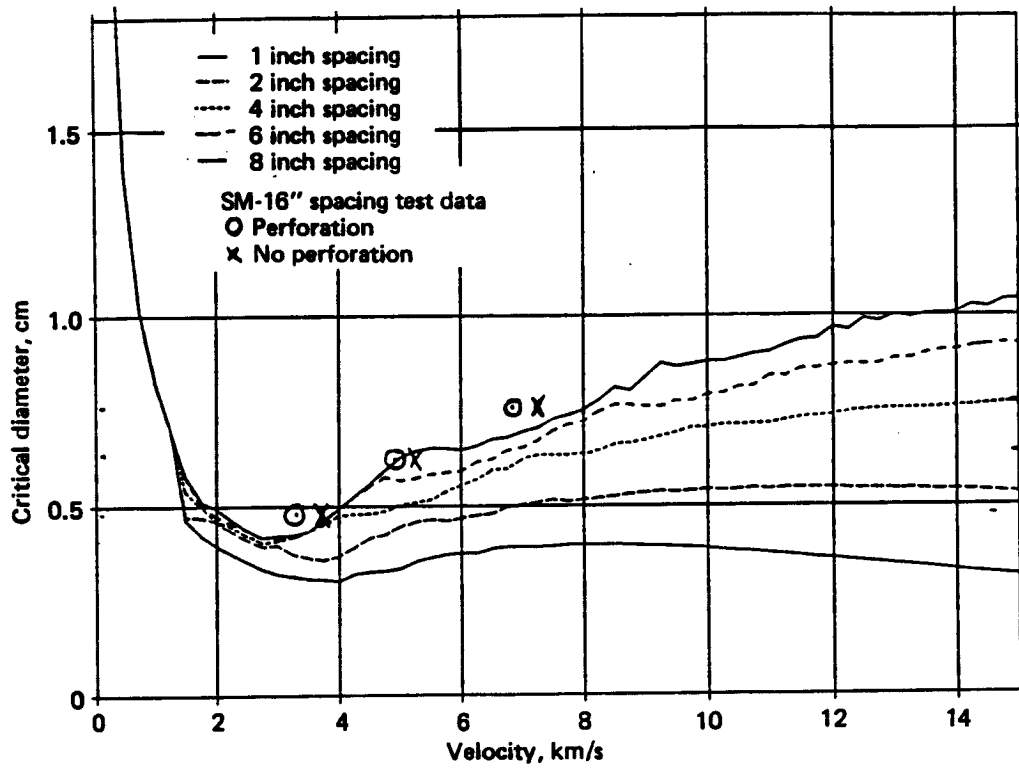


Figure 2-44 Comparison with SM-1 6 inch plate spacing critical diameter data.

5.0 RECOMMENDATIONS

The major improvement remaining to be made to PEN4 is the inclusion of a plate fragment distribution, distinct from the projectile fragment distribution, in the calculation of probability of multiple cratering.

The following tests and analysis will provide the necessary plate fragmentation data and modifications to PEN4:

1. Hypervelocity oblique impacts of aluminum projectiles onto single plate targets, with recovery of the plate fragments. Collection of steel projectile fragments has been successfully carried out at AEDC at impact velocities up to 4.5 km/s. Similar experimental techniques should allow collection of aluminum fragments at even larger impact velocities.
2. Hypervelocity oblique impacts of fully dense or foamed plastics onto single plate targets, with the recovery of the plate fragments. It seems unlikely that integral icy projectiles can be successfully launched at hypervelocities. However, it may prove possible to launch plastics, which will volatilize on impact reminiscent of ice. The small shock impedance of plastics will contribute to the fidelity of the simulation. The plate fragment data thus obtained will be used to form a credible icy meteoroid impact model.
3. Modification of PEN4 to include the plate fragment distribution in the calculation of the probability of multiple cratering. This task is a straightforward application of the mathematical techniques already developed for the projectile fragments.

Also of interest, but of lesser importance, is the following:

4. Determination of the effect of alloy and hardness on the projectile fragment masses. A theory has been developed in section 2.3.5 for the effect of material properties on largest residual fragment mass. If verified by experiment, this theory could be used for evaluating the relative effectiveness of penetration of different alloys of aluminum, necessary information for determining the uncertainty in the calculated critical diameter curves.

6.0 REFERENCES

1. NSWC TR 83-189. High Velocity Penetration Analysis. Naval Surface Weapons Center, Dahlgren, Virginia, May 1983.
2. D180-29230-1. PEN4 Version 8 Hypervelocity Impact Analysis. The Boeing Company, Seattle, Washington, 1 November 1986.
3. D180-28210-1. Fragment Fracture Study. The Boeing Company, Seattle, Washington. 15 June 1984.
4. D180-29153-1. Fragment Fracture Research. The Boeing Company, Seattle, Washington. November 1986.
5. Backman, M.E. and W. Goldsmith. The Mechanics of Penetration of Projectiles into Targets. Int. J. Engng. Sci., Vol. 16, pp. 1-99, 1978.
6. AFATL-TR-70-78. A Combined Theoretical and Experimental Investigation of Armor Penetration Mechanics. Air Force Armaments Laboratory, Eglin AFB, Florida. August 1970.
7. Zimmerschied, A.L., The Boeing Company, Seattle, Washington, (Private Communication).
8. Awerbuch, J. and S.R. Bodner. Int. J. Solids Struc. Vol. 10. p. 671 (1974).
9. ARBRL-TR-02188. The Particle Dynamics of Target Penetration. U.S. Army Ballistic Research Laboratory, Aberdeen Proving Ground, Maryland. September 1979.
10. THOR 41. A Comparison of the Performance of Fragments of Four Materials Impacting Various Plates. Ballistic Analysis Laboratory, John Hopkins University, Baltimore, Maryland. May 1959.
11. THOR 47. The Resistance of Various Metallic Materials to Perforation by Steel Fragments; Empirical Relationships for Fragment Residual Velocity and Residual Weight. Ballistic Analysis Laboratory. John Hopkins University, Baltimore, Maryland. April 1961.
12. 61 JTCG/ME-77-16. Penetration Equations Handbook. Technical Coordinating Group for Munition Effectiveness (Anti-Air) Aerial Target Vulnerability Subgroup. November 1977.
13. Arione, S.E. and M.D. Bjorkman. Scaling Flow Fields From the Impact of Thin Plates. Int. J. Impact Engng. vol. 5 (to be published)

14. NASA TN D-4568. Penetration Resistance of Double-Sheet Structures at Velocities to 8.8 km/s. National Aeronautics and Space Administration, Washington, D.C., May 1968.
15. SM-1 test data from Marshall Spaceflight Center, Huntsville, Alabama. (Unpublished).
16. AEDC Data Package: Von Karman Gas Dynamics Facility, Arnold Engineering Development Center, Arnold Air Force Station, Tennessee, Project No. V41S-20, SAMSO Fragment Impact Test. Test Period June 19 to September 1978. (Unpublished).
17. GM TR63-225. Investigation of Fundamental Mechanism of Damage to Thin Targets By Hypervelocity Projectiles. GM Defense Research Laboratories, Santa Barbara, California. September 1963.
18. Recht, R.F. and T.W. Ipson. Ballistic Perforation Dynamics. Journal of Applied Mechanics, Vol. 30, No. 3. pp 284-90. September 1963.
19. Fowles, G.R. Analytical Mechanics. 2nd edition, Holt, Rinehart and Winston, Inc. New York, New York. 1970.
20. Ipson, T.W. and R.F. Recht. Ballistic Penetration Resistance and Its Measurement, Experimental Mechanics, pp 249-257. July 1975.
21. NWC-TP-5844. Dynamics of the Oblique Impact and Ricochet of Nondeforming Spheres Against Thin Plates. Naval Weapons Center, China Lake, California. September 1976.
22. NWC-TP-6490. Experimental Data for Characterizing Perforating Impacts: Fragmentation Processes. Naval Weapons Center, China Lake, California. May 1985.
23. ARBRL-MR-03243. Ricochet and Penetration of Steel Spheres Impacting Aluminum Targets. Ballistic Research Laboratory, Aberdeen, Maryland. February 1983.
24. D180-28149-1. Fragment Penetration Physics Study. The Boeing Company, Seattle, Washington. 8 April 1985.
25. D180-29286-1. Aluminum Fragment Impact Test. The Boeing Company, Seattle, Washington. 1986.
26. Dickinson D., Naval Weapons Center, Dahlgren, Virginia (Private Communication).
27. Holsapple, K.A. and K.R. Housen. Scaling Laws for the Catastrophic Collisions of Asteroids (accepted for publication in Memorie della Societa Astromica Italiana).

28. Gault, D.E. and J.A. Wedekind. The Destruction of Tektites by Meteoroid Impact. J. Geophys. Res., Vol. 74, p. 6780-94. 1969.
29. Fujiwara, A., G. Kamimoto and A. Tsukamoto. Destruction of Basaltic Bodies by High Velocity Impact. Icarus, Vol. 31, pp. 277-88. 1977.
30. Grady, D.E. Local Inertial Effects in Dynamic Fragmentation. J. of Appl. Phys. Vol. 53, No. 1, pp. 322-5. 1982.
31. Weibull, W. Statistical Evaluation of Data From Fatigue and Creep Rupture Test. Fundamental Concepts and General Methods. WADC Tech. Rept. 59-400., Part I. 1959.
32. Grady, D.E. The Mechanics of Fracture Under High-rate Stress Loading., in, "Proc. W. Prager Symp. Mech. of Geomaterials: Rocks, Concrete, Soils." Int. U. of Theor. Appl. Mechanics. Northwestern University, Evanston, Illinois. 1983.
33. Grady, D.E. and M.E. Kipp. Statistical Size Distribution in Random Single Fracture. 1983.
34. NSWC TR 82-123. High Velocity Multiple Plate Penetration Model. Naval Surface Weapons Center, Dahlgren, Virginia. February 1982.
35. Holsapple, K.A. and R. M. Schmidt, "Point Source Solutions and Coupling Parameters in Cratering Mechanics" (submitted to Journal of Geophysical Research).
36. Small crater impact test report document.
37. Herrmann, W. and A.H. Jones. Survey of Hypervelocity Impact Information. ASRL Report No. 99-1. Lincoln Laboratories, Massachusetts Institute of Technology, Cambridge, Massachusetts. September 1961. AD 267 289.
38. NSWC TR 79-66. Investigation of High-Velocity Fragments Impacting Plate Arrays. Naval Surface Weapons Center, Dahlgren, Virginia. March 1979.
- B-1 Zukas, J.A., T. Nicholas, H.F. Swift, L.B. Greszczuk, and D.R. Curran. "Impact Dynamics," John Wiley & Sons, New York, NY, 1982 p. 317.
- C-1 Grady, D.E. Steady Wave Risetime and Spall Measurements on Uranium (3-15 GPa) in, "Metallurgical Applications of Shock-Wave and High-Strain-Rate Phenomena," ed. by, L.E. Murr, K. Staudhammer, and M.A. Myers. Marcel Dekker, Inc., New York, New York. 1986

- C-2 AFWAL-TR-83-4144. Damage Tolerant Design Handbook. Air Force Wright Aeronautical Laboratories/Materials Laboratory, Wright Patterson AFB, Ohio. 1983.
- C-3 McClintock, F.A. and A. S. Argon. "Mechanical Behaviour of Materials." Addison-Wesley Co., Reading, Massachusetts. 1966.
- C-4 Campbel, J.E., W.W. Gerberich and J.H. Underwood. "Application of Fracture Mechanics for Selection of Metallic Structural Materials." American Society for Metals, Metals Park, Ohio, 1984.

APPENDIX A

OBLIQUE IMPACTS DATA SEARCH

A data search was made for oblique impact data using two personal computer data bases. The first data base was constructed at Boeing from SM-1 and NAS8-36426 data. The second data base was produced by Kaman Nuclear Sciences under contract to the U.S. Army Strategic Defense Command (USASDC), Ref. A-1. Over 600 documents were found in the USASDC contracted bibliographic search, which were then cataloged and entered into the data base.

The data bases were only searched for data that came from the impact of a projectile on a single plate; i.e., hole diameter, crater dimensions, and projectile and target fragment mass data. These data are directly applicable to the development of oblique impact relations for the various routines within PEN4. Multiple plate ballistic limit velocity or multiple plate ballistic limit thickness data (which are the vast majority of what was measured) were ignored. Enough data of that ilk have been collected under NAS8-36426 and SM-1 to validate the PEN4 results. Furthermore, in many cases, the targets were of complex shapes and composed of multiple materials, making any comparison to PEN4, which is designed to handle only two projectile materials and one target material, problematical.

No significant data were found in these two data bases quantifying the masses of projectile or target fragments produced by oblique impacts. Hence, no modifications of the largest residual fragment mass and the residual fragment mass distributions were possible from this data search.

No significant amounts of crater volumes from oblique impacts of uniform targets data were found in either of these two data bases. Hence, the older reference, Ref. 37, which did not have much data above 5 km/s impact velocity, was the sole source of crater dimensions from oblique impacts data.

What were found in the two data bases were data for the hole diameter produced in the shield plate from oblique impacts of projectiles. Hence what follows is a discussion of the oblique impact hole data found and the fits made to them.

A number of oblique hole diameter data from the NAS8-36426 testing were found. Figures A-1 and A-2 show the fits to four of those oblique impact shots. It was decided to fit the data with a function that peaked near 60 degrees obliquity, mostly on the basis of test data found in the USASDC data base. The function chosen was, which peaks near 60 degrees.

$$D_H = D_H(\theta=0) [1 - \exp(-(85-\theta)/9.5)] \quad (A-1)$$

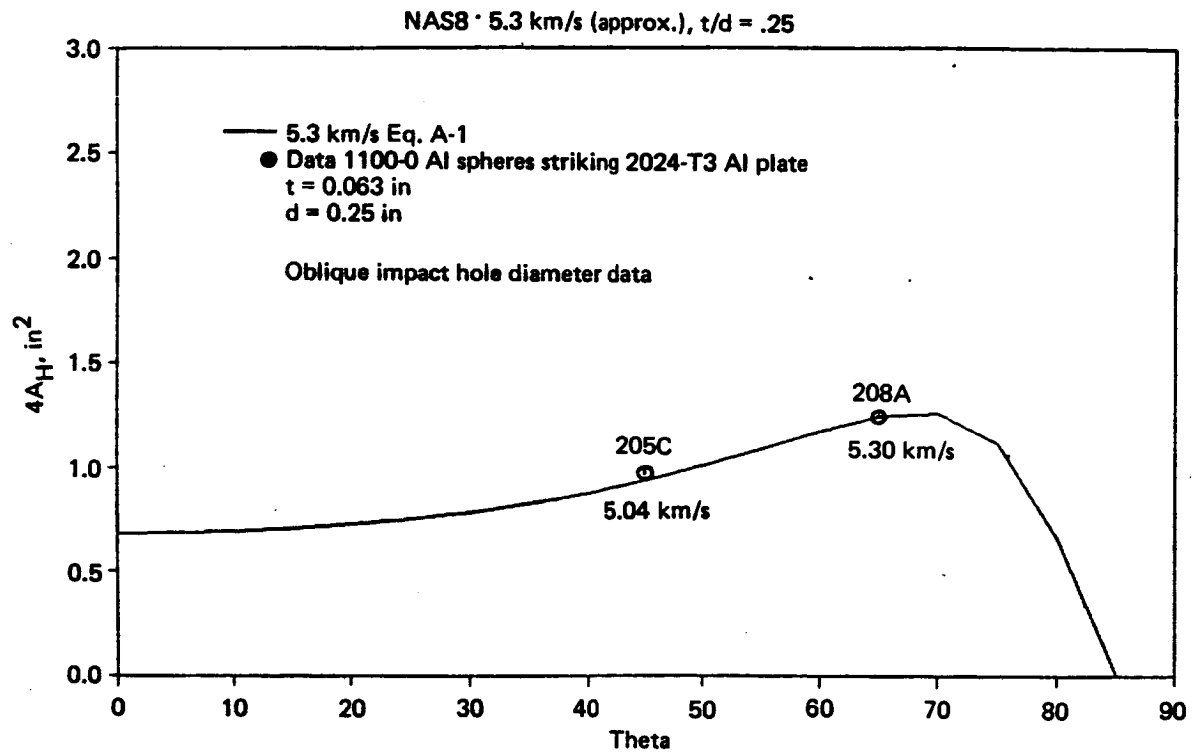


Figure A-1 Oblique Impact Hole Diameter Data

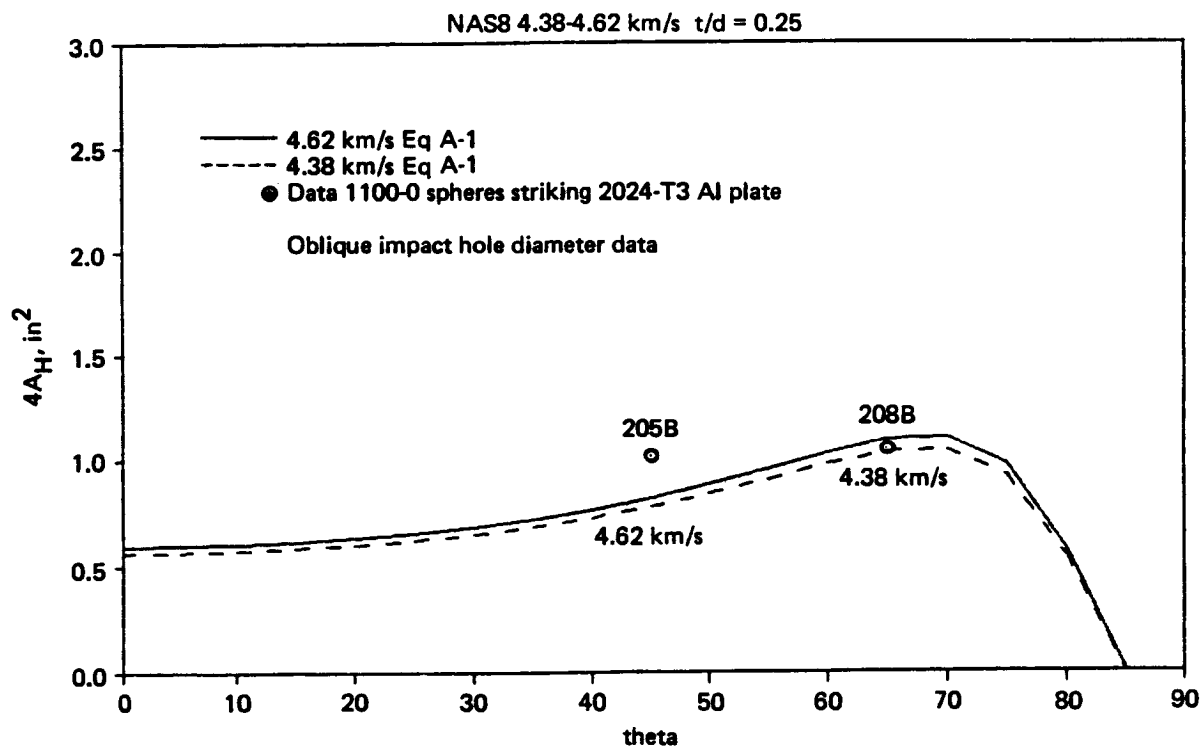


Figure A-2 Oblique Impact Test Data

The 5.3 km/s impact velocity data plotted in figure A-1 are fitted well by Eq. A-1 which is plotted as the solid line, while the smaller impact velocity 4.38 and 4.62 km/s data plotted in figure A-2 are not fitted as well by Eq. A-1, which is plotted as the solid line for 4.62 km/s impact velocity and as the broken line for 4.28 km/s impact velocity.

Sixty-six shots were found in the USASDC data base which met the following conditions: 1) a homogeneous spherical projectile, and 2) an oblique impact of a flat target plate. Thirty five of the 66 shots found in the data base were shot into multiple layer targets (e.g. the targets were single plates composed of ablative material glued to an aluminum substrate.) Most of the effort was expended in fitting the single layer targets and not the multiple layer targets.

A comparison of Eq. A-1 with 2 data points from the USASDC data base is plotted in figure A-3. The projectiles were 2017 aluminum spheres and the targets were 2024-T3 aluminum plates. The plate thickness, projectile diameter, and impact velocity are labeled on the figure.

The fit is not as good as the fit to the NAS8-36426 5.63 km/s impact velocity data and is indicative of the general applicability of Eq. A-1.

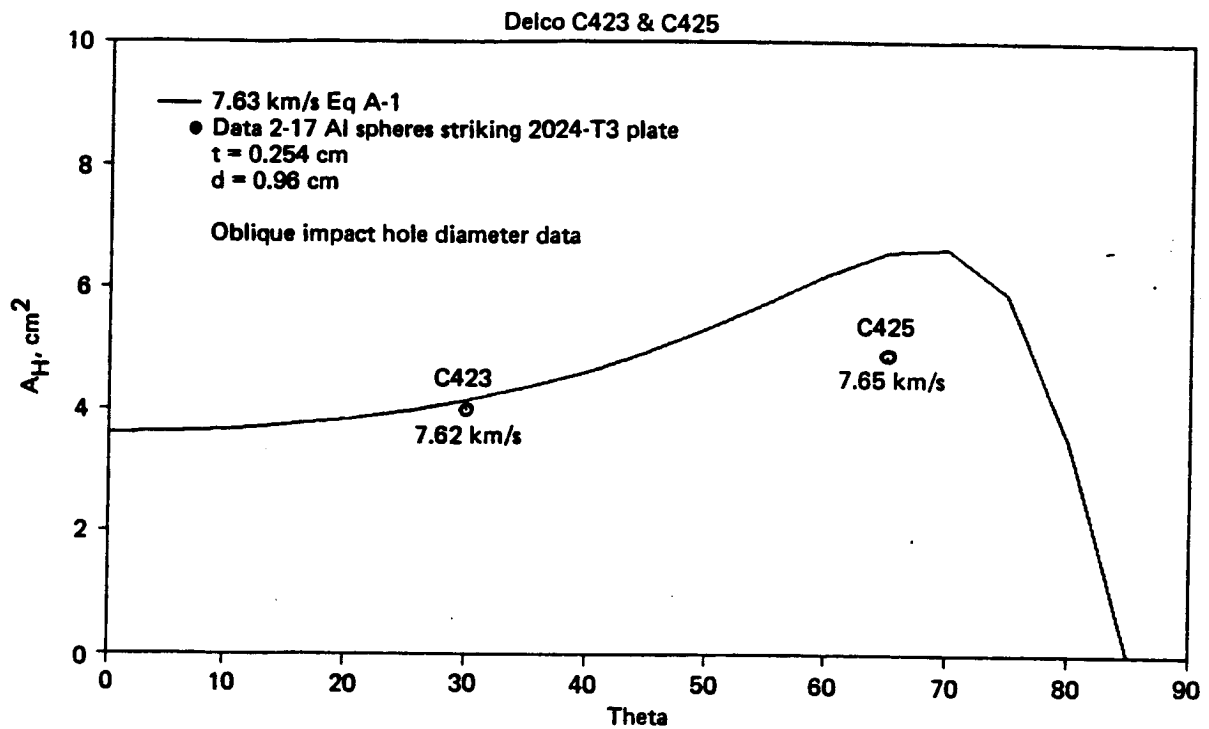


Figure A-3 Oblique Impact Hole Diameter Data

APPENDIX B

EFFECT OF RATE DEPENDENT YIELD ON BALLISTIC LIMIT VELOCITY
SIZE DEPENDENCE

Over the past thirty years a large body of rate dependent yield test data has been obtained. Nicholas (Ref. B-1) has summarized some of these data and plotted them as figure B-1. The y-axis is the strain rate exponent n defined for Eq. 3 and used in Eq. 5. This can be shown as follows.

Rate dependent yield Y was assumed to be proportional to a power of the strain rate $d\epsilon/dt$. (If the rate dependent yield mechanism is not actually a power-law, as in creep, it can be at least approximated by a power-law over some limited range of strain rates.) This was expressed mathematically as Eq. 3, which is reproduced below as Eq. B-1,

$$Y = k (d\epsilon/dt)^n. \quad (B-1)$$

Suppose two measurements of strain rate dependent yield strength have been made, one at a small strain rate $(d\epsilon/dt)_s$, called the static strength Y_s , and the other at a large strain $(d\epsilon/dt)_d$, rate called the dynamic strength Y_d . The average power law exponent relating the measured yield strengths to the applied strain rates will be called n , and will satisfy the equations,

$$Y_s = k (d\epsilon/dt)_s^n. \quad (B-2)$$

$$Y_d = k (d\epsilon/dt)_d^n. \quad (B-3)$$

To solve for the exponent n using the two measured values of strength, divide Eq. B-3 by Eq. B-2 and obtain,

$$Y_d/Y_s = [(d\epsilon/dt)_d/(d\epsilon/dt)_s]^n. \quad (B-4)$$

Note that for Y_d approximately equal to Y_s the left-hand side of Eq. B-4 may be approximated by,

$$Y_d/Y_s - 1 + (Y_d/Y_s - 1) = \exp(Y_d/Y_s - 1). \quad (B-5)$$

Substituting Eq. B-5 into Eq. B-4 and taking the natural logarithm of both sides gives,

$$Y_d/Y_s - 1 = n \ln[(d\epsilon/dt)_d/(d\epsilon/dt)_s] \quad (B-6)$$

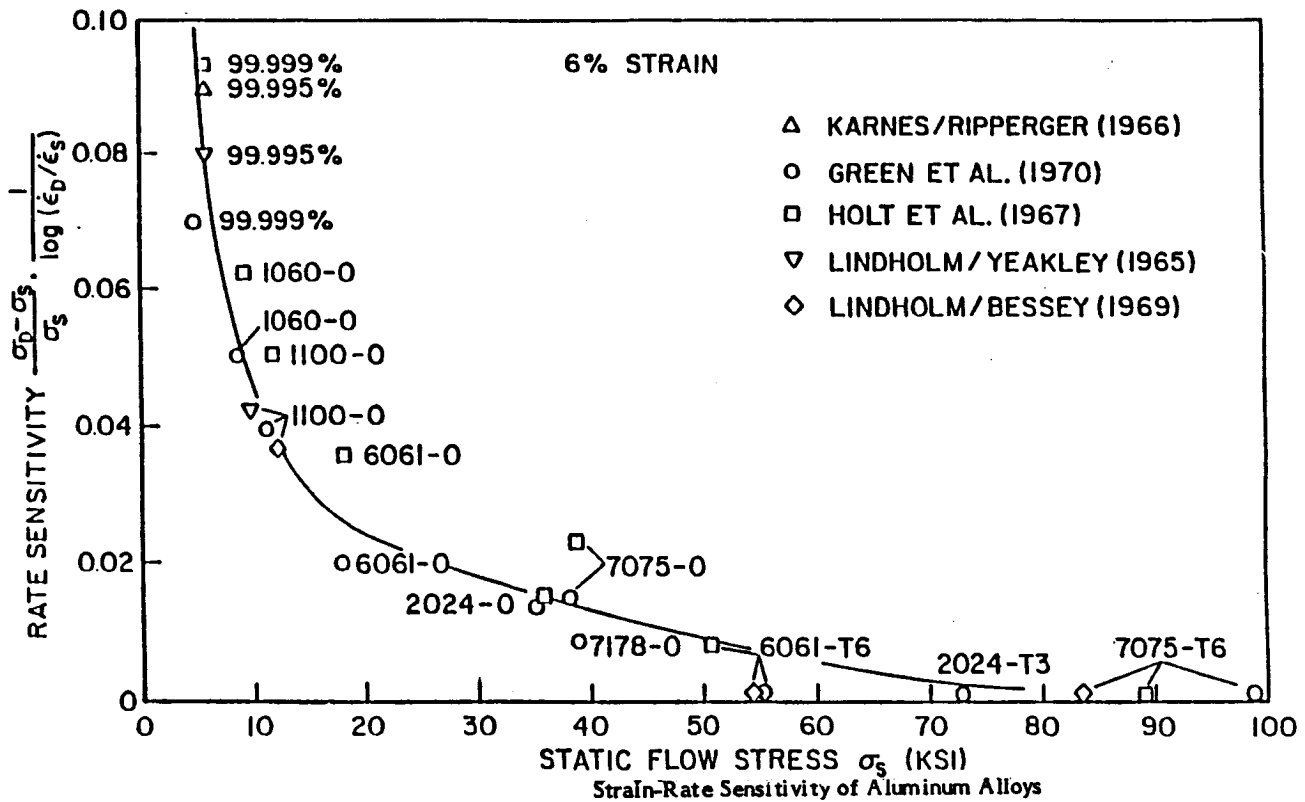


Figure B-1.

Rearranging the terms of Eq. B-6 gives,

$$n = (Y_d - Y_s) / Y_s \cdot 1 / \ln[(d\epsilon/dt)_d / (d\epsilon/dt)_s], \quad (B-7)$$

which the desired result.

The 2024-T3 point is plotted at a static yield strength of 72 ksi and using the curve fitted through the data gives,

$$n = 0.002. \quad (\text{for 2024-T3}) \quad (B-8)$$

Note that the scatter in the data for the materials for which repeated measurements have been made is around 0.01, hence values for n between zero and 0.01 should probably be considered, which are the values quoted in section 2.3.1.

APPENDIX C

EFFECT OF FRACTURE SURFACE ENERGY ON
LARGEST RESIDUAL FRAGMENT MASS

Fragmentation results from the nucleation and growth of cracks. The following is a conceptually simple model of fragmentation that probably oversimplifies what actually occurs; however, it is easy to derive and can be readily tested.

The PEN4 model for largest residual fragment mass is a generalization of an analysis performed by Grady in Ref. 30. The analysis given below from Eq. C-1 to Eq. C-7 is a reproduction of the analysis for spherical fluid projectiles performed by Grady in Ref. 30. His results are generalized in Eq. C-8 to C-10 to the case of metallic projectiles striking metallic plates using the analysis presented in section 2.3.5.2 of this document. At the end of this appendix Eq. C-10 is applied to test data and the fit parameters are determined for mild steel projectiles and 2024-T3 aluminum projectiles striking aluminum plates.

C.1 GRADY'S MODEL FOR FRAGMENT SIZE FROM THE RADIAL EXPANSION OF
SPHERICAL FLUID PROJECTILES.

The PEN 4 model for largest residual fragment size starts from an analysis of fluid projectile fragmentation performed by Grady in Ref. 30. There he argued that the kinetic energy associated with the expansion of the projectile (in our case the spherical expansion would have to come from the motions induced in the projectile by the collision with the target plate) is responsible for the fracturing forces, and that the fracture surface energy associated with forming the fracture surfaces alone resists the fragmentation process.

The the above intuitive argument was expressed mathematically by Grady in Ref. 30 for the special case of radial expansion of a fluid drop projectile. For the fluid drop projectile case the total energy per unit volume of the projectile $E(A)$ is,

$$E(A) = 3 (d\delta/dt)^2 / (10 \delta A^2) + \gamma A, \quad (C-1)$$

where the first term on the right-hand side of Eq. C-1 is the radial kinetic energy, and the second term on the right-hand side is the surface energy associated with forming fragments with surface area to volume ratio A . The parameter δ is the projectile density, $d\delta/dt$ is the time rate of change of the density from the radial expansion of the projectile, and γ is the surface energy associated with forming the fragment. The volumetric strain

rate de/dt associated with radial expansion is

$$de/dt = (d\delta/dt)/(3\delta). \quad (C-2)$$

Substituting Eq. C-2 into Eq. C-1 gives,

$$E(A) = 2.7 \delta (de/dt)^2/A^2 + \gamma A. \quad (C-3)$$

Grady assumed that during the fragmentation process the forces brought about will seek to minimize the energy in Eq. C-1 with respect to the fracture surface area per fragment volume A . The minimum of Eq. C-1 occurs when $dE/dA = 0$, or,

$$A = (5.4 \delta/\gamma)^{1/3} (de/dt)^{2/3}. \quad (C-4)$$

The surface area to volume ratio, A , for spherical fragments is,

$$d = 6/A, \quad (C-5)$$

where d is the fragment diameter. Substituting Eq. C-5 into Eq. C-4 gives,

$$d = 3.43 (\gamma/\delta)^{1/3} (de/dt)^{-2/3}. \quad (C-6)$$

Equation C-6 can be solved for the fragment mass, m , by cubing both sides of Eq. C-6 and multiplying both sides by the fragment density δ ,

$$m = 39.4 \gamma (de/dt)^{-2}. \quad (C-7)$$

In Ref. 30 Eq. C-6 was shown to closely fit the mean fragment diameter data from flat plate spall of oil shale experiments. The strain rate in the flat plate target material was calculated using the approximation that the free surface velocity divided by the specimen thickness gives the strain rate. Note that for symmetric impact, the free surface velocity is approximately equal to twice the impact velocity. When this result is substituted into Eq. C-7 the inverse square dependence on impact velocity noted in figure 2-16 for mild steel cube projectiles is obtained for the oil shale experiments, a result that Grady did not point out.

Also in Ref. 30, Eq. C-7 was shown to apply to the mean diameter of fragments from exploding brittle steel cylindrical cases. This result was shown in figure 2-18 of this report. The exploded cases all used the same explosive, hence loaded the cases all at the same strain rate. Thus these experiments are tests on the fracture surface energy parameter in Eq. C-7. In Ref. 30 this important test on the choice of material parameters validated the choice of fracture surface energy for brittle steels.

Equation C-7 also appears to apply to ductile materials, however. In Ref. C-1 Grady showed that Eq. C-7 adequately fitted spall data from flat plate impacts of ductile unalloyed D-38 uranium metal plates. The question arises

on how to measure a material parameter associated with brittle materials (such as the fracture toughness) when the material of interest is ductile; however, when available Grady's model appears applicable.

C-2 GENERALIZATION OF GRADY'S MODEL TO THE IMPACT OF METAL PROJECTILES ON METALLIC PLATES.

The essential result of Grady's Eq. C-7 is that the fragment mass is only dependent on one material parameter; the fracture surface energy γ .

The assertion that the fracture surface energy is the only material parameter governing fragmentation is the core of Grady's analysis, even though it was never explicitly stated in his Ref. 30. This result is also consistent with the observation made in section 2.3.5.2 that there is only one material parameter governing fragmentation. Thus, the analysis leading up to Eq. 44 in section 2.3.5.2 can be used to determine the largest residual fragment mass for mild steel and aluminum projectiles by equating the dimensions of the fragmentation material parameter S in Eq. 44 with the dimensions of the fracture surface energy γ . This requires that the exponent a on S equal 1 and the exponent b equal 0. Substituting these exponents into Eq. 44 gives,

$$m_r V^2 / (d^2 \gamma) = f(t/d, Z_p/Z_t). \quad (C-8)$$

It can be shown that the surface energy γ is related to the critical stress intensity factor K_{1c} required to just start the crack propagating. The relation (see Ref. C-2) is,

$$\gamma = K_{1c}^2 / (\delta c^2). \quad (C-9)$$

Substituting Eq. C-9 into Eq. C-8 gives,

$$m_r/m_s = [K_{1c}/(\delta c)]^2 V^{-2} d^{-1} f(t/d, Z_p/Z_t). \quad (C-10)$$

Equation C-10 contains 3 results that can be tested by experiment:

1. m_r/m_s V^{-2} at fixed d , t/d and material properties
2. m_r/m_s d^{-1} at fixed V , t/d and material properties
3. m_r/m_s K_{1c}^2 at fixed V , d , t/d and target material

C.3 THE FIT OF EQUATION C-10 TO TEST DATA

Equation C-10 has only been compared with some recent NSWC/D tests performed at DRI Ref. 26. Some 200 test firings of mostly R_p90 1018 steel cubes fired against 2024-T3 aluminum plates were performed. The cube sizes were 1/4, 3/8, and 1/2 inches, and the t/d 's were 0.065, 0.1, 0.2, 0.4, and 0.8. A few tests were also performed with R_c30 and R_c40 4340 steel cubes against aluminum plates.

The $t/d = 0.065$ data from Ref. 26 are plotted in figure C-1, the $t/d = 0.1$ data are plotted in figure C-2, the $t/d = 0.2$ data are plotted in figure C-3, the $t/d = 0.4$ data are plotted in figure C-4, and the $t/d = 0.8$ data are plotted in figure C-5. Two curves have been drawn through each set of t/d and d data. At impact velocities well above the fragmentation threshold velocity, the largest residual mass is formed by the power-law fragmentation mechanism, m_r is proportional to the inverse square of impact velocity, and Eq. C-10 holds. A greater dependence on impact velocity is evident for impacts near the fragmentation threshold which is thought to result from projectile spallation.

The curves were fitted to the data freehand. Lines of slope -2 were drawn through the data plotted in figures C-1, C-2, C-3, C-4 and C-5 and the spacing between the lines adjusted to give inverse dependence on size. The curves pass reasonably well through the data. This procedure was most problematic with the $t/d = 0.8$ data plotted in figure C-5 where the $m_s = 16$ g data appear to be above the two smaller sizes. These data were fitted with a spall relation to force the desired dependence on d at larger impact velocities.

The functional dependence of m_r on t/d , called $f(t/d)$ in Eq. C-10, is not determined by the dimensional analysis leading to Eq. C-10 and thus must be determined from fits to the data. Fitting the data was accomplished by reading from figures C-1, C-2, C-3, C-4, and C-5 the value for m_r/m_s at $m_s = 2.0$ g and $V = 2$ km/s and plotting them in figure C-6.

Since the curve for $f(t/d)$ plotted in figure C-6 is an empirical fit to data taken for $0.065 < t/d < 0.8$, a decision must be made on what value m_r/m_s will have for t/d 's outside the test data range. For simplicity m_r/m_s for $t/d < 0.1$ was chosen to be constant and equal to m_r/m_s at $t/d = 0.1$ and m_r/m_s at $t/d > 0.8$ was chosen to be constant and equal to m_r/m_s at $t/d = 0.8$.

The constants for Eq. C-10 for the NSWC/D test data must be determined before $f(t/d)$ can be calculated from figure C-6. Unfortunately, values of K_{lc} for $R_c 40$ 4340 steel cubes and $R_p 90$ 1018 steel cubes are not available so values of K_{lc} were estimated for those materials not reported in the literature.

The fracture toughness values for $R_c 45$, 50, and 60 4340 steel listed in Table C-1 were taken from Ref. C-2.

The values of K_{lc} for $R_c 30$ and 40 4340 steel listed in Table C-1 were estimated by assuming them the same as the values for $R_c 45$ 4340 steel. This choice was made to make Eq. C-10 consistent with the m_r data plotted in figure C-7. The m_r data plotted in figure C-7 indicate that $R_c 30$ and 40 4340 steel cubes produce largest residual fragments with about the same mass. If this is to be consistent with Eq. C-10, then $R_c 30$ and 40 4340 steel must

NSWC/D steel cube data

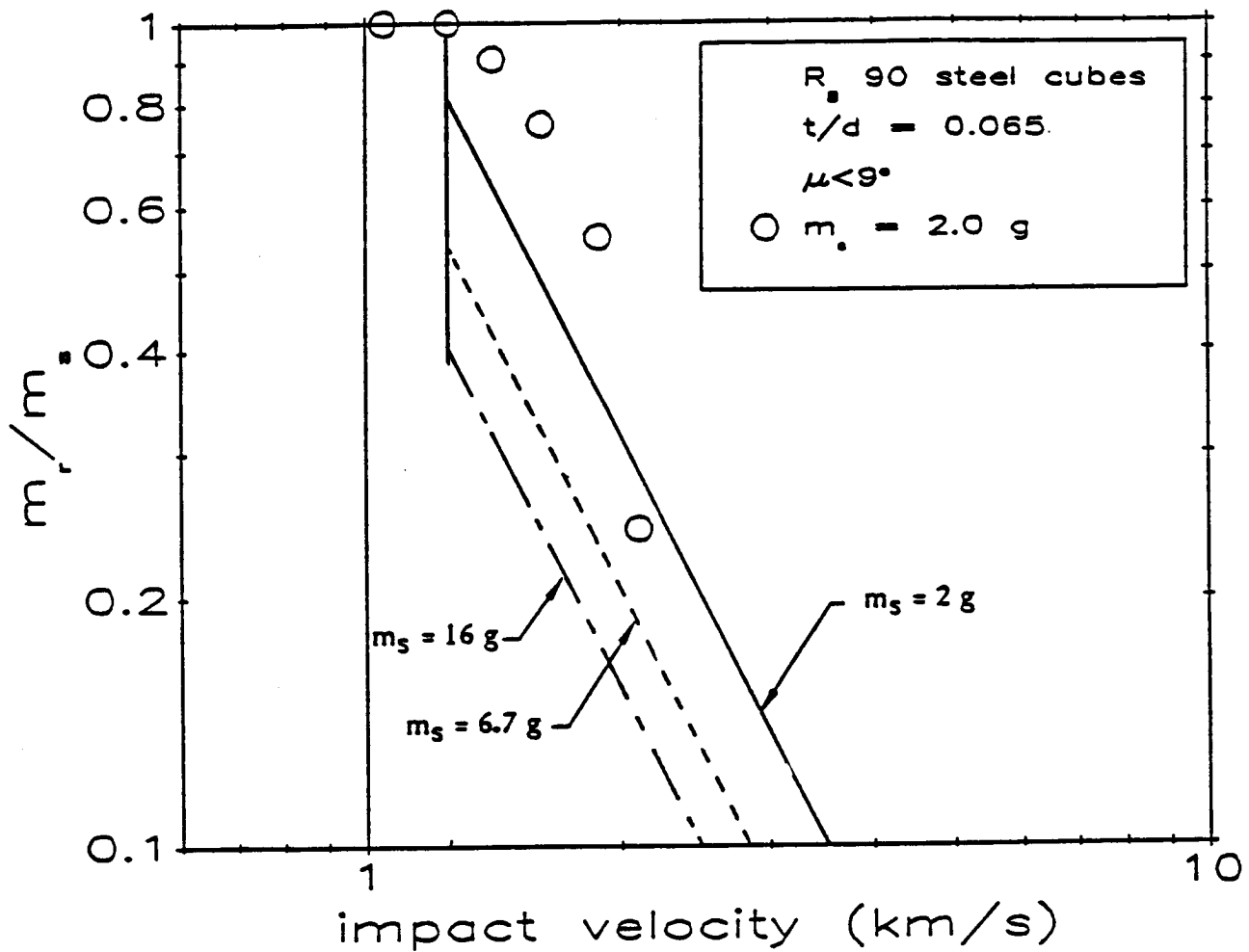


Figure C-1 Largest residual fragment mass as a function of impact velocity for Rb90 1018 steel cubes striking 2024-T3 aluminum plate, $t/d = 0.065$

NSWC/D steel cube data

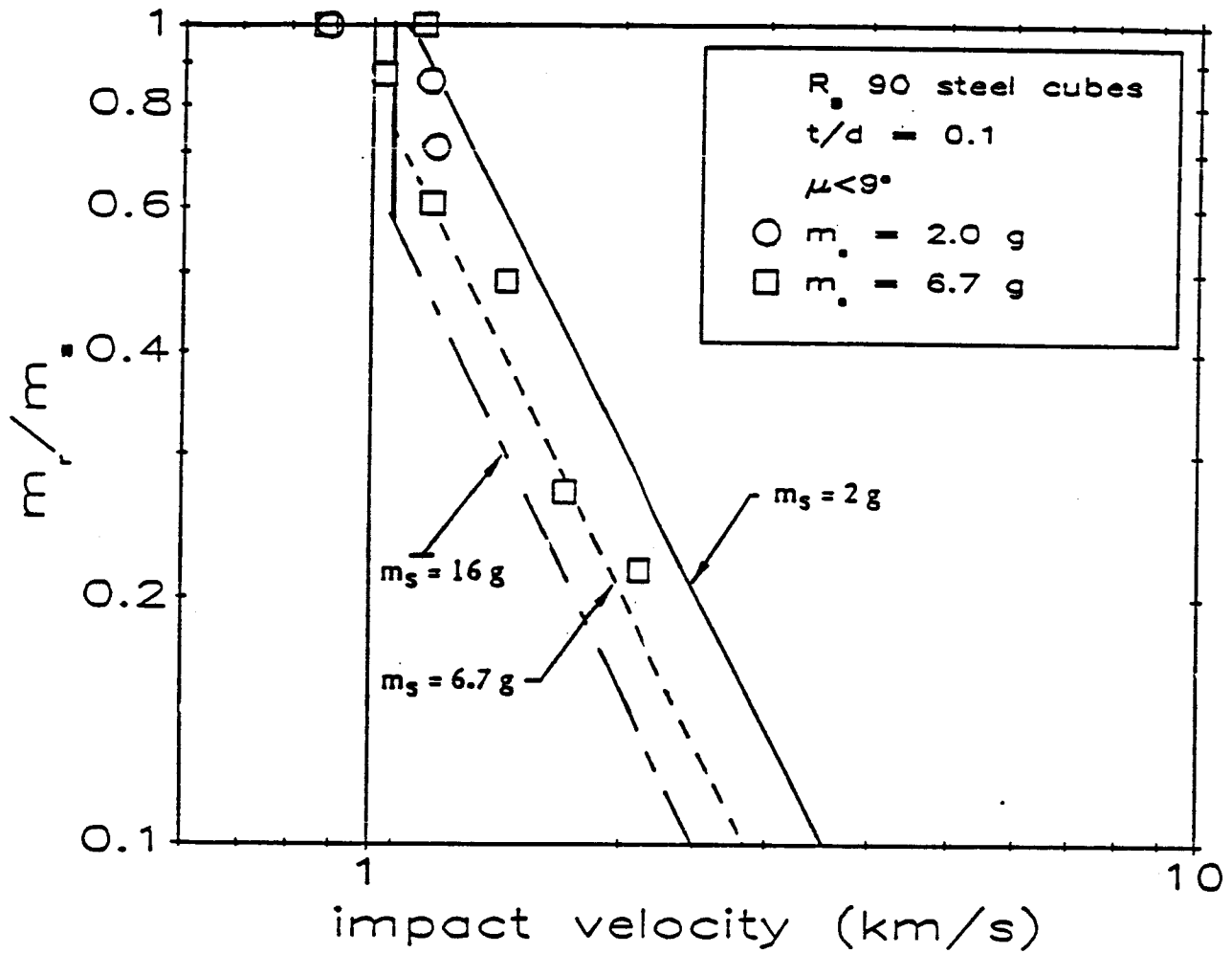


Figure C-2 Largest residual fragment mass as a function of impact velocity for Rb90 1018 steel cubes striking 2024-T3 aluminum plate, $t/d = 0.1$

NSWC/D steel cube data

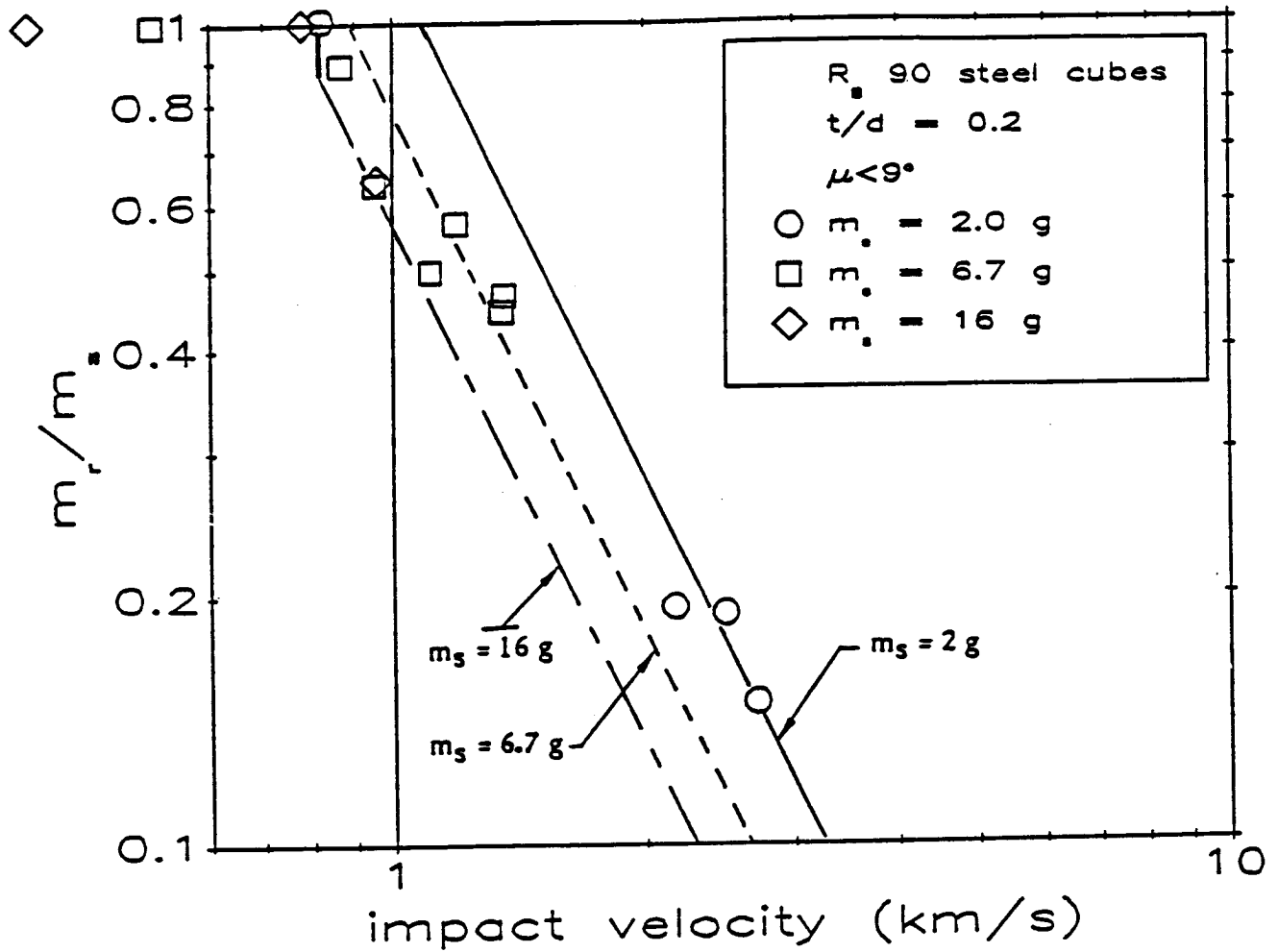


Figure C-3 Largest residual fragment mass as a function of impact velocity for Rb90 1018 steel cubes striking 2024-T3 aluminum plate, $t/d = 0.2$

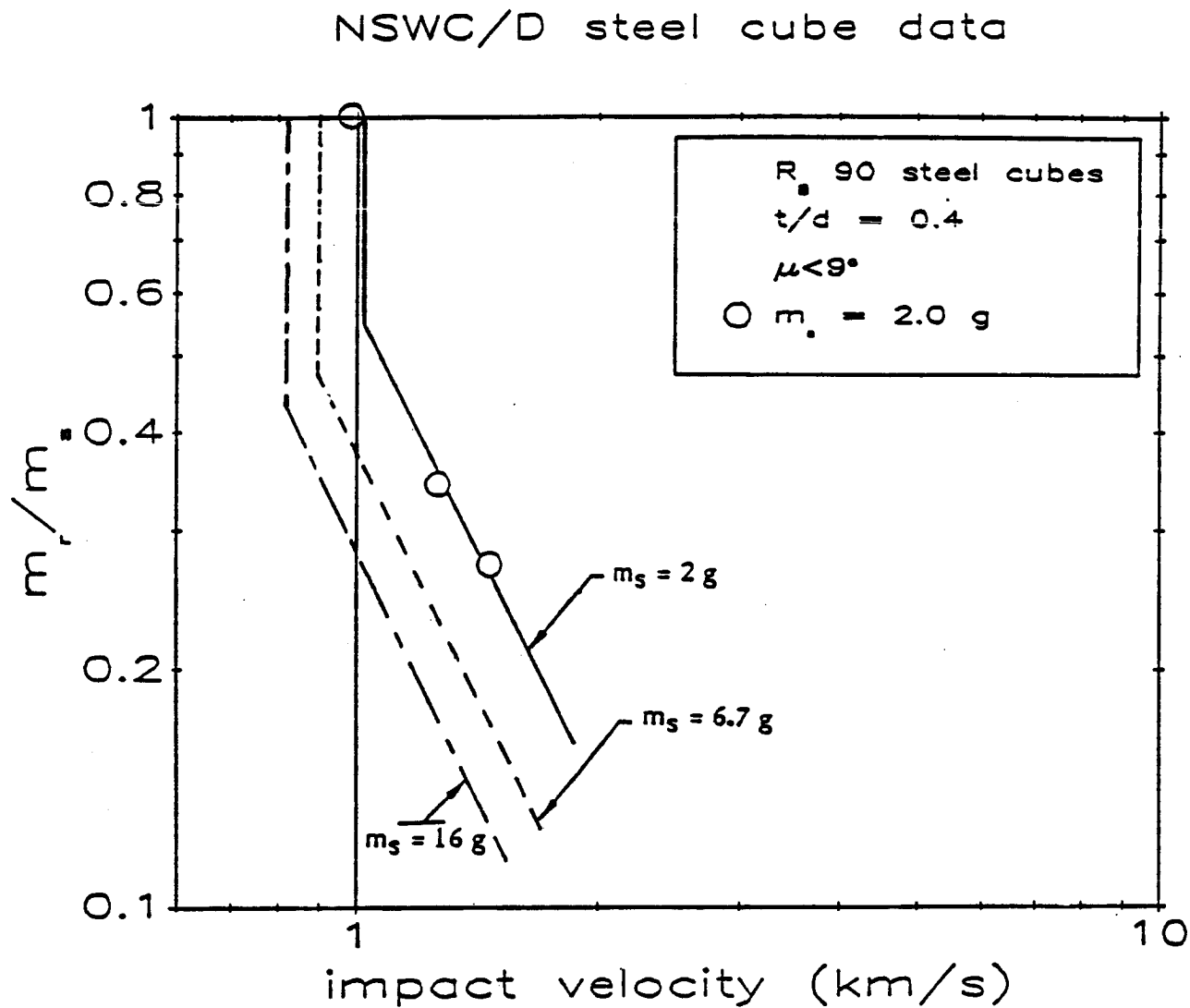


Figure C-4 Largest residual fragment mass as a function of impact velocity for Rb90 1018 steel cubes striking 2024-T3 aluminum plate, $t/d = 0.4$

NSWC/D steel cube data

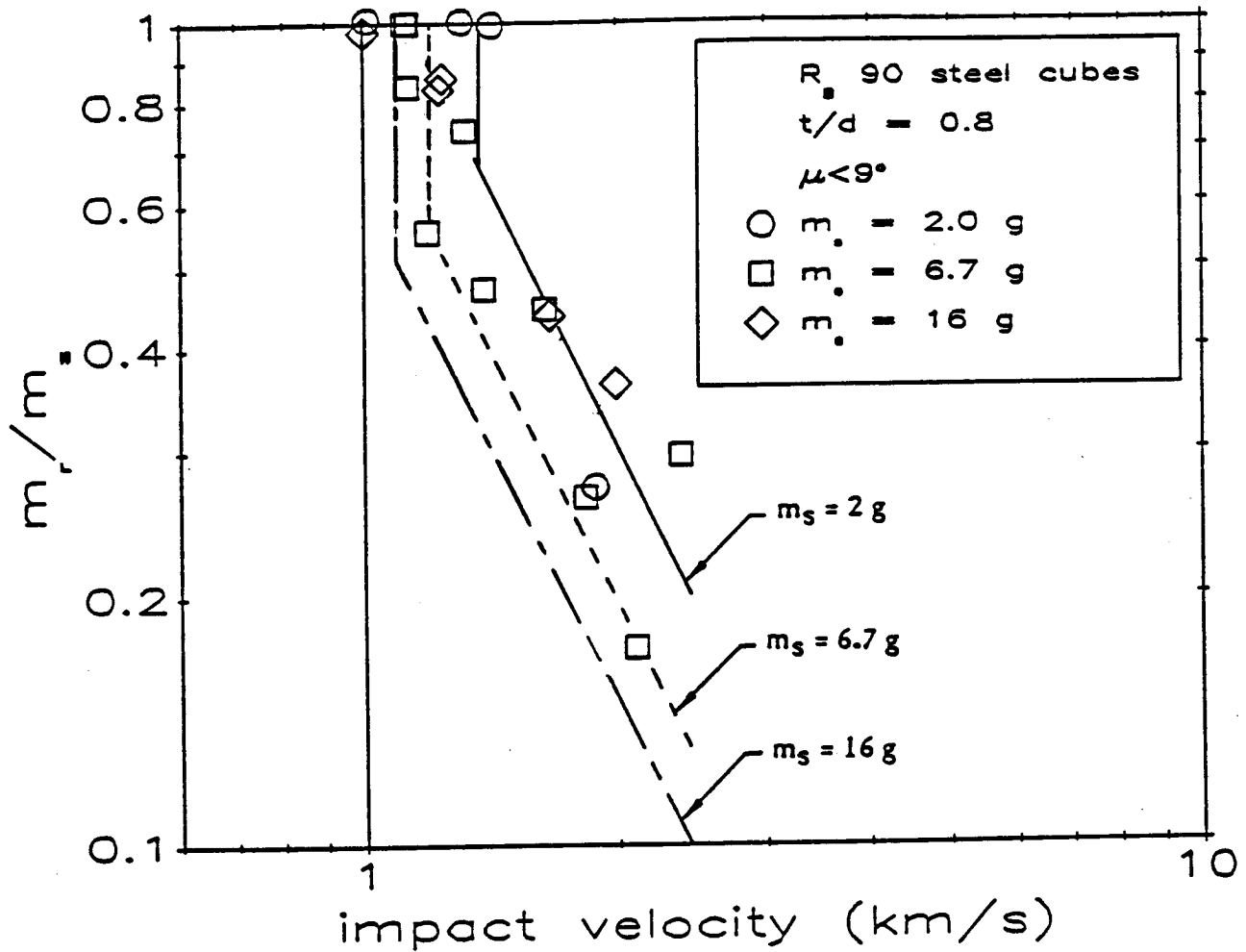


Figure C-5 Largest residual fragment mass as a function of impact velocity for Rb90 1018 steel cubes striking 2024-T3 aluminum plate, $t/d = 0.8$

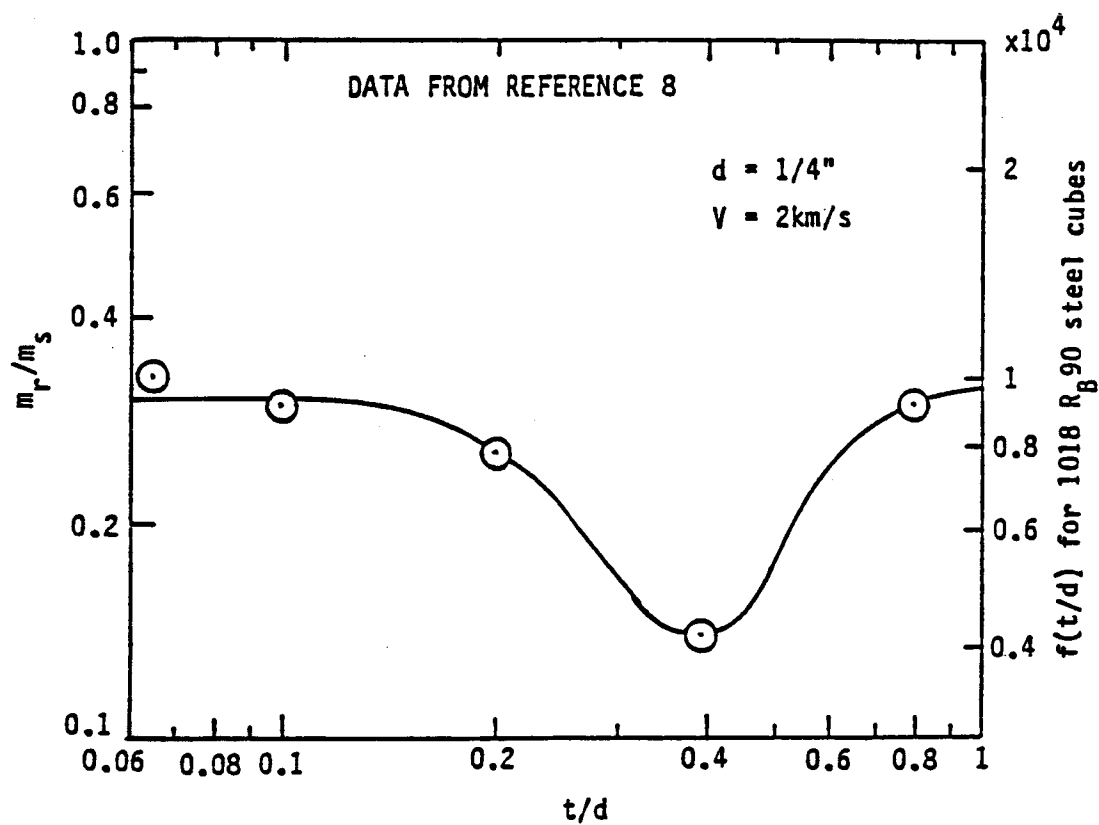


Figure C-6 Measured functional dependence of largest residual mass on t/d for Rb90 1018 steel cubes striking aluminum plate.

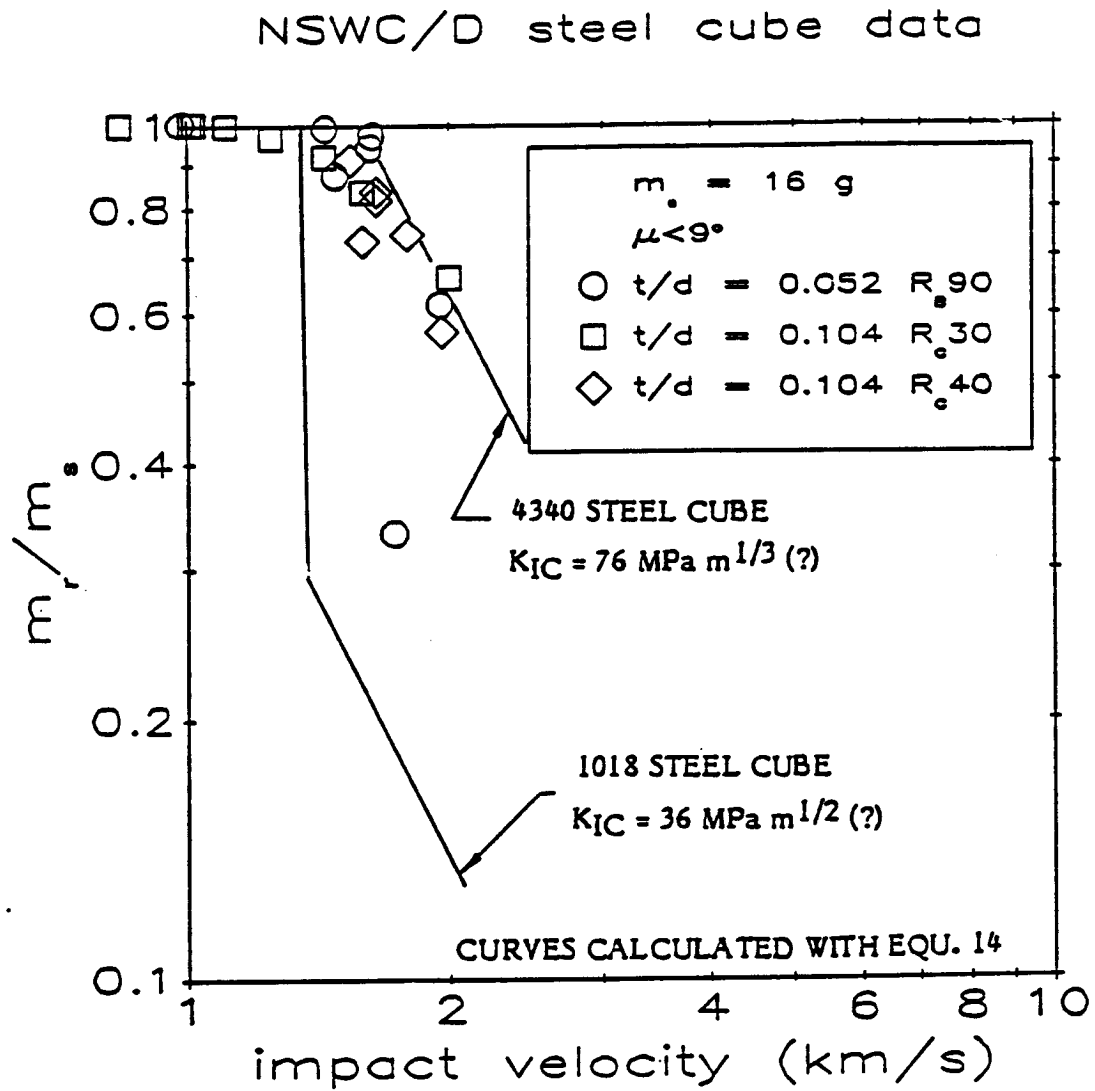


Figure C-7 Largest residual fragment mass as a function of impact velocity for steel cubes and aluminum cylinders striking aluminum.

Material	Rockwell Hardness	Fracture Toughness* (MPa-m ^{1/2})	Source (Reference)
<u>Steel</u>			
4340	R _C 60	55	24
4340	R _C 50	60	24
4340	R _C 45	76	24
4340	R _C 40	76	estimate
4340	R _C 30	76	estimate
1018	R _B 90	36	25
<u>Aluminum</u>			
2024-T351		39	24
7075-T6		28	24

*Toughness in the L-T direction.

Table C-1 Fracture toughness for 8 materials.

have the same K_{Ic} .

Assuming K_{Ic} is constant for hardnesses between R_c 30 to 45 (i.e., yield strengths from 1.1 GPa to 1.5 GPa) is not consistent with the trend of the data plotted in figure C-8. A plot of K_{Ic} as a function of hardness (i.e., yield strength) for 6 steels taken from Ref. C-4 is reproduced in figure C-8. Note that the trend is for K_{Ic} to decrease with increasing hardness in general agreement with Table C-1. However, the putative maximum value of $K_{Ic} = 76 \text{ MPa m}^{1/2}$ for 4340 steel listed in Table C-1 does not agree with all the points plotted in figure C-8. Furthermore, the values of hardness for which K_{Ic} is asserted to be constant range from 1.1 GPa to 1.47 GPa, the steepest portion of figure C-8.

It is thought that figure C-8 may be misleading, since the scatter in values is plus or minus $20 \text{ MPa m}^{1/2}$, which nearly encompasses all the data above the putative maximum. Furthermore, there are only 5 4340 steel points plotted in figure C-8 above the asserted maximum of $76 \text{ MPa m}^{1/2}$. More fracture toughness data are needed before an unqualified claim can be made that the data of figure C-7 refute the dependence on K_{Ic} claimed in Eq. C-10.

The value for fracture toughness of 1018 steel was taken from the value for low-carbon steel in Ref. C-3. This is the only value for fracture toughness of room temperature low carbon steel found in the literature search, and it was thought better to use it than to estimate from the values of other alloy steels. Not having reliable fracture toughness for 1018 steel is a major roadblock to verification of Eq. C-10.

Some degree of confidence in Eq. C-10 can be gained by comparing the predictions made with Eq. C-10's (which was developed from a fit to the NSWCD R_b90 1018 steel cube data) with the R_c40 4340 steel cube data from Ref. 26. This is tantamount to using the material properties of one steel to scale to the m_r/m results from another steel. All the 4340 R_c40 steel cubes had striking masses of 16g and impacted plates with thicknesses corresponding to a $t/d = 0.1$ ratio. No R_b90 1018 steel cubes with an initial mass of 16 g were launched at plates with t/d ratio of 0.1, so the smaller size 1018 steel cube data was size-scaled using Eq. C-10 to obtain the curve labeled "1018 steel cube" in figure C-7. The fracture toughness data from Table C-1 were then substituted into Eq. C-10 and the curve labeled "4340 steel cubes" resulted, which is in reasonable agreement with the data, lying no more than 5% above the R_c 30 and 40 4340 steel cube data.

A second check on the fracture toughness dependence of Eq. C-10 took advantage of the negligible dependence of m_r on t/d for t/d 's less than 0.1. Some test data with 1018 R_b90 steel cubes with an initial mass of 16g striking plates with a $t/d = 0.065$ are plotted as open circles in figure C-7. Only two tests produced significant fragmentation; one shows dependence on alloy and hardness and the other lies with the 4340 steel data showing no dependence on alloy and hardness. It is asserted here that the point

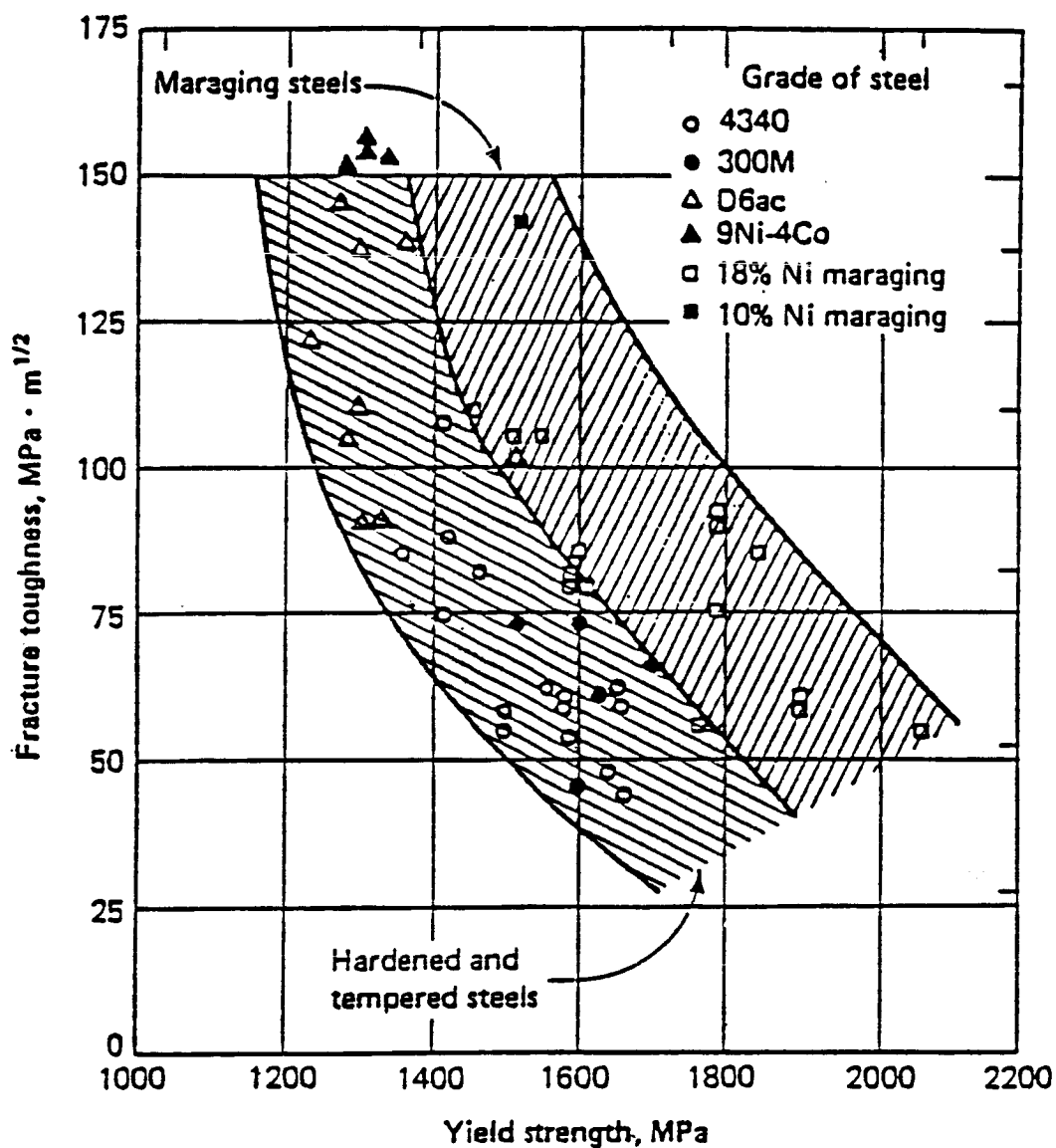


Figure C-8 Correlation between fracture toughness and yield strength for ultra high-strength steels.

lying with the R_p 90 1018 steel data points is fragmenting by spallation and hence is not expected to lie on the curve labeled "1018 steel cube" in figure C-7 and calculated with Eq. C-10. Furthermore, the point that lies between the two curves may also have fragmented by spallation and hence not have to lie on the 1018 steel curve, much like some 16 g data plotted in figure C-5. If such is not the case, then Eq. C-10 may need to be revised.

At best the above arguments on the correctness of the material properties dependencies in Eq. C-10 are suggestive and not compelling. More test data comparing the largest residual fragment masses from impacts with different hardnesses of 4340 steel projectiles are needed before Eq. C-10 can be unequivocally claimed right or wrong.

For the assumed values for fracture toughness it is possible to calculate $f(t/d)$ from figure C-6. The results of those calculations were used to label the vertical axis on the right hand side of figure C-6.

For simplicity the curve plotted in figure C-4 has been approximated by a piecewise continuous line connecting the data points. For R_p 90 1018 steel cubes striking 2024-T3 aluminum plate the following functions were obtained for $f(t/d)$,

$$\begin{array}{lll} f(t/d) & = & 9.17 \times 10^3 \quad t/d < 0.1 \\ & = & 5.42 \times 10^3 (t/d)^{-0.23} \quad 0.1 < t/d < 0.2 \\ & = & 1.90 \times 10^3 (t/d)^{-0.88} \quad 0.2 < t/d < 0.4 \\ & = & 1.17 \times 10^4 (t/d)^{1.1} \quad 0.4 < t/d < 0.8 \\ & = & 9.09 \times 10^3 \quad 0.8 < t/d. \end{array} \quad (C-11)$$

No attempt has been made to map out the functional dependence on the ratio of projectile and target shock impedance. The function of t/d shown in figure C-4 may change when the ratio of projectile and target shock impedance is changed, even when the fragmentation mechanism stays the same. Thus more test data are required to determine the function $f(t/d)$ for aluminum projectiles striking aluminum plate. Here, it will be assumed that the functional dependence is the same as shown in figure C-4.

An estimate was made of m_r as a function of V for 2024-T3 aluminum cylinders at $d = 1/4$ and $t/d = 0.1$ was based on recent Boeing IR&D tests, Ref. 25. These data are shown plotted in figure C-9. Some data for m_r show a larger mass than the original mass, m_s . This results from aluminum plate material adhering to the aluminum projectile. The curve is shown as a broken line in figure C-5. Using the constant offset shown in figure C-5, the offset for $f(t/d)$ for 2024-T3 aluminum cylinders was calculated and used to calculate the right-most y-axis for $f(t/d)$ in figure C-4 and the two curves for $t/d = 0.3$ and 0.8 shown in figure C-9.

To obtain $f(t/d)$ for 2024-T3 aluminum projectiles striking 2024-T3 aluminum plate divide Eqs. C-11 by 7.77.

1985 IR&D data

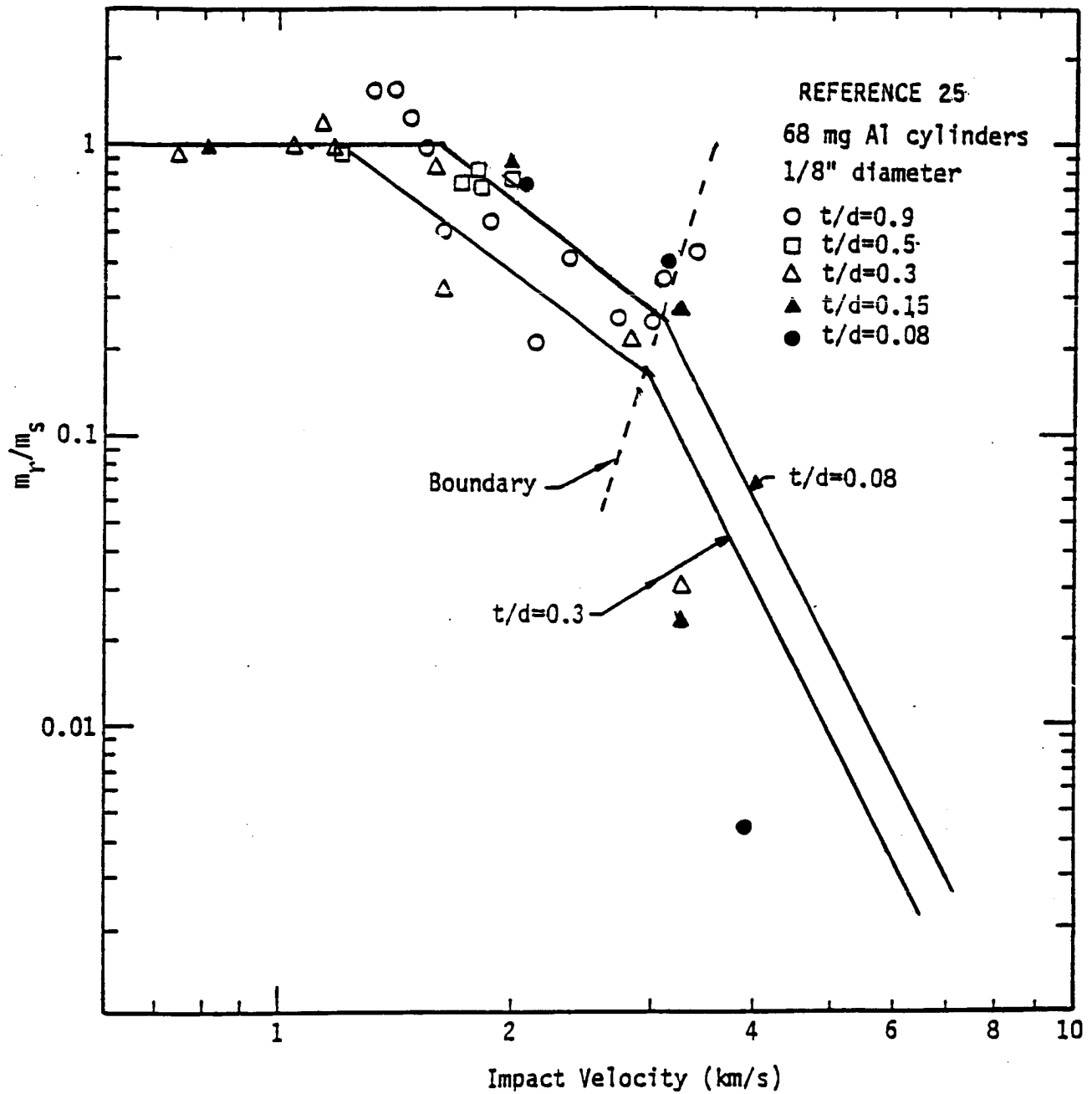


Figure C-9 Largest residual fragment mass as a function of impact velocity for aluminum cylinders striking aluminum plate in the fragmentation roll-off regime.

APPENDIX D

EFFECT OF PROJECTILE FRAGMENT
SPATIAL DISTRIBUTION

To explore the effect of the assumed distribution of fragment impacts on the second plate, the following parameter study of the effect of using the spatial distribution from the FATE penetration code documented in Ref. 34 was performed. In Ref. 34 the cumulative number of impacts on the second plate is proportional to the radius of the circle enclosing the impacts. This distribution (called here the FATE distribution) results in the number of impacts per unit area being larger for the center of spray area than for the edge of the spray area. This follows, since the cumulative number of impacts is proportional to the radius of the enclosing circle, while the area contained within the circle is proportional to the radius squared.

The effect of the FATE spatial distribution on PEN4 output was tested by calculating the minimum diameter projectile required to perforate a given two plate array as a function of impact velocity (called here a critical diameter plot). The output from a PEN4 version 10 run using the standard spatial distribution (which allocates an equal probability to the impact any spot within the spray area) are plotted in figure D-1 as a solid curve. The PEN4 version 10 curve compares favorably with the test data from Ref. 15 plotted as open circles in figure D-1.

Following the above calculation, PEN4 was modified to incorporate the FATE spatial distribution. The multiple impact algorithm was also modified so that all impacts were spread evenly at constant polar angle (i.e., there was no standard deviation to the number of multiple impacts. This is equivalent to the method FATE uses to spread impacts at a constant polar angle.). The results of this calculation are plotted as a dashed line in figure D-1. Note that the FATE distribution has led to a monotonically increasing ability of the projectile to perforate the two plate array with increasing impact velocity, contradicting the test data plotted in figure D-1.

As a point of reference, the program FATE was run to obtain the critical diameter curve plotted as a solid line in figure D-2. Note that the solid line curve in figure D-2 shows decreasing perforating ability with increasing impact velocity similar to the data plotted in figure D-1. Nevertheless, upon examination of the FATE penetration code it was found that FATE ceases to consider the possibility of perforation once all the projectile fragments are stopped. If FATE is allowed to consider perforation by plate fragments alone, as well as combinations of projectile and plate fragments, then the dashed curve plotted in figure D-2 results, in qualitative agreement with the modified PEN4 results.

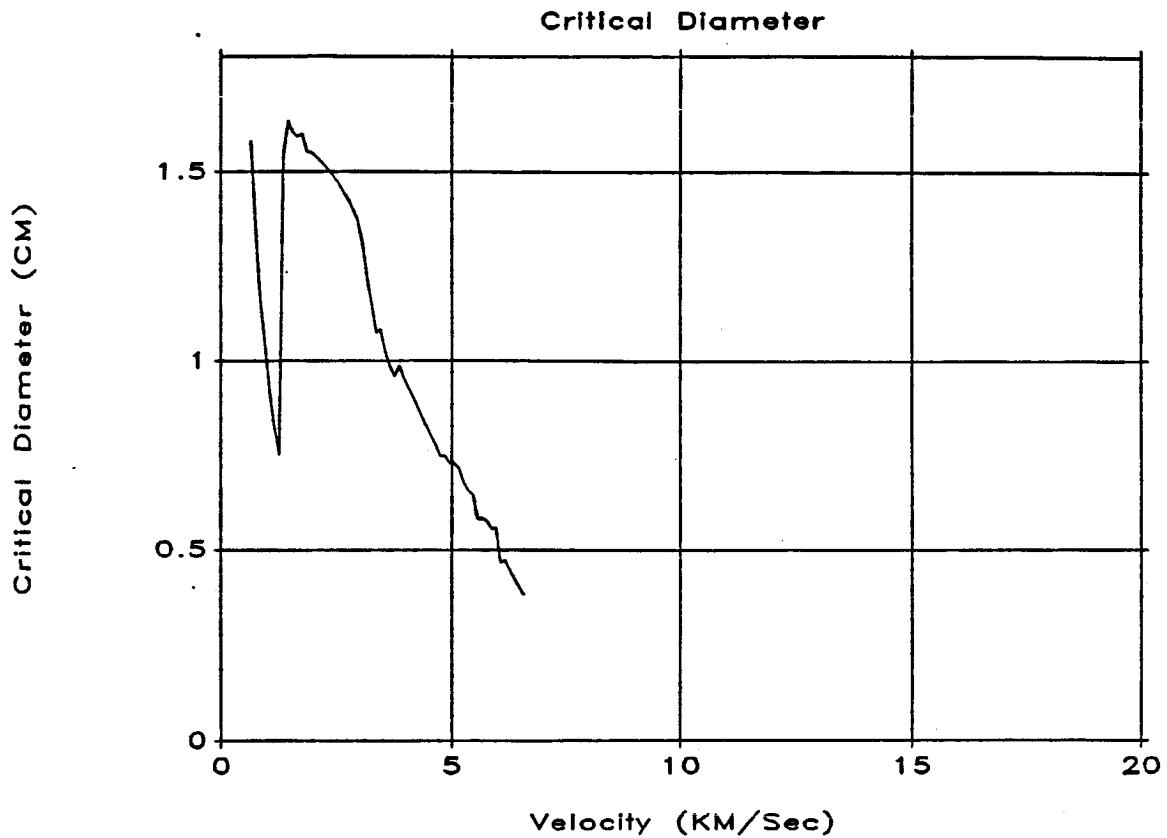


Figure D-1 Critical diameter curves calculated using FATE spatial distribution and an equal probability of impacting any spot in the spray area.

Critical Diameter

Critical Diameter (CM)

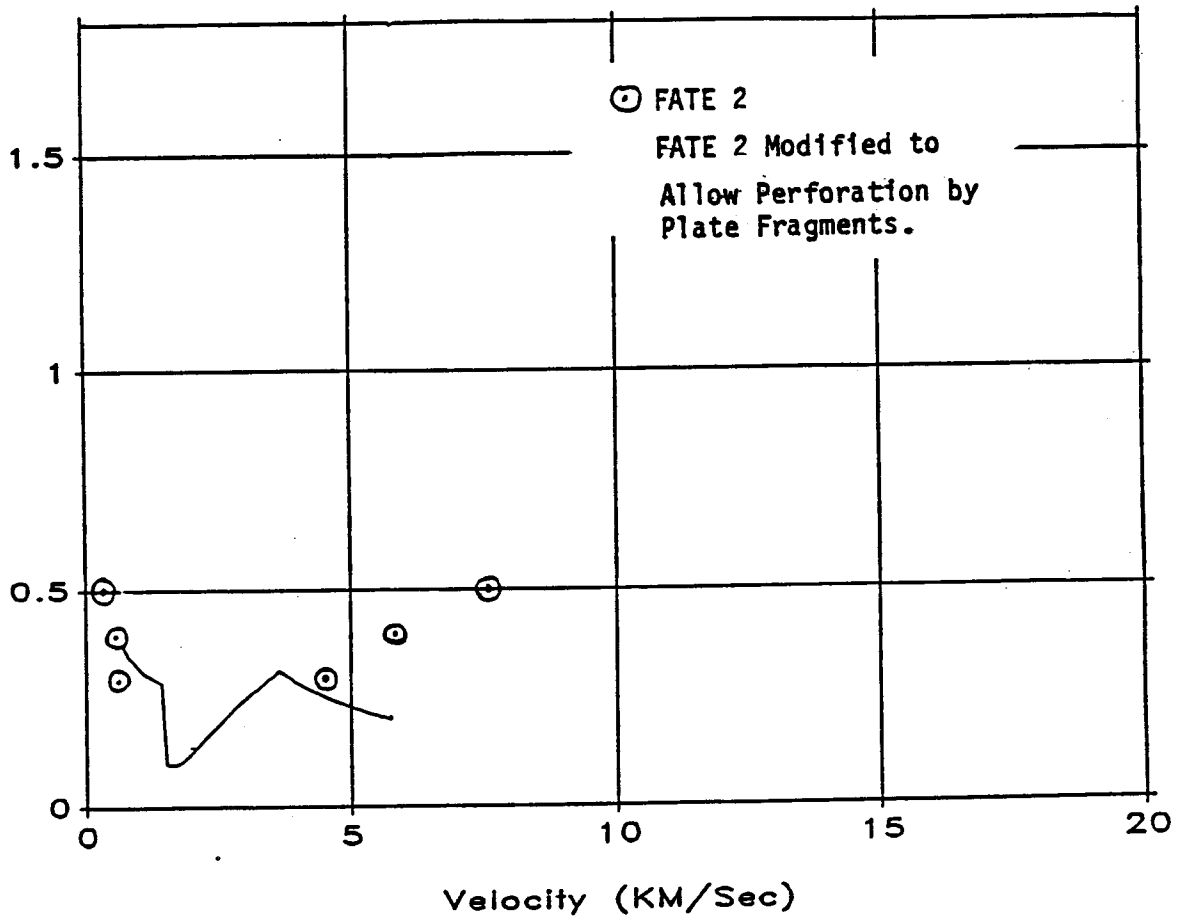


Figure D-2 Critical diameter curve calculated with FATE 2.

On the basis of the results plotted in figures D-1 and D-2 it is concluded that the original spatial distribution in PEN4 is adequate and that it is not necessary to incorporate the FATE spatial distribution into PEN4.

APPENDIX E

DEMONSTRATION OF CONVERGENCE

A important check on the self-consistency of the PEN4 algorithm is demonstrating that PEN4 converges on an answer as the number of fragment mass bins is increased. Far fewer bins are used in the calculation than occur in an actual impact, hence the PEN4 calculation is expected to converge on a single answer (i.e., the one that occurs in an actual impact) as the number of bins is increased. Convergence is demonstrated in figure E-1 for the series of calculations with 3, 5, and 10 bins. Note, however, that the way mass is allocated between the bins affects the final answer. Allocating the mass equally between the bins resulted in convergence on an approximately 10% larger critical diameter at 10 to 15 km/s impact velocity than using the procedure described in section 2.3.6.5.

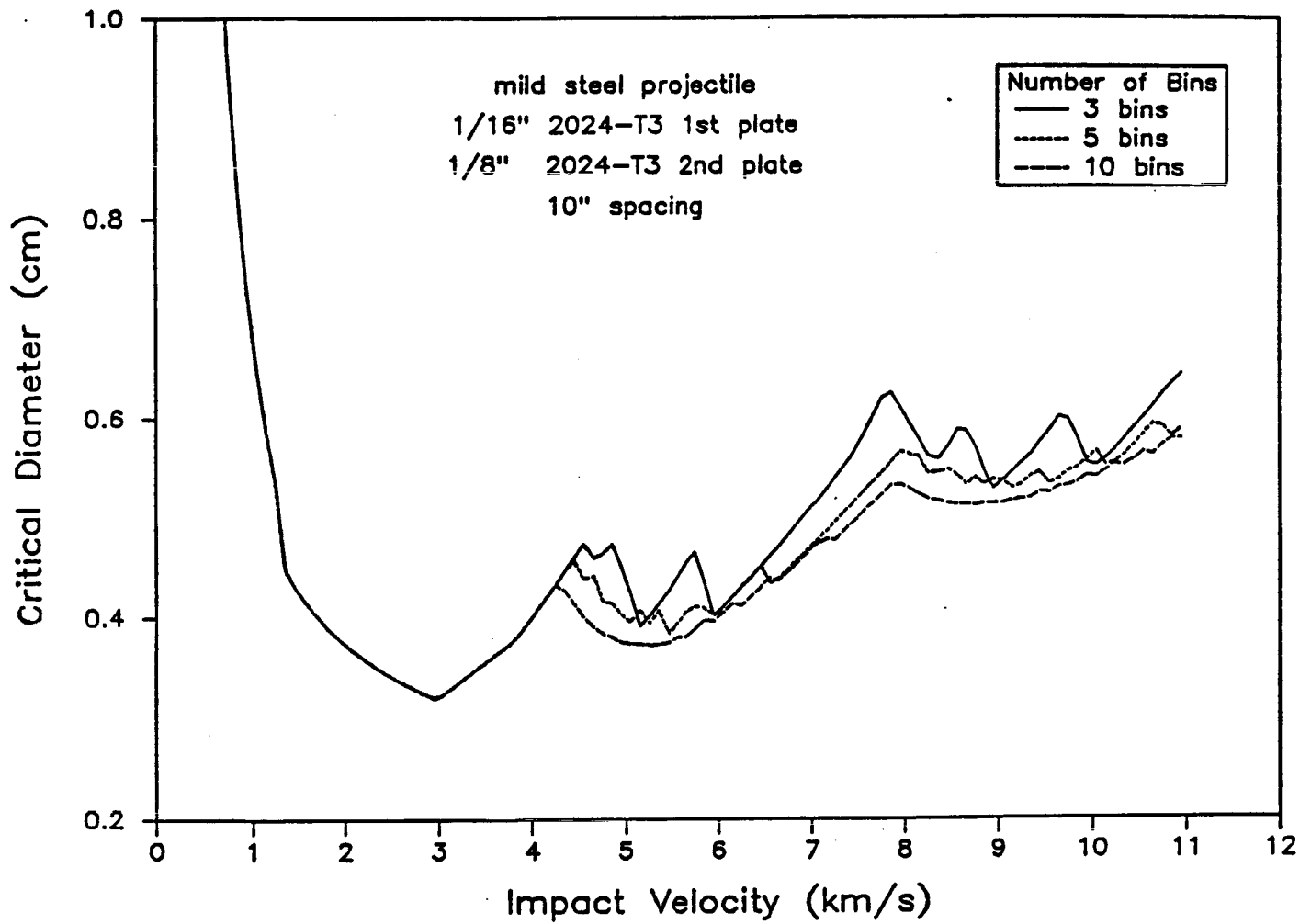


Figure E-1 Test for Convergence.

APPENDIX F

CRITICAL DIAMETER CURVE BEHAVIOR
AT IMPACT VELOCITIES LARGER THAN 13 km/s

Originally, the PEN4 method for calculating the critical diameter curve was expected to result in a curve similar to that shown as the solid line in figure F-1. The minimum diameter projectile required for perforating a two plate array was expected to decrease as a function of increasing impact velocity from 0 km/s to approximately 4 km/s impact velocity. Impact velocities larger than approximately 4 km/s were expected to result in minimum projectile diameters increasing as a function of increasing impact velocity. It was reasoned that, since at approximately 4 km/s impact velocity steel projectiles enter the roll-off fragmentation mechanism, the size of the projectile fragments would start to decrease much more rapidly with increasing impact velocity than the crater depth would increase.

What was actually calculated with PEN4 is more closely represented by the dashed line in figure F-1. At impact velocities larger than approximately 13 km/s the calculated minimum diameter for perforation of a two plate array starts to decrease as a function of increasing impact velocity.

It was discovered that the calculation of probability of multiple impacts was responsible for the decrease in the critical diameter curve that begins at about 13 km/s. Most factors involved such as the fragment size and the individual crater depths of the fragment are described as power law functions of impact velocity. The largest residual fragment mass in the roll-off fragmentation region is proportional to $V^{6.2}$, while the crater depth is proportional to the cube root of the impacting fragment mass. Hence the crater depth from the largest residual fragment mass is proportional to $V^{2.38}$. The binomial distribution given in Eq. 83 on the other hand has several factorial terms in it. When Eq. 83 is rewritten with the large factorials replaced by Stirling's approximation Eq. F-1 results,

$$P(k) = e^{-k} N_r^k (N_r / (N_r - k))^{N_r - k + 1/2} / k! P_c^k (1 - P_c)^{N_r - k}. \quad (F-1)$$

At large impact velocities N_r is many orders of magnitude larger than k and increases as $V^{6.2}$.

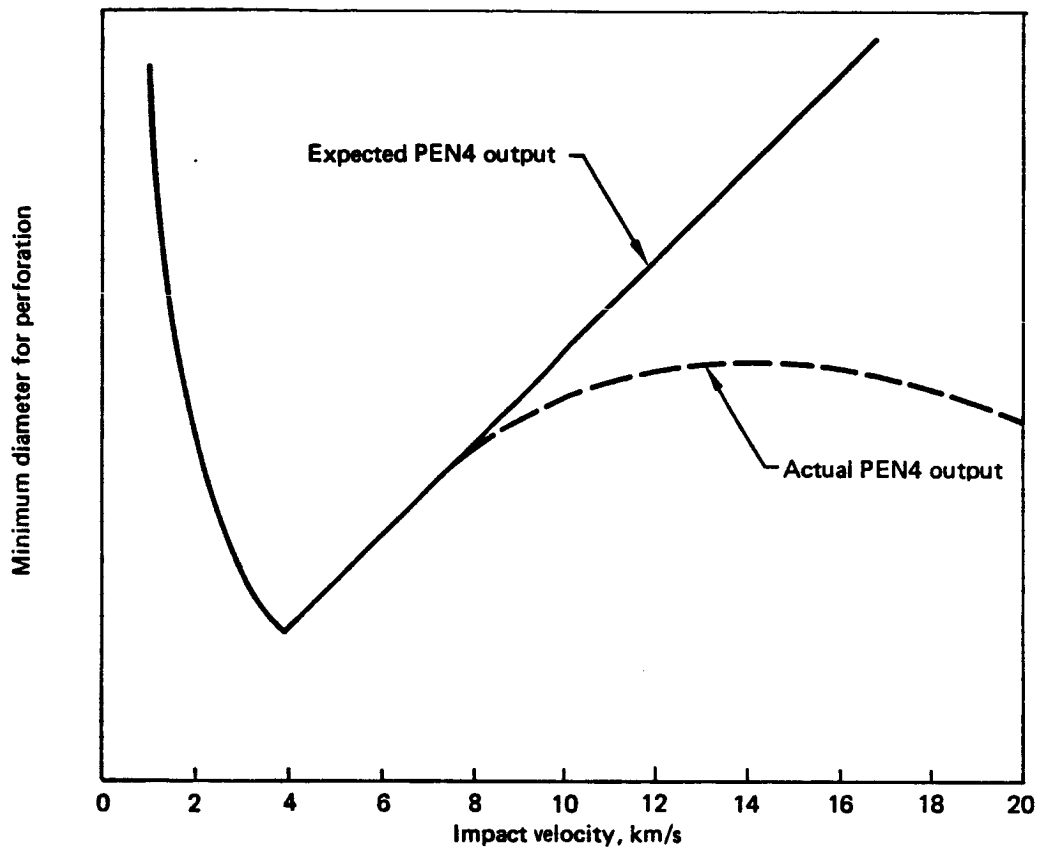


Figure F-1 Critical Diameter Curve Behavior above 13 km/s Impact Velocity